Title	Cold stream properties in the circumgalactic medium: the role of magnetic field and thermal conduction
Author(s)	Ledos, Nicolas
Citation	大阪大学, 2023, 博士論文
Version Type	VoR
URL	https://doi.org/10.18910/95938
rights	
Note	

Cold stream properties in the circumgalactic medium: the role of magnetic field and thermal conduction

by

Nicolas Ledos

A thesis submitted in partial fulfillment for the

degree of Doctor of Philosophy

in the

Department of Earth and Space Science

Graduate School of Science

Osaka University

November 2023

Abstract

Background: Galaxy formation and evolution is a challenging field linking the early state of our Universe that is imprinted in the cosmic microwave background to the Milky Way and the numerous observed nearby galaxies. Current state-of-the-art cosmological simulations reproduce relatively well important galaxies' properties such as the two distinct populations in the nearby galaxies or the cosmic star formation history. Moreover, cosmological simulations unveil a physical key mechanism behind the galaxies' properties: the cold stream scenario. In the early Universe ($z \gtrsim 2$) galaxies are predicted to acquire most of the fuel of their star formation via cold streams of gas with temperature $\sim 10^4\,\mathrm{K}$ flowing along the potential of the cosmic web. Despite the ubiquitous nature of this scenario from cosmological simulations, the current simulations' accuracy is insufficient to fully capture the stability and Lyα emission properties of these cold streams. Deciphering the characteristic emission of the cold streams is essential to fully understand the numerous observed Lyα emitters.

Method: To answer this challenge, recent efforts focused on idealized high-resolution hydrodynamics (HD) simulations. Our research follows this current trend by performing a large suite of 2D magneto-HD (MHD) simulations assessing for the first time how magnetic fields at various angles and anisotropic thermal conduction (TC) influence the dynamics of radiatively cooling cold streams. Those simulations are performed using the astrophysical code Athena++ on which we implemented the anisotropic thermal conduction module.

Results: We find that an initially small magnetic field strength of approximately $10^{-3}\,\mu\mathrm{G}$, with a field oriented non-parallel to the stream, undergoes significant growth. The amplification of the field increases the stability of the stream against Kelvin-Helmholtz instabilities and reduces Lyα emissions by a factor of less than 20 compared to the hydrodynamics scenario. The inclusion of anisotropic thermal conduction (TC) categorizes the stream evolution into three distinct regimes: (1) the *diffusing stream* regime, where the stream diffuses into the surrounding hot circumgalactic medium; (2) the *intermediate* regime, characterized the mixing layer diffusion, leading to increased stability and reduced Lyα emissions; (3) the *condensing stream* regime, where the influence of magnetic fields and TC on the stream's emission and evolution is negligible. Extrapolating these findings to a cosmological context suggests that cold streams with a radius of $\lesssim 1\,\mathrm{kpc}$ may serve as a prolonged source of cold, metal-enriched, magnetized gas (with magnetic field strengths in the range of 0.1 to $1\,\mu\mathrm{G}$) for massive galaxies in the early Universe. This, in turn, results

in a broad spectrum of Lyα luminosity signatures ranging from approximately 10^{37} up to 10^{41} $\mathrm{erg\,s^{-1}}$.

"Faithless is he that says farewell when the road darkens."

J.R.R. Tolkien, *The Lord of the Rings*

Acknowledgements

This thesis was a long and unforgettable journey in the field of Astrophysics. Besides the scientific adventure, working at the OUTAP was a real pleasure. Many actors helped and guided me throughout this journey and I would like to immensely THANKS them.

Kentaro Nagamine, my PhD supervisor, for allowing me to enter in the field of Astrophysics, for his support throughout the long path of the PhD, and for his friendliness in his supervision.

Shinsuke Takasao, whose help and guidance in the treacherous path of magnetohydrodynamics and numerical methods was crucial in the achievement of this work. I deeply appreciate our discussions.

The jury committee, Hironori Matsumoto, Hirokazu Odaka, and Takayoshi Sano, for their questions which helped in improving this work.

All the current and past professors of the group: Yoshiyuki Inoue, Daisuke Toyouchi, Luca Baiotti, Hiroyuki Hirashita, Kengo Tomida and more, for their support and our discussions.

Current and past students and Postdocs, Yuri for his help in navigating the Japanese system, Keita because *this is the way*, Abednego for all our discussions, Zhao for the introduction to the best and spiciest Chinese food, Dylan for having brought back french language in the group, Kei for his promotion of nomikai, Ellis, who loves sandwiches, for our discussions, Samuel for his helpful proof-reading, Sudipta for our appointed salada-time discussions, Enrico for the introduction to role-play game, Kengo for our discussions, and his interest in Paris, Pierre for his help upon my arrival in Japan and all other members and students for the great time spent with them.

I would like to give special thanks to Mariko Tokiwa and Hiroko Joh for their immense support and help in smoothly handling my path through the Japanese administration.

Last but not least, I want to express my sincere gratitude toward my family and my partner Yasuko, for their support in daily life.

Contents

List of Figures

List of Tables

Abbreviations

AGN	**A**ctive **G**alactic **N**uclei
BC	**B**oundary **C**onditions
CDM	**C**old **D**ark **M**atter
CGM	**C**ircum**g**alactic **M**edium
CMB	**C**osmic **M**icrowave **B**ackground
COBE	**CO**smic **B**ackground **E**xplorer
EoR	**E**poch **o**f **R**eionization
ESA	**E**uropean **S**pace **A**gency
FLRW	**F**riedmann **L**emaître **R**obertson **W**alker
FRB	**F**ast **R**adio **B**urst
FRB	**F**araday **R**otation **M**ap
HD	**H**ydro**d**ynamics
IC	**I**nitial **C**onditions
IGM	**I**nter**g**alactic **M**edium
KHI	**K**elvin-**H**elmholtz **I**nstabilities
MHD	**M**agneto-**H**ydro**d**ynamics
ML	**M**ixing **L**ayer
PDE	**P**artial **D**ifferential **E**quation
SFR	**S**tar **F**ormation **R**ate
TC	**T**hermal **C**onduction
WMAP	**W**ilkinson **M**icrowave **A**nisotropy **P**robe

Chapter 1

Introduction

1.1 Universe and the large-scale structure

1.1.1 Cosmological background

One of the current main challenges of astrophysics is to reveal the history of the Universe and its underlying physics. Since the birth of general relativity theory (Einstein, 1916), the Universe itself has become a physical object that can be studied, leading to the creation of modern cosmology. The Universe is described as expanding both theoretically and from observations by Lemaître (1927)[1], and by Hubble (1929). To describe the Universe itself using general relativity, one must start by assuming its metric. Assuming the Universe is spatially homogeneous and isotropic on large scales, it can be described by the Friedmann–Lemaître-Robertson-Walker metric (FLRW),

$$\mathrm{d}s^2 = -c^2\mathrm{d}t^2 + a(t)^2\mathrm{d}l^2 = -c^2\mathrm{d}t^2 + a(t)^2\left[\frac{(\mathrm{d}r)^2}{1-kr^2} + r^2\left((\mathrm{d}\theta)^2 + \sin(\theta)^2(\mathrm{d}\psi)^2\right)\right], \tag{1.1}$$

with $\mathrm{d}t$ and $\mathrm{d}l$ the time and space interval, $\mathrm{d}s$ the invariant space-time interval, and $a(t)$ the scale factor accounting for the expansion of space in the function of time. Physically, $\mathrm{d}l$ represents the co-moving space interval. Under the spatially homogeneous and isotropic assumptions, the Universe can have three trivial geometries: a 3-sphere with positive curvature, a 3-dimensional flat space with no curvature, or a hyperbolic 3-space with negative curvature. The term r, θ, and ψ are the coordinates of the 3-dimensional space, which are equivalent to spherical coordinates in

[1]see Lemaître (1931) for the English translation.

the case of a flat Universe[2]. In order to retrieve a common equation for all cases, the factor k is introduced and is defined by 1 for a positive curvature, also called close space, by 0 for a flat space (no curvature), and -1 for a negative curvature, also referred as an open space.

Considering the Einstein field equations and the stress-energy tensor of a perfect fluid leads to the Friedmann-Lemaître equations,

$$\begin{cases} H^2 = \left(\frac{\dot{a}}{a}\right)^2 = \frac{8\pi G}{3}\rho - \frac{kc^2}{a^2} + \frac{\Lambda c^2}{3}\,, \\ \left(\frac{\ddot{a}}{a}\right) = -\frac{4\pi G}{3}\left(\rho + \frac{3p}{c^2}\right) + \frac{\Lambda c^2}{3}\,. \end{cases} \tag{1.2}$$

The Hubble parameter describing the expansion rate of the Universe is defined by $H = \dot{a}/a$; ρ is the matter density, p is the pressure; while G, k and Λ are the gravitational constants, the curvature term and the cosmological constant, respectively. These equations are the foundation of the current standard model of cosmology as they allow us to describe the global evolution of the Universe properties and its expansion rate assuming the equation of state between p and ρ and a Universe curvature. For example, under the simple assumption of Einstein de-Sitter Universe ($k = 0$, $\Lambda = 0$) being dominated by dust ($p = 0$), one can find that $a(t) = a_0\,(t/t_{\mathrm{present}})^{2/3}$ and $H(t) = 2/(3t)$, with t_{present} our current time.

From a dimensional analysis of the first equation in the system 1.2, we can deduce a critical density,

$$\rho_{\mathrm{c}} = \frac{3H^2}{8\pi G}, \tag{1.3}$$

which defines the density limit between a Universe dominated by its expansion and a Universe dominated by gravity. In other words, the critical density defines if the structures in the Universe can still be bound by gravity or if these structures will increasingly distance themselves. Normalizing this same equation by H^2 yields to,

$$1 = \frac{\rho}{\rho_{\mathrm{c}}} + \frac{\rho_{\mathrm{k}}}{\rho_{\mathrm{c}}} + \frac{\rho_\Lambda}{\rho_{\mathrm{c}}} = \Omega_{\mathrm{m,tot}} + \Omega_{\mathrm{k}} + \Omega_\Lambda, \tag{1.4}$$

which describes the relative proportion of each component with $\Omega_{\mathrm{m,tot}} = \rho/\rho_{\mathrm{c}}$, $\Omega_{\mathrm{k}} = -kc^2/\dot{a}^2$, and $\Omega_\Lambda = \Lambda c^2/(3H^2)$, the cosmological parameter for the total matter, curvature and dark energy, respectively. From the second equation of the system 1.2, inserting the time derivative of the first one in it, with the assumption

[2] In the case of a 3-sphere or a hyperbolic 3-space, r is a conventional notation for $R\sin\phi$ and $R\sinh\phi$, respectively. The angle ϕ is another angle coordinate.

that $\dot{k} = 0$, i.e. the Universe's shape does not vary with time, we obtain,

$$\frac{\dot{\rho}}{\rho} = 3\,(1+w)\,\frac{\dot{a}}{a}, \tag{1.5}$$

where the fluid is assumed to be perfect with an equation of state defining the pressure as $p = w\rho c^2$. Integrating both part of equation 1.5 yields to,

$$\rho = \rho_0\,(1+z)^{3(1+w)}\,, \tag{1.6}$$

where $z = a_0/a\,(t)$ is the redshift. The coefficient of the above equation of state w have different values, and hence $\Omega_{\mathrm{m,tot}}$ can be decomposed into matter ($w = 0$) and radiation ($w = 1/3$). In practice, the cosmological constant term can also be expressed as a fluid with $w = w_{\mathrm{d}} = -1$. Using equation 1.6, we can then rewrite the first Friedmann-Lemaître equation as,

$$H(z) = H_0\sqrt{\Omega_{\mathrm{m},0}\,(1+z)^3 + \Omega_{\mathrm{r},0}\,(1+z)^4 + \Omega_{\mathrm{k},0}\,(1+z)^2 + \Omega_{\Lambda,0}}, \tag{1.7}$$

with $\Omega_{\mathrm{m},0}$, $\Omega_{\mathrm{r},0}$, $\Omega_{\mathrm{k},0}$, and $\Omega_{\Lambda,0}$ the cosmological parameters at present time ($z = 0$).

The current fiducial model to describe the Universe is the Λ Cold Dark Matter model (ΛCDM), the so-called standard cosmological model. Taking its origin to explain the "apparent" missing mass in nearby galaxies or the Milky Way (e.g., Zwicky, 1937, Babcock, 1939, Rubin & Ford, 1970), the introduction of an unknown, and yet undetected, dark matter is the current most successful model in cosmology. The first radiation of the Universe, the Cosmic Microwave Background (CMB), has been now thoroughly observed by the Cosmic Background Explorer (COBE, (Wright et al., 1990, Smoot et al., 1992, Bennett et al., 1996)), the Wilkinson Microwave Anisotropic Probe (WMAP, (Spergel et al., 2003, Komatsu et al., 2009, Larson et al., 2011, Bennett et al., 2013, Hinshaw et al., 2013)), and the ESA Planck Satellite (Planck Collaboration et al., 2014, 2016, 2020, 2021). From the CMB temperature and polarization, and as shown in Fig. 1.1, the cosmological parameters are constrained such that $H_0 = 67.4 \pm 0.5\,\mathrm{km\,s^{-1}\,Mpc^{-1}}$, $\Omega_{\mathrm{m},0} = 0.315 \pm 0.007$, and $\Omega_{\mathrm{k}} = 0.001 \pm 0.002 \sim 0$, with $\Omega_{\mathrm{r},0} = 0$, which gives $\Omega_{\Lambda,0} = 0.685$. The ΛCDM model hence assumes a flat-Universe ($k = 0$). The proportion of baryonic and dark matter are also defined as $\Omega_{\mathrm{b},0} = 0.0494 \pm 0.0003$ and $\Omega_{\mathrm{c},0} = 0.265 \pm 0.0026$ (Planck Collaboration et al., 2020), meaning that the matter in the Universe is composed currently of $\sim 17\%$ of baryons and $\sim 83\%$ of dark matter. To note, those proportions change with time, as, at the time of the CMB ($z \sim 1100$), the matter was also composed of a large amount of relativistic matter such as photons, and neutrinos. Considering such parameters, the resulting age of the Universe is $t_{\mathrm{present}} \sim 13.8 \pm 0.002$ Gyr with

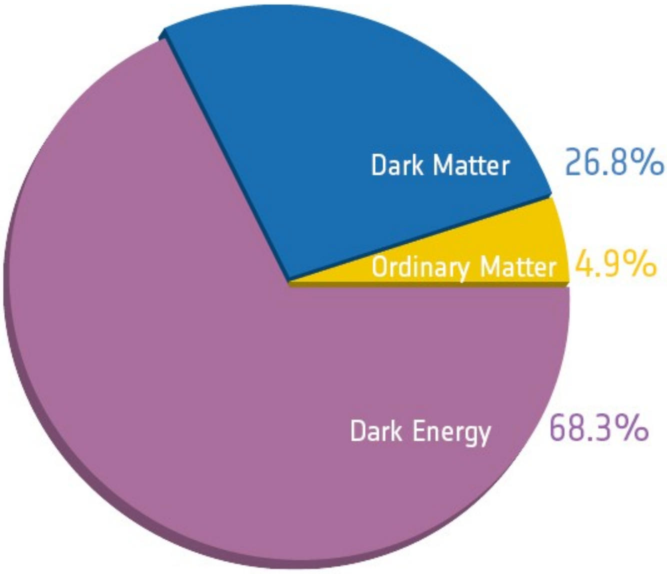

FIGURE 1.1: The composition of the Universe. Source: ESA, PlanckESA, Planck.

the Big Bang being chosen as a reference origin $t = 0$. On top of the measurements from the CMB, observations from the nearby Universe by supernova type-Ia using distant ladders (Riess et al., 1998, 2004, 2007, Perlmutter et al., 1999, Kowalski et al., 2008), and from the baryon acoustic oscillation (Seo & Eisenstein, 2003, Eisenstein et al., 2005, Percival et al., 2007, 2010, Anderson et al., 2014, Delubac et al., 2015) also confirm the cosmological parameters of the ΛCDM model ($w_{\rm d} = -1$) in a flat ($k \sim 0$) Universe.

1.1.2 Structure formation

We now describe the Universe's history from observations and from the framework of the ΛCDM model. This history is illustrated by the timeline in Fig. 1.2. Immediately

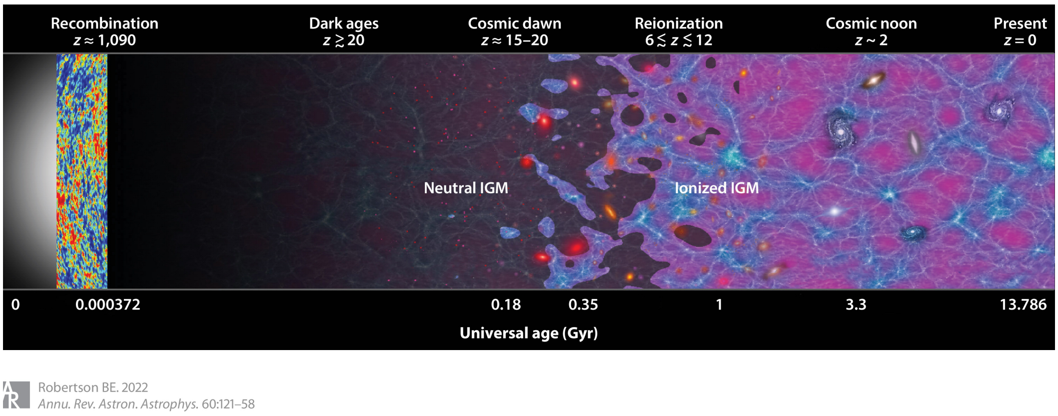

FIGURE 1.2: Timeline of the Universe history. Source: Robertson (2022, Fig. 1).

following the inflation, the period in which the Universe was subject to a rapid expansion, the matter becomes highly dense and fully ionized, rendering it optically thick to Thomson scattering. With the expansion of the cosmos, the gas temperature dropped due to adiabatic cooling, while the fraction of neutral hydrogen gradually increased. Approximately $380,000$ years after the Big Bang (at a redshift $z \sim 1100$), the electrons and protons of the gas can recombine, hence releasing the so far trapped photons in the fluid, leading to the CMB radiation. The Universe is then composed of mainly hydrogen ($\sim 76\%$ in mass) and helium ($\sim 24\%$ in mass) with traces of heavier elements (lithium and berylium).

Following the recombination (at $z \sim 1100$), the Universe continued to expand, causing the gas temperature to decrease progressively. At this epoch, the gas is neutral, meaning a complete absence of emission and leading to the so-called "dark age" (see Figure 1.2). Despite the absence of emission from this epoch, this period is quite important as it marks the basis of structure formation in the Universe. From the primordial fluctuation of the CMB and by the action of gravity, the dark matter perturbations grow, forming first walls, filaments, and then, at the intersection of those threads, high-density knots. Local dark matter (DM) higher-density regions in threads and knots grow and merge into massive haloes. This hierarchical structure formation, also called the "bottom-up" scenario, is a signature of the ΛCDM model (e.g. Press & Schechter, 1974, White & Rees, 1978, Lacey & Cole, 1993, Navarro et al., 1996, 1997, Sheth & Tormen, 1999, Somerville & Kolatt, 1999, Sheth & Tormen, 2002, Reed et al., 2003, Springel et al., 2005, De Lucia & Blaizot, 2007, Boylan-Kolchin et al., 2009, Guo et al., 2011, Vogelsberger et al., 2014). Such DM evolution leads to the formation of a cosmic web in which gravitational potential attracts the baryonic matter. Subsequently, the baryonic matter also forms walls, thread and knots in which, at the overdense regions, the first stars form, enlightening once again the Universe. The fact that the baryonic matter is bound to flow in the dark matter components shows the crucial link between cold dark matter haloes and baryons (e.g. Rees & Ostriker, 1977, Blumenthal et al., 1984, Davis et al., 1985, Couchman & Rees, 1986, White & Frenk, 1991, Efstathiou, 1992, Kauffmann et al., 1993, 1999, Haardt & Madau, 1996, Tegmark et al., 1997, Barkana & Loeb, 2001, Abel et al., 2002, Yoshida et al., 2006, 2008, Greif et al., 2008, 2010, Wise et al., 2012a,b).

These first galaxies produce ionizing photons, giving rise to H II bubbles within the intergalactic medium (IGM). The further galaxies grow and stars form, the further these ionized regions expand and overlap, ultimately leading to the almost complete reionization of hydrogen. This significant transition in the Universe's evolution is known as the "epoch of reionization" (EoR), which ended approximately one billion years after the Big Bang (at $z \sim 6$) (e.g. Gnedin, 2000b,a, Furlanetto et al., 2004, Shapiro et al., 2004, Gnedin, 2014, Iliev et al., 2014, Ocvirk et al., 2016, Xu et al., 2016, Pawlik et al., 2017, Rosdahl et al., 2018, Finlator et al., 2018, Lewis et al., 2022, Smith et al., 2022, Kannan et al., 2022, Robertson, 2022, Endsley et al., 2023, Treu et al., 2023, Shen et al., 2023).

Once all the hydrogen in the Universe is ionized, the structures continue their growth, with baryons falling further into dark matter potential leading to the growth of galaxies via gas accretion and merger. Fig. 1.3 shows the resulting large-scale structure around the Milky Way (Geller & Huchra, 1989, Gott III et al., 2005) and mock comparisons from cosmological simulations (Springel et al., 2005). The web is characterized by voids, walls, filaments, and knots, whose structures reflect the dark matter distribution and as a consequence, the galaxy distribution.

1.2 Galaxy formation and gas accretion

1.2.1 Galaxy formation and population

The increasing samples of observed galaxies are also followed by the increasing variety in galaxies' luminosity, shapes, mass, and environments. The golden aim of galaxy formation and evolution theory is to explain all galaxies' properties and varieties. The current first step in this approach is to understand the global properties of galaxies before zooming in on specific cases. Those main properties are showcased in Fig. 1.4.

Galaxies are gigantic factories of stars and their star-formation rate (SFR) is a valuable tracer to understand their evolutions. Madau & Dickinson (2014) compiled the SFR of wide samples of UV and IR observations galaxies (Sanders et al., 2003, Takeuchi et al., 2003, Wyder et al., 2005, Schiminovich et al., 2005, Robotham & Driver, 2011, Dahlen et al., 2007, Reddy & Steidel, 2009, Magnelli et al., 2011, 2013, Bouwens et al., 2012a,b, Cucciati et al., 2012, Schenker et al., 2013, Gruppioni et al., 2013). Figure 1.4 shows the resulting cosmic SFR density in function of redshift and lookback time. In the Universe's history, galaxies formed the highest number of stars very early at $z \sim 2$, i.e., ~ 2.5 Gyr after the Big Bang. The SFR density then declines gradually down to the value it had after the EoR ($z \sim 6$).

At our current time, the large amount of observed nearby galaxies showcases two evident populations in the colour–stellar mass space. The colour bimodality is characterized by a population of red and massive galaxies, while the second population

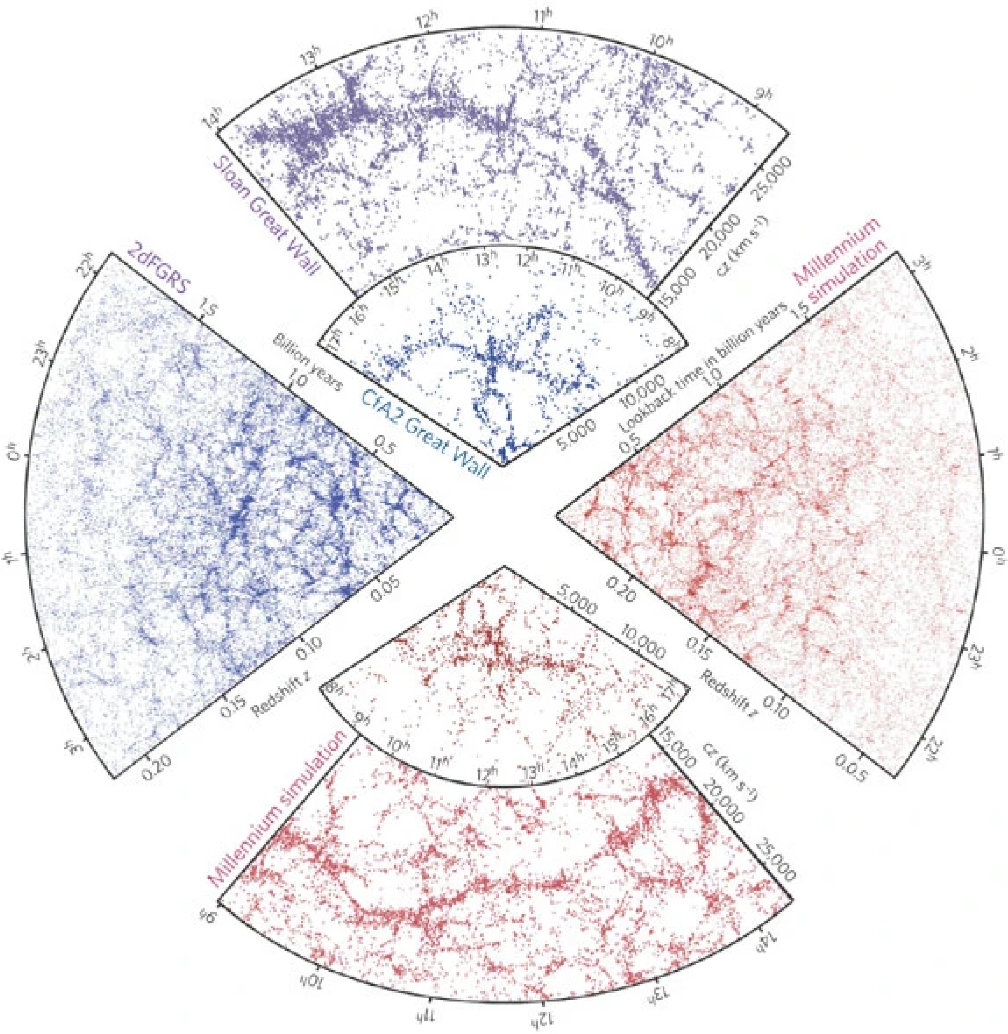

FIGURE 1.3: The cosmic web around us. The blue data are observed galaxies obtained by spectroscopic redshift surveys from Geller & Huchra (1989) and Gott III et al. (2005) for the left and top panels respectively. Red points show galaxies in similar environments from cosmological simulation (Springel et al., 2005). Source: Springel et al. (2006, Fig. 1).

is defined by blue and smaller galaxies (Strateva et al., 2001, Blanton et al., 2003, Yang et al., 2003, Kauffmann et al., 2003, Baldry et al., 2004, Bell et al., 2004). Red galaxies are mainly elliptical shapes populated by old stars, they exhibit low SFR. They are also referred to as early-type galaxies as they are expected to form most of their stars in the early age of the Universe, growing in mass with time while depleting their gas reservoir which fueled their SFR. In opposite, the blue galaxies represent relatively young spiral star-forming galaxies, with relatively low mass but with enough gas to fuel their SFR. They are referred to as late-type galaxies.

The bottom panel of Fig. 1.4 shows the mass function of galaxies for the blue and red sequence. The mass function first highlights the results from the colour bimodality, showing that most young blue galaxies are distributed towards lower mass, while the

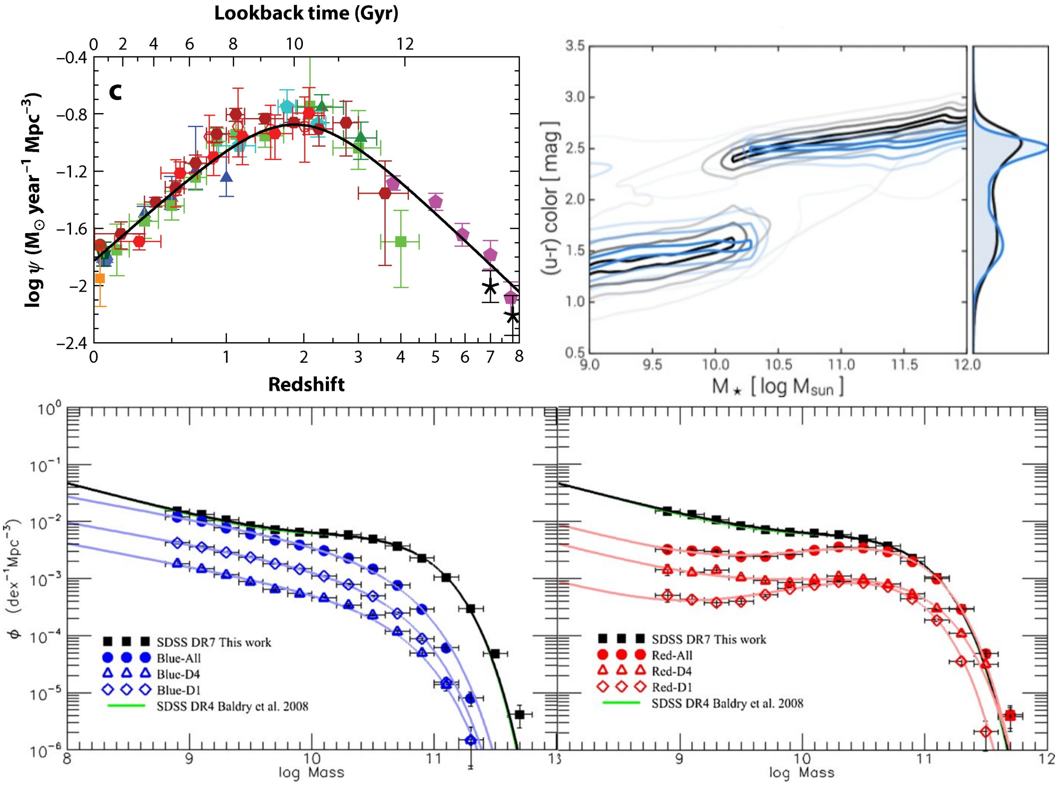

FIGURE 1.4: *Top left panel:* The star-formation density in the function of redshift from FUV and IR observations (see review, Madau & Dickinson, 2014). Source: Madau & Dickinson (2014, Fig. 9). *Top right panel:* The galaxy colour bimodality from SDSS catalog Strateva et al. (2001) and the IllustrisTNG cosmological simulation Nelson et al. (2018). Source: Nelson et al. (2018, Fig. 3, bottom-left panel). *Bottom panel:* Galaxy mass function for blue galaxies (left) and red galaxies (right). Source: (Peng et al., 2010, Fig. 12).

red galaxies are mostly situated at higher mass with a bulk around $M_* \sim 10^{10.5}\,\mathrm{M}_\odot$. The galaxy mass function is crucial in the understanding of galaxy evolution because analytical structure formation models Press & Schechter (1974), Sheth et al. (2001) and early cosmological simulations (Springel et al., 2005, Baldry et al., 2008, Genel et al., 2014) fail to reproduce either one or both the low and high-mass galaxy populations, overestimating them. The higher predicted number of low and high-mass galaxies comes from the fact that if only considering dark matter or hydrodynamics without sub-grid physics, the baryons continuously accumulate inside galaxies without being ever removed from it. In a realistic case, feedback mechanisms can expulse a large amount of gas outside the galaxy, and even push the gas around the galaxy, cutting off its fuel supply to create stars. The dominant feedback mechanism for low-mass galaxies is stellar feedback, either by stellar wind or supernovae. For the higher mass galaxies, stellar feedback is not strong enough to expulse the gas outside for a long period, leading to efficient gas recycling; instead, it is the Active Galactic Nuclei (AGN), i.e., the jet or radiation from the supermassive black hole at the centre of the galaxy, which have enough power to quench the high mass galaxies.

1.2.2 Hot and cold mode

As depicted by the galaxy properties in the previous section, gas represents the fuel for creating stars in galaxies. Hence, understanding gas accretion is a crucial key to unlock the scenario leading to the observed cosmic star-formation rate, the galaxies' colour bimodality and mass function.

From standard galaxy formation theory, the gas spherically accretes into the dark matter halo of a galaxy (Silk, 1977, Rees & Ostriker, 1977, White & Rees, 1978, Fall & Efstathiou, 1980, White & Frenk, 1991, Mo et al., 1998). The gas is then shock heated up to the virial temperature, defined using the virial theorem,

$$T_{\rm vir} \equiv \frac{1}{2}V_{\rm vir}^2 = \frac{1}{2}\frac{GM_{\rm vir}}{R_{\rm vir}}, \tag{1.8}$$

where $V_{\rm vir}$ is the virial velocity, $R_{\rm vir}$ the virial radius and $M_{\rm vir}$ the virial mass. The virial temperature is dependent on redshift through its mean density which can substitute either the virial mass or radius as explicitly shown in Sec. 1.2.3. For a halo of mass $M_{\rm h} \equiv M_{\rm vir} = 10^{12}\,{\rm M}_{\odot}$ at $z = 2$, $T_{\rm vir} \sim 10^6\,{\rm K}$. Once heated, the gas then cools down and starts triggering the star formation in the galaxy. This idealised picture faded with the emergence of the first cosmological simulations including hydrodynamics (Fardal et al., 2001, Kereš et al., 2005, Dekel & Birnboim, 2006, Ocvirk et al., 2008, Agertz et al., 2009, Dekel et al., 2009). From those simulations, a large amount of the gas accreting galaxies is never heated up to the virial temperature of the halo by shock, but rather remains cold ($T \lesssim 10^4\,{\rm K}$). Such cold accretion is depicted in Fig. 1.5. At early redshift, the gas falls inside the dark matter potential of the cosmic web where it is heated up to $\sim 10^4\,{\rm K}$ due to adiabatic compression. In over-dense regions, especially at the knot of filaments, galaxies form. The gas inside nearby then steadily accretes onto the galaxies. The gas already inside filaments connected to the knots remains cold and fuels the galaxy with gas cold enough to rapidly form stars. Finally, after redshift $z \sim 2$, the cold accretion does not penetrate well enough in the hot halo and ceases. The gas outside the galaxy follows a direct accretion scenario and is shock-heated up to $10^6\,{\rm K}$. This hot mode accretion needs the gas to cool down before it can trigger star formation. As shown in the sketch of Fig. 1.5, the galaxy also ejects gas from stellar and AGN feedbacks, which gas is re-accreted onto the galaxy, the so-called galactic fountain. The assembly of accretion modes, feedbacks, and fountains is referred to as the baryon cycle and forms the CircumGalactic medium (CGM), i.e., the gaseous halo around the galaxy.

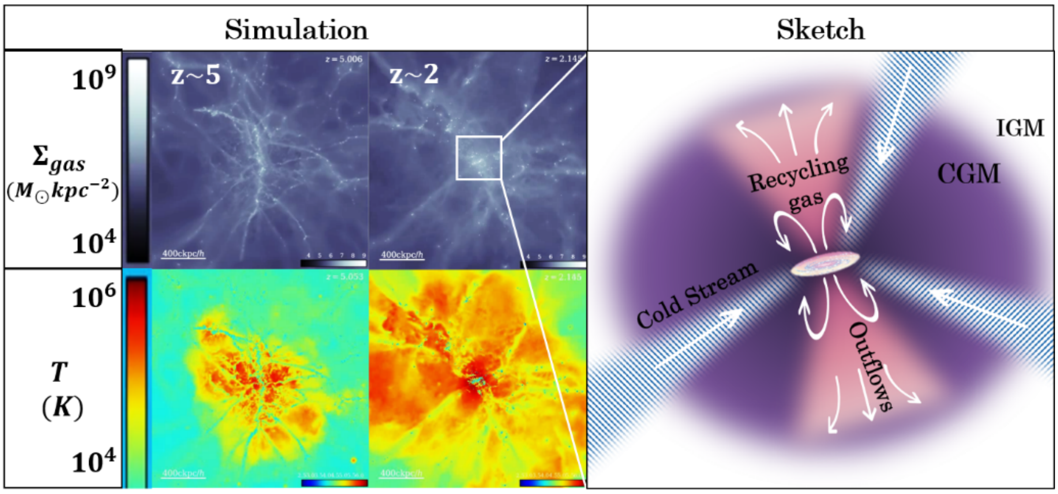

FIGURE 1.5: *Left panels:* Density and temperature maps of the gas around a forming galaxy at various redshift from a cosmological simulation of our group. Credit: K. Nagamine and I. Shimizu (see GADGET-3 simulations in Roca-Fàbrega et al., 2021). *Right panel:* Illustration of the resulting baryons processes inside the halo of the galaxy.

The accretion of cold gas flowing along the potential of filaments is called cold streams or cold flows and appears as a ubiquitous feature of ΛCDM cosmological simulations. Coming from the InterGalactic medium (IGM), the cold streams penetrate the hot halo of massive galaxies without being shock heated up to a redshift $z \sim 2$, enhancing the formation of stars in the galaxies. These cold accretions were already present in the early hydrodynamic cosmological simulations (Fardal et al., 2001) but were characterized as "cold streams" by the pioneering work of Dekel & Birnboim (2006), Dekel et al. (2009).

The strength of the cold stream accretion scenario is that it provides a natural physical explanation of the galaxy's properties. As the gas is already cold, the star formation in the Universe can be triggered soon after the Big Bang (Madau & Dickinson, 2014, Dayal & Ferrara, 2018). Also, the cessation of the cold accretion at $z \sim 2$ for massive haloes ($M_{\rm h} \sim 10^{12}\,{\rm M}_\odot$) also matches with the decrease of cosmic star formation. Dekel & Birnboim (2006) also shows that cold streams provide the physical mechanism leading to the galaxy bimodality, depicted in Fig. 1.6. From the left panel, cold streams accrete both massive and low mass haloes early ($z > 2$), with halo mass distinction defined by a threshold mass $M_{\rm shock}$ (the mathematical definition and derivation of $M_{\rm shock}$ is explained in the next section). This creates a population of star-forming galaxies. Then, after $z \sim 1-2$, the gas in the massive haloes becomes too hot which diffuses the cold streams and shut-down the cold-gas fueling for the massive haloes ($M_{\rm h} > M_{\rm shock}$). Those massive galaxies cease to form stars, leading to lower SFR and older stellar population, thus the red colour. For

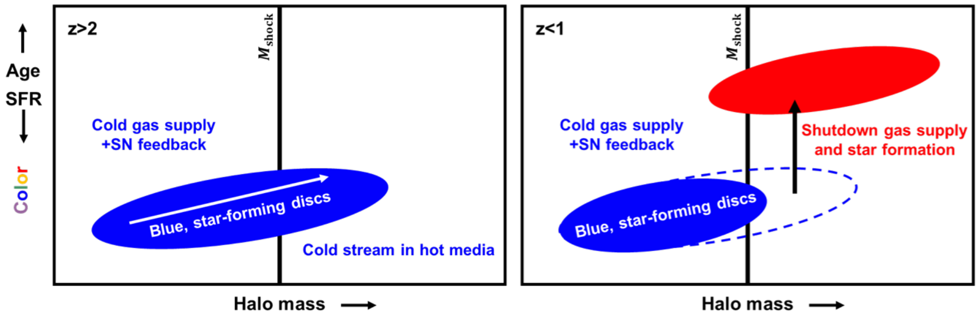

FIGURE 1.6: Galaxy colour bimodality explanation from cold stream accretion scenario. Source: Dekel & Birnboim (2006)

the late-type galaxies, their halo mass is relatively low allowing cold accretion and the formation of stars. They hence appear blue due to their high SFR.

1.2.3 Cold stream scenario

We now describe in more detail the background of the cold stream accretion scenario and its relationship with halo mass by summarizing the works of Birnboim & Dekel (2003) and Dekel & Birnboim (2006). The key parameters to understand the cold stream scenario are the halo mass threshold $M_{\rm shock}$ which defines if a halo is massive enough to support a stable accretion shock, and $M_{\rm stream}$ which defines at which redshift and halo mass the cold stream can no longer feed the galaxy in the presence of a stable shock.

The physical understanding of the stability of an accretion shock around a halo depends on the balance between the pressure gain from the compression of the gas due to the gravitational infall, and the pressure loss from radiative cooling. Starting from the energy equation in Lagrangian formulation,

$$\frac{\mathrm{d}e_{\rm i}}{\mathrm{d}t} = -P\frac{\mathrm{d}}{\mathrm{d}t}\left(\frac{1}{\rho}\right) + q, \tag{1.9}$$

where $e_{\rm i}$ is the internal energy per mass unit, ρ the density, P the pressure, γ the adiabatic index and q the radiative losses. Assuming an ideal gas equation of state $\rho e_{\rm i} = P(\gamma-1)^{-1}$, and considering that $\mathrm{d}_{\rm t}\left(\rho^{-1}\right) = -\rho^{-2}\dot{\rho}$, one can rewrite,

$$\frac{\dot{P}}{\dot{\rho}} = \frac{P}{\rho}\gamma - q \times \frac{\rho}{\dot{\rho}}\left(\gamma - 1\right),$$

which, after rewriting, allows to define an effective adiabatic index,

$$\gamma_{\rm e} \equiv \frac{\mathrm{d}\ln P}{\mathrm{d}\ln\rho} = \gamma - \frac{\rho}{\dot{\rho}}\frac{q}{e_{\rm i}} = \gamma - \Gamma^{-1}\frac{t_{\rm comp}}{t_{\rm cool}}, \tag{1.10}$$

with the compression time $t_{\rm comp} = \Gamma\rho/\dot{\rho}$, and the cooling time $t_{\rm cool} = e/q$. Γ is an arbitrary coefficient. The effective adiabatic index then allows the system state to account for the impact of radiative loss. Hence, a critical value $\gamma_{\rm crit}$ exists which defines the limit between a compression-driven system and a cooling-dominated system. In term of halo, a compression-driven system translates into a halo with a high dark matter potential, i.e. massive halo, while in the cooling-dominated system, the halo does not have a potential high enough to accelerate the gas and heat it up before it radiatively cools. From perturbation analysis, Birnboim & Dekel (2003) found that the halo can sustain a stable shock for

$$\gamma_{\rm e} > \gamma_{\rm crit} \ , \text{with } \gamma_{\rm crit} \equiv \frac{2\gamma}{\gamma + 2/3}. \tag{1.11}$$

Injecting this criterion inside equation 1.10, the conditions can be simplified as

$$t_{\rm comp} < t_{\rm cool}, \tag{1.12}$$

with a chosen $\Gamma \equiv (3 + 2\gamma^{-1})/(3\gamma - 4) = 21/5$ to cancel out extra terms. The computation of the cooling time is straightforward once one obtains the cooling rate. A full description of the computation of radiative cooling and cooling rate is given in Sec. 2.2. In their case, Dekel & Birnboim (2006) use

$$t_{\rm cool,h} \sim \frac{3}{2}\frac{k_{\rm b}T}{n\Lambda}, \tag{1.13}$$

with $k_{\rm b}$ the Boltzmann constant, T the temperature, n the gas number density and Λ the cooling rate function.

For the compression time, one can rewrite the expression using the conservation of mass such that

$$t_{\rm comp} = -\frac{\Gamma}{\nabla \cdot \mathbf{u}}. \tag{1.14}$$

Assuming a spherical infall of the gas leading to a spherical shock, Birnboim & Dekel (2003) found the equivalence relation $r/u = r_{\rm s}/u_{\rm post}$, with $r_{\rm s}$ the shock radius in the halo, and u_1 the post-shock radial velocity. Hence, $\nabla \cdot \mathbf{u} \sim 3u_{\rm post}/r_{\rm s}$. Using the Rankine-Hugoniot jump condition in the halo frame where the shock can expand,

$$u_{\rm pre} - u_{\rm s} = \frac{\gamma + 1}{\gamma - 1}\left(u_{\rm post} - u_{\rm s}\right), \tag{1.15}$$

with $u_{\rm pre}$ the pre-shock velocity, i.e., the velocity in the halo, and $u_{\rm s}$ the shock velocity. In the case of a stable shock, Dekel & Birnboim (2006) found $u_{\rm s} \sim -u_{\rm post}$, leading to $u_{\rm pre} \sim u_{\rm post} \times (\gamma+3)/(\gamma-1)$. Considering that in the halo $u_{\rm post} \sim V_{\rm vir}$, $V_{\rm vir}$ being the Virial velocity, $r_{\rm s} \sim R_{\rm vir}$ the Virial radius, $T = T_{\rm vir}$ the virial temperature, and with $\gamma = 5/3$, the ratio of both timescale becomes,

$$\frac{t_{\rm comp}}{t_{\rm cool,h}} \sim 0.1 \frac{R_{\rm vir} n \Lambda}{k_{\rm b} T_{\rm vir} V_{\rm vir}}. \tag{1.16}$$

Finally, to express this relation as a ratio of halo mass over a threshold mass, we can use the virial theorem $0.5V_{\rm vir}^2 = k_{\rm b}T_{\rm vir}/m$ and $V_{\rm vir}^2 = GM_{\rm vir}/R_{\rm vir}$. Under the assumption that the cooling curve can be expressed as $\Lambda \sim a \times T^{-1}$ with a any remaining coefficient, it is obtained,

$$\frac{t_{\rm comp}}{t_{\rm cool,h}} \sim \left(\frac{M_{\rm shock}}{M_{\rm vir}}\right)^{4/3}, \tag{1.17}$$

with $M_{\rm shock}^{4/3} = (0.3R_{\rm vir}k_{\rm b}an) \,/\, \left(V_{\rm vir}mG^2\pi^2\rho\right)$.

Similarly, one can obtain the same expression for stream stability inside a halo with the stream density relation $\rho_{\rm stream}/\rho_{\rm vir} \sim (3M_*/M)^{-2/3}$ derived from simulations (Dekel & Birnboim, 2006), with M_* the halo mass in function of time which can be defined using Press-Schechter characteristic mass (Press & Schechter, 1974, Sheth & Tormen, 2002)[3].

The stability relation for a stream is then,

$$\frac{t_{\rm comp}}{t_{\rm cool,stream}} \sim \left(\frac{M_{\rm vir}}{3M_*}\right)^{2/3} \left(\frac{M_{\rm shock}}{M_{\rm vir}}\right)^{4/3}. \tag{1.18}$$

$M_{\rm stream}$ is then obtained when $t_{\rm comp}/t_{\rm cool,stream} = 1$,

$$M_{\rm stream} \sim \frac{M_{\rm shock}^2}{3M_*}. \tag{1.19}$$

The resulting accretion modes are shown in Fig. 1.7. The limit of shock stability $M_{\rm shock}$ (red curve) shows a roughly constant value $10^{12}\rm M_\odot$[4], but only defines the cold to hot accretion mode from a redshift $z \sim 1$. Above this redshift, the cold stream can still survive inside the halo leading to the cold in hot regime. The limit for the cold stream stability $M_{\rm s}$ (magenta line) can be roughly define as $\log M_{\rm stream} \sim \log M_{\rm shock} + 1.11 \times (z - 1.4)$ (Daddi et al., 2022). The two dashed black curves show the typical evolution of a halo for different initial overdensities. Hence, despite having a stable shock, massive haloes can still be fed by cold streams up to $z \sim 2$, while haloes exceeding $M_{\rm shock}$ at $z \lesssim 1.5$ cannot sustain any more cold accretion.

[3] Also see Dekel & Birnboim (2006, appendix 3).

[4] To note, the red line representing $M_{\rm shock} \sim 6 \times 10^{11}\rm M_\odot$ is in reality the one for a stable shock at $r_{\rm s} = 0.1R_{\rm vir}$ in the the halo. However, to ease the calculus explained in this section, we only describe the simplest case $r_{\rm s} = R_{\rm vir}$. This does not drastically change the discussion as in the case $r_{\rm s} = R_{\rm vir}$, $M_{\rm shock} \sim 2 \times 10^{12}\rm M_\odot$ which is about $\sim 10^{12}\rm M_\odot$.

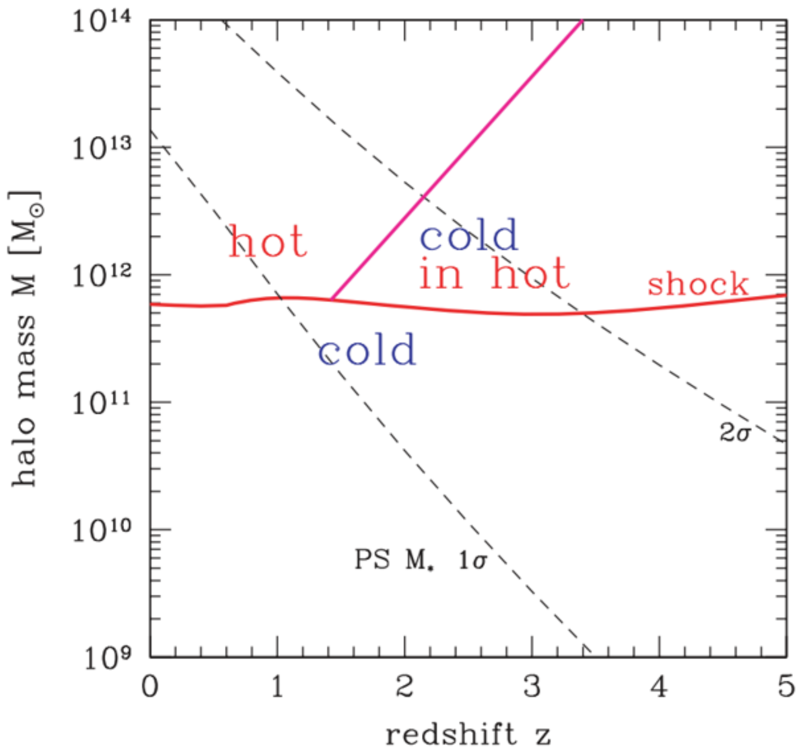

FIGURE 1.7: Gas accretion modes depending on the halo mass. Source: Dekel & Birnboim (2006)

Such disappearance of the cold mode at $z \sim 2$ correlates well with the drop of cosmic star formation in Fig. 1.4 and provides an analytical framework to explain the galaxy bimodality (see Fig. 1.6).

1.2.4 The current challenge

Recent observational evidence increasingly supports the concept of cold stream accretion (Behroozi et al., 2019; Daddi et al., 2022a, 2022b), but direct observations of these cold streams remain relatively few compared to the large sample of observed galaxies. Observing cold inflow typically involves detecting Mg II and Fe II absorption lines in the spectra of systems with background quasars or galaxies (Giavalisco et al., 2011, Rubin et al., 2012, Martin et al., 2012, Bouché et al., 2013, 2016, Zabl et al., 2019), as well as H I gas (Turner et al., 2017, Chen et al., 2020, Fu et al., 2021). The scarcity of detections in such absorption line systems can be attributed to the limited covering fraction of cold streams compared to the halo's surface area (Faucher-Giguère & Kereš, 2011). On the other hand, emissions-based observations of Lyα emitters have unveiled filamentary structures in or near the halos of high-redshift galaxies (e.g., Cantalupo et al., 2014, Fumagalli et al., 2016, Borisova et al., 2016, Umehata et al., 2019) and systems which emissions align with cold inflow patterns (e.g., Battaia et al., 2018, Christopher Martin et al., 2019). For instance, Daddi et al. (2021) used Lyα emissions to identify distinct cold filamentary gas structures encompassing massive galaxies at redshift $z = 2.9$. In addition, Emonts et al. (2023) detected cold filamentary gas structures using observations of neutral carbon (C i) emissions at $z = 3.8$, while Zhang et al. (2023) identified emissions consistent with inspiraling streams around a galaxy at redshift $z = 2.3$ through Lyα and metal lines. These observations offer direct evidence for the presence of cold streams in the proximity of these galaxies, although they also underscore the challenge of linking these emissions to cold streams. Therefore, understanding the emission signatures of cold streams constitutes a crucial step in confirming their prevalence beyond the realm of cosmological simulations.

Concurrently, recent efforts have been made to examine the impact of simulation resolution on gas properties within the halo, particularly in the circumgalactic medium (CGM) (Peeples et al., 2019, van de Voort et al., 2019, Hummels et al., 2019, Suresh et al., 2019, Nelson et al., 2020, Bennett & Sijacki, 2020). Bennett & Sijacki (2020) observed that a mass resolution 512 times higher around shocks results in a CGM with approximately 50% denser cold gas and about 25% more inflow than their standard case, presenting a significantly more multiphase and turbulent CGM than the conventional state-of-the-art cosmological simulations. It is worth noting that they did not fully attain convergence at their highest resolution. Nelson et al. (2020) further demonstrates that a resolution finer than $\Delta x < 100\,\mathrm{pc}$ is necessary for fully resolving the small-scale cold gas structures in the CGM of massive galactic haloes ($M_{\mathrm{h}} > 10^{12}, \mathrm{M}_{\odot}]$) at redshift $z = 0.5$. In the context of cold stream accretion, insufficient resolution hinders the development of Kelvin-Helmholtz Instabilities (KHI) at the interface between the cold, dense stream and the hot, diffuse CGM. These instabilities, initially explored by Mandelker et al. (2016), can shorten the stream's lifetime. Considering that most cosmological simulations maintain a typical CGM resolution near the virial radius of approximately $\sim 1\,\mathrm{kpc}$, it underscores the necessity to investigate the evolution of cold streams using high-resolution simulations.

To gain insights into both the evolution and emission characteristics of cold streams, a series of numerical studies have been conducted, assuming idealized stream geometries. Mandelker et al. (2016) conducted a linear analysis, while Padnos et al. (2018) delved into 2D hydrodynamic (HD) simulations. Mandelker et al. (2019) expanded this further with 2D and 3D HD simulations, all revealing that cold streams face disruptions from Kelvin-Helmholtz Instability (KHI) surface modes and body modes, the latter one also known as reflective modes. The dominant disruptive modes are the surface one, which are characterized by the highest growth rates. Aung et al. (2019) focused on the effect of self-gravity, which have the potential to induce stream fragmentation through gravitational instabilities. Building upon this, Berlok & Pfrommer (2019b) employed 2D and 3D magnetohydrodynamic (MHD) simulations to examine the impact of magnetic fields parallel to the stream. Their findings indicated that sufficiently strong fields ($B \gtrsim 0.3$–$0.8\,\mu$G) could aid in shielding the stream from KHI. Vossberg et al. (2019) conducted 2D HD simulations to investigate the formation of over-dense regions in the stream due to KHI growth. While these studies predominantly focused on the evolution of cold streams, Mandelker et al. (2020a) brought valuable insights into the understanding of their characteristics emissions by including radiative cooling into HD simulations. This work demonstrated a cooling emission scaling inversely with the cooling time, roughly as $\propto t_{\rm cool}^{-1/4}$. Analytical considerations by Mandelker et al. (2020b) further reinforced these findings putting them in cosmological context and revealing that cold streams with a radius exceeding 3 kpc can exhibit Lyα luminosities surpassing $L_{\rm Ly\alpha} > 10^{42}\,{\rm erg\,s^{-1}}$ for halo masses $M_{\rm h} > 10^{12}\,{\rm M_\odot}$ at a redshift of approximately $z \sim 2$.

1.3 Scope of the thesis

1.3.1 What is missing ?

The mixing between the hot CGM gas (with a temperature of $T_{\rm cgm} \sim 10^6\,{\rm K}$) and the cold stream gas (with a temperature of $T_{\rm s} \sim 10^4\,{\rm K}$) is the key mechanism leading to the cold stream emission. This interaction results in a gas mixture with an intermediate temperature ($T_{\rm mix} < 10^5\,{\rm K}$), which has a significantly higher cooling rate by several orders of magnitude (Begelman, 1990).

Such mechanism has been studied by Gronke & Oh (2018, 2020) from simulations of cold clouds embedded within a hot galactic wind. These studies demonstrated that the condensation/mixing velocity and the cooling emission of the cloud scale with the cooling time in the mixing layer, approximately as $\propto t_{\rm cool}^{-1/4}$. Similar scaling has been found in higher-resolution shear layer simulations by Fielding et al. (2020) and Tan et al. (2021, for their strong cooling case). In contrast, Ji et al. (2019) and Tan et al. (2021, for their weak cooling case) found a scaling of approximately $\propto t_{\rm cool}^{-1/2}$. Further works have also explored the impact of high Mach numbers (Yang & Ji, 2023). Consequently, in the context of HD simulations with radiative cooling, it is possible to predict the evolution of the cold stream in terms of mass flux and emission by estimating the cooling time within the mixing layer.

The implications of introducing additional physics, such as magnetic fields and thermal conduction, in conjunction with radiative cooling for the analysis of cold streams remain an open question. Valuable insights can be gained from simulations involving cold clouds within the CGM. In 2D hydrodynamic (HD) simulations, Armillotta et al. (2017) shows that isotropic thermal conduction can impede the growth of Kelvin-Helmholtz Instabilities (KHI) and extend the survival of cold clouds. In 3D simulations, Hidalgo-Pineda et al. (2023) explored the influence of magnetic fields, concluding that the magnetic fields can contribute to stabilizing the cloud against KHI, thereby prolonging its lifespan. Brüggen & Scannapieco (2023) conducted 3D magnetohydrodynamic (MHD) simulations, examining both isotropic and anisotropic thermal conduction at various magnetic field angles. Their findings demonstrate that both magnetic fields and thermal conduction can hinder KHI growth, in other the development of the mixing layer, leading to extended cloud survival. In 3D MHD simulations with self-gravity, star formation, thermal conduction, and other physics, Sander & Hensler (2021) explored high-velocity clouds within the CGM. Their work concluded that thermal conduction also contributes to cloud stability while simultaneously causing the diffusion of cold gas substructures separated from the cloud, such as in the cloud tail.

In summary, a crucial mechanism impacting the emission signature and evolution of cold streams is the mixing of the CGM gas and the stream gas from Kelvin-Helmholtz Instabilities (KHI) . Notably, the emission emanating from the mixing layer is Lyα-dominated, potentially correlates with observed Lyα emitters. However, simulations involving cold clouds within the hot CGM reveal that magnetic fields at varying angles and thermal conduction can each influence KHI growth. The reduction in the KHI growth rate can extend the survival of cold streams but may concurrently diminish their emission. Consequently, this thesis work aim to address this gap through an extensive suite of 2D magnetohydrodynamic (MHD) simulations (approximately 120 simulations). These simulations encompass radiative cooling and anisotropic thermal conduction, allowing a comprehensive parameter study, including distinct stream velocities, CGM/stream densities, and magnetic field angles, across hydrodynamic (HD), MHD, and MHD simulations with thermal conduction (MHD+TC).

1.3.2 Thesis structure

First, the fundamental physical processes in our simulations, the cold stream and CGM properties and the idealized model are described in Chapter 2.

Chapter 3 presents the numerical set-up the simulation suite, presenting the governing equations, the computational methods and the initial conditions.

Chapter 4 describes the simulations results and analysis, first by a general comparison and then focusing on the impact of the magnetic field and the thermal conduction.

We discuss the extent of our results from a cosmological perspective in Chapter 5, assessing both the cold streams emissions and properties.

Finally, Chapter 6 draw the conclusion of this thesis along with an illustrative manga summary of our main findings.

Chapter 2

Cold stream model and physical processes

2.1 Typical parameters of cold streams

2.1.1 Observations

Our selection of parameters for the stream model aligns with those employed in previous numerical investigations of idealized cold streams (see, e.g., Berlok & Pfrommer, 2019b, Mandelker et al., 2020a).

Observations involving absorption primarily utilize Mg II and Fe II lines (Giavalisco et al., 2011, Rubin et al., 2012, Martin et al., 2012, Bouché et al., 2013, 2016, Zabl et al., 2019) or focus on H I gas (Turner et al., 2017, Chen et al., 2020, Fu et al., 2021). Emission-based observations have unveiled filamentary structures using Lyα (e.g., Cantalupo et al., 2014, Borisova et al., 2016, Umehata et al., 2019, Daddi et al., 2021) and C I lines (Emonts et al., 2023). These observations have also detected lines consistent with the emission originating from inspiraling cold streams (Battaia et al., 2018, Christopher Martin et al., 2019, Zhang et al., 2023). These studies have predominantly targeted massive haloes with $M_{\rm h} < 10^{11}\,{\rm M}_\odot$, spanning a range of redshifts from $z \sim 0.4$ (Martin et al., 2012, Christopher Martin et al., 2019) to $z \sim 3.8$ (Emonts et al., 2023). The neutral hydrogen column densities in these observations cover a broad spectrum, ranging from $10^{17}\,{\rm cm}^{-2}$ to $10^{21}\,{\rm cm}^{-2}$, with metallicities spanning from $10^{-3.8}\,{\rm Z}_\odot$ to $1\,{\rm Z}_\odot$.

2.1.2 Simulations and analytical model

Building upon a cosmological simulation, Dekel et al. (2013) developed an idealized model for star-forming galaxies within massive haloes ($M_{\rm h} > 10^{11}\mathrm{M}_\odot$) at $z > 1$ with the following virial radius and velocity:

$$R_{\rm v} \sim 100 \left(\frac{M_{\rm v}}{10^{12}\mathrm{M}_\odot}\right)^{1/3} \left(\frac{3}{1+z}\right) \mathrm{kpc}\,, \tag{2.1}$$

$$V_{\rm v} \sim 200 \left(\frac{M_{\rm v}}{10^{12}\mathrm{M}_\odot}\right)^{1/3} \left(\frac{3}{1+z}\right)^{1/2} \mathrm{km\,s^{-1}}\,, \tag{2.2}$$

where $M_{\rm v}$ is the virial mass of the halo and is taken as $10^{12}\,\mathrm{M}_\odot$.

For halo masses around $10^{12}\,\mathrm{M}_\odot$ at approximately $z \sim 2$, cosmological simulations (Goerdt et al., 2010) and analytical extensions of Dekel et al. (2013) model (Padnos et al., 2018, Mandelker et al., 2020a,b) yield the following characteristics for cold streams:

- A stream number density of $n_{\rm s} \sim 10^{-3}$–$10^{-1}\,\mathrm{cm^{-3}}$.
- A density ratio (δ) defined as the stream density over the CGM density, with values ranging from $\delta \sim 30$–300.
- A stream radius ($R_{\rm s}$) spanning 3–50 kpc.
- A Mach number based on the CGM sound speed ($\mathcal{M}_{\rm cgm}$) within the range $\mathcal{M}_{\rm cgm} \sim 0.75$–$2.25$.

Regarding metallicities, cosmological simulations provide more stringent constraints compared to observations:

- For stream metallicities ($Z_{\rm s}$), values around 10^{-2}–10^{-1} are estimated (Goerdt et al., 2010).
- CGM metallicities ($Z_{\rm cgm}$) at the virial radius exhibit a range from $10^{-2}\,\mathrm{Z}_\odot$ (Roca-Fabrega et al., 2019, i.e., the lower value) to $10^{-0.5}\,\mathrm{Z}_\odot$ (Strawn et al., 2021, i.e., the average value).

Consistently with previous work, we target three number densities $n_{\rm s} = 10^{-3}, 10^{-2}, 10^{-1}\,\mathrm{cm^{-3}}$, along with two density ratios $\delta \equiv \rho_{\rm s}/\rho_{\rm cgm} = 30, 100$, one set of stream/CGM metallicities $(Z_{\rm s}, Z_{\rm cgm}) = \left(10^{-1.5}, 10^{-1}\right)\,\mathrm{Z}_\odot$, and three different stream Mach number $\mathcal{M} = \mathcal{M}_{\rm cgm} = 0.5, 1, 2$. We also choose to fix the stream radius $R_{\rm s} = 1\,\mathrm{kpc}$.

2.1.3 Magnetic field in the CGM

Our understanding of the magnetic field in the large-scale structure of the Universe remains incomplete. The primordial magnetic field has been constrained to a lower limit of $\sim 10^{-10} - 10^{-9}\,\mu$G (Neronov & Vovk, 2010, Dolag et al., 2011). Although the evolution of the primordial magnetic field has been theorized (Saveliev et al., 2012), it may be more reliable to focus on magnetic fields that have been studied in recent simulations and observations of the CGM.

Little is known about the properties of the magnetic field in the CGM of high-redshift galaxies. Most zoom-in simulations are focused on the magnetic field strength growth (Rieder & Teyssier, 2017, Martin-Alvarez et al., 2018) and morphology (Pakmor et al., 2017, 2018, Steinwandel et al., 2019) in the galactic disc due to the small-scale dynamo. Therefore, to better understand the composition and magnetic morphology of the CGM, we may rely on CGM-focused simulations. Simulations from the Auriga project (Pakmor et al., 2020) and FIRE project (Hopkins et al., 2020) have investigated the evolution of the magnetic field in the CGM, providing estimates of the magnetic field strength ranging from 10^{-3} µG to 10^{-2} µG at the virial radius and for redshift $z \sim 2$. The evolution of galactic and near CGM magnetic fields generally follows three phases. First, there is exponential growth during the gravitational collapse of baryonic matter into the dark matter potential. This is followed by a linear growth phase during accretion and eventually stabilizing and oscillating during the feedback phase.

Observations of the near-center CGM gas have put upper constraints on the magnetic field strength, but probing the magnetic field at high-redshift halos is challenging. Using fast radio bursts (FRBs), Prochaska et al. (2019) have constrained the magnetic field to a range of $6\,10^{-2} - 2\,\mu$G for electron density range of $10^{-5} - 10^{-3}\,\mathrm{cm}^{-3}$ inside the hot halo ($T_{\mathrm{cgm}} \sim 10^6$K). It should be noted that this constraint applies only to the magnetic field parallel to the line of sight. This is consistent with the previous Faraday Rotation Measure (FRM) study by Bernet et al. (2008), which constrained the magnetic field to be $10\,\mu$G for $N_{\mathrm{HI}} = 10^{19}\,\mathrm{cm}^{-2}$. The study by Lan & Prochaska (2020) of over 1000 FRMs in low-redshift galaxies ($z < 1$) provides a lower constraint of $2\,\mu$G for the upper limit of the coherent magnetic field. Since the magnetic field in the halo grows with time, the magnetic field strength found by Lan & Prochaska (2020) is expected to represent a higher value than the one of CGM at higher redshift. Hence, our motivation to investigate the effects of a low magnetic field.

In their study, Berlok & Pfrommer (2019b) investigated the impact of magnetic fields that are aligned with the cold stream on KHI growth, using a magnetic field strength of approximately 1 μG. This strength is higher or in the upper limit range than what some observations and simulations suggest (Prochaska et al., 2019, Pakmor et al., 2020, Hopkins et al., 2020) for cold stream at the Virial radius. This high magnetic field strength was chosen to explore a range of dynamically relevant magnetic field strengths for cold streams without radiative cooling ($\beta < 100$) when the magnetic field is parallel to the stream. In our cases, we investigate cases where the magnetic field is not parallel to the stream in which cases an amplification of the magnetic field strength can be expected. Hence, we assume a lower magnetic field strength of $B \sim 10^{-3}\,\mu$G defined by an initial ratio of thermal pressure over magnetic pressure $\beta = p/p_{\mathrm{mag}} 10^5$ for our study. One shall see that despite this initially insignificant value of magnetic field strength, this one can impact the cold stream evolution.

Berlok & Pfrommer (2019b) investigated the impact of a magnetic field aligned with the cold stream on the growth of KHI, using a magnetic field strength of approximately 1 μG. This relatively high magnetic field strength was chosen to explore a range of dynamically relevant magnetic field strengths for cold streams without radiative cooling ($\beta \leq 100$), when the magnetic field is parallel to the stream. In our work, we investigate a magnetic field with various angles in which cases an amplification of the magnetic field strength can be expected. Hence, we focus on a lower magnetic field strength of $B \sim 10^{-3}$ μG defined by an initial ratio of thermal pressure over magnetic pressure $\beta = p/p_{\mathrm{mag}} = 10^5$ for our study. This gives an Alfvenic time-scale,

$$t_{\mathrm{a}} \sim R_{\mathrm{s}}/v_{\mathrm{a}}, \tag{2.3}$$

with the Alfven speed $v_{\mathrm{a}} = B_0/\sqrt{\rho}$. From the sound crossing time of the stream, defined as $t_{\mathrm{sc}} = 2R_{\mathrm{s}}/c_{\mathrm{s}}$, the Alfvenic time can be expressed as $t_{\mathrm{a}} \sim 0.5 t_{sc} c_{\mathrm{s}}/\left(2\beta\right)^{0.5} \sim 100\, t_{\mathrm{sc}}$, which means that the Alfvenic time can be initially ignored.

2.2 Radiative cooling-heating model

2.2.1 Basis of photo-chemistry

At a given temperature and density, the internal energy of a gas can be strongly affected by chemical processes. Collision, recombination, or Bremsstrahlung process can lead to the emission of photons which decrease the internal energy of the gas, ultimately decreasing its temperature and increasing its density. Similarly, heating processes such as background radiations can also modify the gas thermodynamical state. Considering the cooling and heating is then primordial to reproduce a realistic evolution of the gas and to understand its emission. Cen (1992), Katz et al. (1996), Thoul & Weinberg (1996) were among the first to include the gas chemistry in astrophysical-cosmological simulations. We hereby describe the basics principle of a chemistry solver. Considering a gas made of hydrogen and helium, and assuming the gas being optically thin and in ionization equilibrium, the number density of each species is given by,

$$\begin{cases} \Gamma_{\mathrm{eH_0}} n_{\mathrm{e}} n_{\mathrm{H_0}} + \Gamma_{\gamma \mathrm{H_0}} n_{\mathrm{H_0}} = \alpha_{\mathrm{H_+}} n_{\mathrm{H_+}} n_{\mathrm{e}}, \\ \Gamma_{\mathrm{eHe_0}} n_{\mathrm{e}} n_{\mathrm{He_0}} + \Gamma_{\gamma \mathrm{He_0}} n_{\mathrm{He_0}} = \left(\alpha_{\mathrm{He_+}} + \alpha_{\mathrm{d}}\right) n_{\mathrm{He_+}} n_{\mathrm{e}}, \\ \Gamma_{\mathrm{eHe_+}} n_{\mathrm{e}} n_{\mathrm{He_+}} + \Gamma_{\gamma \mathrm{He_+}} n_{\mathrm{He_+}} + \left(\alpha_{\mathrm{He_+}} + \alpha_{\mathrm{d}}\right) n_{\mathrm{He_+}} n_{\mathrm{e}} = \alpha_{\mathrm{He_{++}}} n_{\mathrm{He_{++}}} n_{\mathrm{e}} + \\ + \Gamma_{\mathrm{eHe_0}} n_{\mathrm{e}} n_{\mathrm{He_0}} + \Gamma_{\gamma \mathrm{He_0}} n_{\mathrm{He_0}}, \\ \alpha_{\mathrm{He_{++}}} n_{\mathrm{He_{++}}} n_{\mathrm{e}} = \Gamma_{\mathrm{eHe_+}} n_{\mathrm{e}} n_{\mathrm{He_+}} + \Gamma_{\gamma \mathrm{He_+}} n_{\mathrm{He_+}}, \end{cases} \tag{2.4}$$

where the creation (destruction) of hydrogen and helium atoms and ions are desbribed from the right-hand sides (left-hand sides). Γ_{eX}, α_{X}, $\Gamma_{\gamma \mathrm{X}}$ are the collisional ionization rate, recombination rate, and photoionization rate of a given specie X and whose expressions in function of temperature can be found in Black (1981), Cen (1992), Katz et al. (1996). Along side equations 2.4, the charge neutrality condition and the number density conservation of the species and electrons leads to a system of six equations (see Katz et al., 1996, equations 33-38), whose solutions is the number density of each species and electrons. Once the number densities are known, one can recover the cooling and heating rates of each processes in function of the species number densities and temperature Katz et al. (see 1996, Table 1). To solve such system of equations, one may use numerical methods such as common zero or minimum search algorithm (e.g. Newton-Raphson method). We provide in Appendix C a simple Matlab code example to solve the equations and recover the cooling and heating rates. Illustrative results from Katz et al. (1996) and our own code are shown in Fig. 2.1 for a gas with primordial composition and without photoionization. For temperature below 10^6 K, cooling is dominated by the two distinctive peaks of hydrogen and helium collisional excitation, while for higher temperature, the free-free emission (Bremsstrahlung) dominates.

Multiple approaches for (M-)HD simulations exist in order to include the cooling and heating rates. The most realistic one consist in solving the gas chemistry on-the-fly during the simulations using an in-house chemistry solver (Cen, 1992, Thoul & Weinberg, 1996, Katz et al., 1996). A more efficient approach is to pre-compute the cooling and heating rates of the assumed gas as a function of temperature, density and metallicity, and store them in tables before running the simulation.

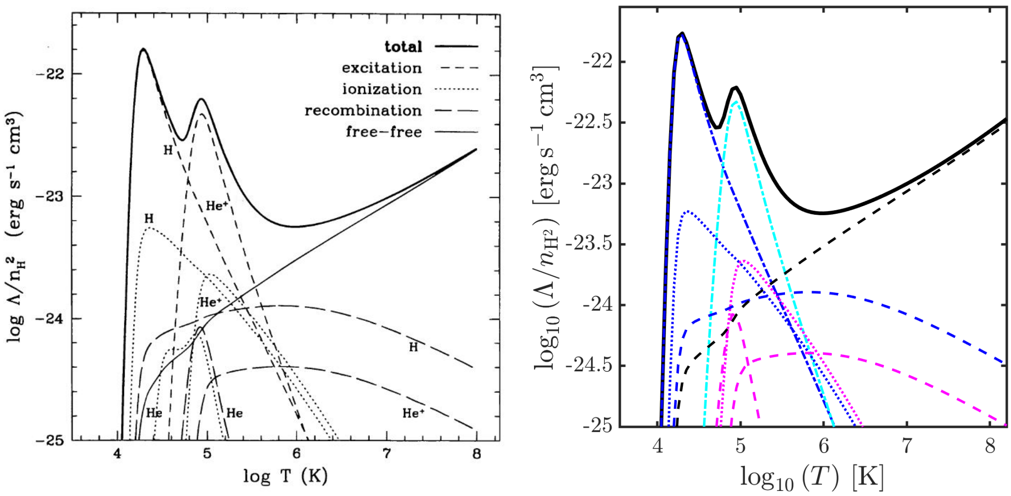

FIGURE 2.1: Net cooling curves (no photoionization) solving equations 2.4 for a gas at primordial composition. *Left panel:* reference figure from Katz et al. (1996, Fig. 1), with in legend the processes represented by each line. *Right panel:* Our results using our own algorithm.

Then, during the simulation, the rates are interpolated using the tabulated values (see the GRACKLE library Smith et al., 2017, for example). To mention, in the case where the temperature range is limited and where the cooling is dominated by mainly one process, assuming collisional ionization equilibrium (no photoionization, e.g., $\Gamma_{\gamma \mathrm{X}} = 0$), one can simply approximate the cooling rate as a power-law function. Such approach is not relevant for our parameter range.

2.2.2 CLOUDY model

The above model only consider a gas made of hydrogen and helium and do not consider additional cooling from heavier elements. While the equations philosophy remain the same, adding more elements increases drastically the number of equations of the system leading to tedious calculus which is beyond the scope and time frame of this work. One may rely on existing photoionization code such as CLOUDY to solve the photo-chemistry. We use the version C17 of CLOUDY (Ferland et al., 2017) considering the redshift-dependent UV-background heating derived from observational data of galaxies and quasars from Haardt & Madau (2012). The tables are generated for temperatures ranging from 10^3 K to 10^6 K with a $\log_{10}(\Delta T) = 0.05$ intervals (61 points), for for number densities ranging from $10^{-6}\,\mathrm{cm}^{-3}$ to $1\,\mathrm{cm}^{-3}$ with intervals of $\log_{10}(\Delta n) = 0.5$ (13 points), and for the CGM and stream metallicities Z_{cgm} and Z_{s}. The heating rates from Haardt & Madau (2012) are considered for a redshift $z = 2$. The CLOUDY input to generate our tables is shown in Appendix D.

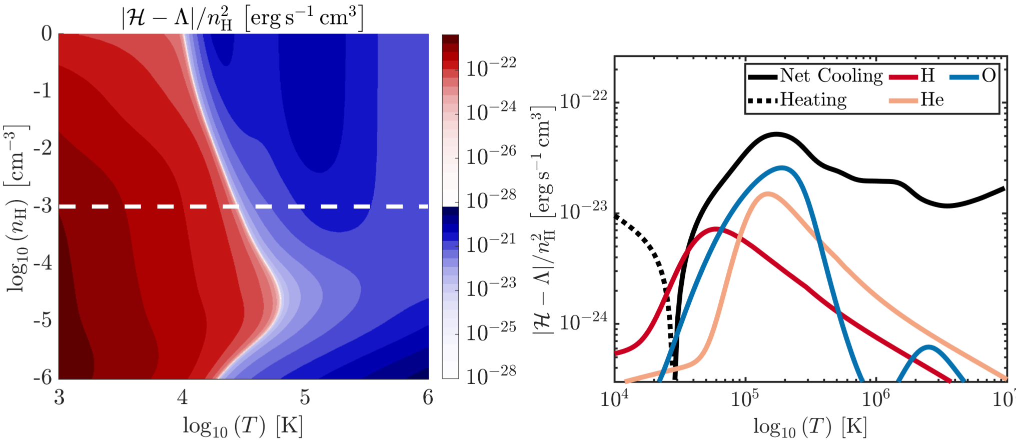

FIGURE 2.2: Net cooling-heating map from our CLOUDY model considering a metallicity of $Z = 0.1\mathrm{Z}_\odot$. *Left panel:* the red and blue colorscale represents heating and cooling scaling, respectively. The white dashed line refers to the fixed density curve represented in the right panel. *Right panel:* Net heating-cooling curve in function of temperature at a fixed number density $n_{\rm H} = 10^{-3}\,\mathrm{cm}^{-3}$. The contributions of heating and cooling are shown in dashed line and plain lines, respectively. Color lines refer to the main species composing the cooling for temperature under 10^6 K.

Figure 2.2 presents the resulting cooling/heating map for the assumed CGM metallicity of $Z_{\rm cgm} = 0.1\,\mathrm{Z}_\odot$. The left panel presents logarithmic scales of the heating and cooling rates in red and blue color maps, where the white region denotes near-equilibrium states. The red region is dominated by heating, while the blue region is dominated by cooling. The right panel shows the net cooling/heating curves of a typical gas in the mixing layer between the stream and the CGM with number density $n_{\rm mix} = 10^{-3}\,\mathrm{cm}^{-3}$. The color lines represent the total cooling from the main species in our temperature region. In our relevant range of gas temperature $T < 10^5$ K, hydrogen cooling is crucial due to the Lyα cooling which leads to the hydrogen cooling peak near $10^{4.3}$. Heavy elements cooling can also contribute especially for temperature tending to 10^5 K. As seen in the colormap, the higher is the density, and the more pronounced are the hydrogen and helium cooling peaks which are described in Figure 2.1.

2.2.3 Stream temperature and cooling time

From cosmological simulations, cold streams are expected to have temperature $\leq 10^4$ K defined by the balance of cooling and heating radiations. Their temperatures can drops down to $\sim 10^3$ K if they are self-shielded, leading to denser stream (Fumagalli et al., 2011).

We determine the initial temperature of the stream from the heating-cooling radiation balance

$$\mathcal{H}_{n_{\rm H}}\left(T_{\rm s}\right) - \Lambda_{n_{\rm H}}\left(T_{\rm s}\right) = 0, \tag{2.5}$$

where $\mathcal{H}$ is the heating rate and Λ is the cooling rates, respectively. This gives stream temperatures of $T_{\rm s} \sim (1.3, 1.9, 3.1) \times 10^4\,{\rm K}$ for $n_{\rm s} = (10^{-1}, 10^{-2}, 10^{-3})\,{\rm cm}^{-3}$, respectively. Our temperatures values are well-aligned with other results from cosmological or idealized simulations. Such thermal equilibrium of the cold stream is also needed in our initial conditions to avoid unrealistic over-heating or over-cooling of the stream in the simulation. Assuming an isobaric cooling, the resulting cooling time for gas in the mixing layer at temperature $T_{\rm mix}$ is

$$t_{\rm cool} = \frac{T_{\rm mix} k_{\rm b}}{\left(\gamma - 1\right) n_{\rm mix} \Lambda_{\rm net,mix}}, \tag{2.6}$$

where the net cooling-heating rate $\Lambda_{\rm net,mix} = \mathcal{H}_{n_{\rm mix}}\left(T_{\rm mix}\right) - \Lambda_{n_{\rm mix}}\left(T_{\rm mix}\right)$ is defined by the number density and temperature in the mixing layer between the stream and the CGM. The value of the mixing layer number density and temperature are defined in the subsequent section.

2.3 KHI and Mixing layer

2.3.1 Linear perturbation theory

Kelvin-Helmholtz instability is a famous type of instability happpening at the interface of shear flows. It's behaviour for incompressible fluid dynamics is a basics of many textbooks (e.g. Chandrasekhar, 1961). In the compressible regime, KHI has been analyticaly studied in the context of jets (Payne & Cohn, 1985, Norman & Hardee, 1988, Hardee, 1987, Hardee & Norman, 1988, Ferrari et al., 1978, Bodo et al., 1994, Birkinshaw, 1984) and was more recently applied to a cold phase inside a hot CGM by Mandelker et al. (2016) and Berlok & Pfrommer (2019a). Following the work of Mandelker et al. (2016), we hereby provide a brief description of the behaviour of KHI for compressible hydrodynamics for a simple sheet geometry.

The governing system of equations is the Euler system,

$$\begin{cases} \dfrac{\partial \rho}{\partial t} + \left(\nabla \cdot \boldsymbol{u}\right)\rho + \left(\boldsymbol{u} \cdot \nabla\right)\rho = 0, \\ \rho \dfrac{\partial \boldsymbol{u}}{\partial t} + \rho\left(\boldsymbol{u} \cdot \nabla\right)\boldsymbol{u} + \nabla P = 0, \\ \dfrac{\partial P}{\partial t} + \left(\boldsymbol{u} \cdot \nabla\right) P - c^2 \left[\dfrac{\partial \rho}{\partial t} + \left(\boldsymbol{u} \cdot \nabla\right)\rho\right] = 0, \end{cases} \tag{2.7}$$

with $\boldsymbol{u} = (u, v, w)^T$ and c the speed of sound. The variables of the field are decomposed by their initial value and the perturbed part,

$$\rho = \rho_0 + \rho_1, \quad P = P_0 + P_1, \quad \boldsymbol{u} = \boldsymbol{u}_0 + \boldsymbol{u}_1. \tag{2.8}$$

Considering a simple sheet geometry with only one interface between the stream an the CGM perpendicular to the x-axis, the initial condition have the following dependency,

$$\rho_0(x, y, z) = \rho_0(x), \quad P_0(x, y, z) = P_0, \quad \boldsymbol{u}_0 = \boldsymbol{u}_0(x). \tag{2.9}$$

The perturbed variables are expressed in the Fourier space as,

$$\forall f_1 \quad f_1(x, y, z, t) = g_1(x) e^{i(k_y y + k_z z - \omega t)}, \tag{2.10}$$

with k_y and k_z the wave vector components in the y and z directions, and ω the frequency. To express the evolution of the perturbed variables, equations are linearized by neglecting all second order terms leading to the new system,

$$\begin{cases} \dfrac{\partial \rho_1}{\partial t} + (\nabla \cdot \boldsymbol{u}_1)\, \rho_0 + (\boldsymbol{u}_1 \cdot \nabla)\, \rho_0 + (\boldsymbol{u}_0 \cdot \nabla)\, \rho_1 = 0, \\ \rho_0 \dfrac{\partial \boldsymbol{u}_1}{\partial t} + \rho_0\, (\boldsymbol{u}_0 \cdot \nabla)\, \boldsymbol{u}_1 + \rho_0\, (\boldsymbol{u}_1 \cdot \nabla)\, \boldsymbol{u}_0 + \nabla P_1 = 0, \\ \dfrac{\partial P_1}{\partial t} + (\boldsymbol{u}_0 \cdot \nabla)\, P_1 - c^2 \left[\dfrac{\partial \rho_1}{\partial t} + (\boldsymbol{u}_0 \cdot \nabla)\, \rho_1 + (\boldsymbol{u}_1 \cdot \nabla)\, \rho_0 \right] = 0, \end{cases} \tag{2.11}$$

and replacing by the Fourier decomposed variables, it is obtained,

$$\begin{cases} \rho_1 = -\dfrac{1}{k^2 \left(v_k - \frac{\omega}{k}\right)^2} \left[P_1'' - \dfrac{2v_k'}{v_k - \frac{\omega}{k}} P_1' - k^2 P_1 \right], \\ u_1 = \dfrac{i}{\rho_0 k \left(v_k - \frac{\omega}{k}\right)} P_1', \\ v_1 = -\dfrac{sin(\phi)}{\rho_0 \left(v_k - \frac{\omega}{k}\right)} P_1, \\ w_1 = -\dfrac{cos(\phi)}{\rho_0 k \left(v_k - \frac{\omega}{k}\right)} \left[\dfrac{v_k'}{k^2 cos^2(\phi) \left(v_k - \frac{\omega}{k}\right)} P_1' + P_1 \right], \end{cases} \tag{2.12}$$

leading for P_1 to the ordinary differential equation,

$$P_1'' - \left[\frac{2v_k'}{v_k - \frac{\omega}{k}} + \frac{\rho_0'}{\rho_0} \right] P_1' - k^2 \left[1 - \left(\frac{v_k - \frac{\omega}{k}}{c} \right)^2 \right] P_1 = 0, \tag{2.13}$$

which has the general solution as,

$$P_1 = Ae^{-rx} + Be^{rx}, \quad r = k\left[1 - \left(\frac{v_k - \frac{\omega}{k}}{c}\right)^2\right]^{1/2}. \tag{2.14}$$

As explain by (Mandelker et al., 2016), cold streams are already assumed to be stable in space, hence only the temporal stability is studied. Fig. 2.3 shows in the left panel the sheet geometry considered with only two-dimension for simplicity. To find the integration constants of Equation 2.14, we consider three main boundary conditions:

- $\lim_{x\to+\infty} P_{1b} = 0$,
- $\lim_{x\to-\infty} P_{1s} = 0$,
- Pressure continuous at the interface: $\lim_{x_+\to 0} P_{1b} = \lim_{x_-\to+\infty} P_{1s}$,

which leads to the solution,

$$P_1 = \begin{cases} Ae^{-r_b x} & x > 0 \\ Ae^{r_s x} & x < 0 \end{cases}. \tag{2.15}$$

In order to deduce the dispersion relation, it is consider the fact that the displacement from the background side is equal to the one from the stream side. This condition is called the Landau condition and is expressed as,

$$h_b = h_s, \tag{2.16}$$

with the displacement change rate equal to the velocity component normal to the interface,

$$u_1|_{x=0} = \frac{\partial h}{\partial t} + (\boldsymbol{u}\cdot\nabla)h = ik\left(u_0|_{x=0} - \frac{\omega}{k}\right)h. \tag{2.17}$$

Applying this equation to both side, we obtain the dispersion equation,

$$\frac{(v_{0,b}k - \omega)^2}{(v_{0,s}k - \omega)^2} = -\frac{\rho_{0,s}}{\rho_{0,b}}\frac{r_b}{r_s}. \tag{2.18}$$

To find values of ω solving the dispersion, we adopt the non-dimensional variables,

$$\varpi = \frac{\varpi_{\mathrm{d}}}{V} = \frac{\omega}{kV}, \quad \delta = \frac{\rho_s}{\rho_b}, \quad M_{b,s} = \frac{V}{c_{b,s}}, \tag{2.19}$$

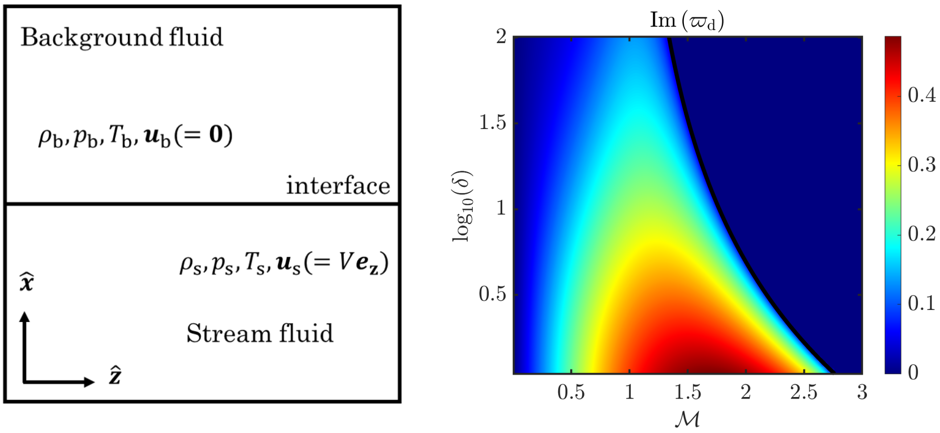

FIGURE 2.3: *Left panel:* Geometry sketch of the 2D sheet. *Right panel:* Color contours of the phase-velocity ϖ_d in the $(\mathcal{M}_b, \delta)$ space. The black line defines the limit for which the system is stable (toward surface modes).

with the phase-velocity $\varpi_d = \omega/k$. The dispersion relation hence becomes,

$$1 = -\frac{1}{\delta}\frac{\varpi^2}{(\varpi-1)^2}\left[\frac{1-(\varpi-1)^2\,\delta M_b^2}{1-\varpi^2 M_b^2}\right]^{1/2} = Z, \tag{2.20}$$

with Z the abbreviation for the right-hand side of the equation. Once Z put to the square, roots can be deduced of the polynomial,

$$\left[\delta(\varpi-1)^2 - \varpi^2\right]\left[\delta(\varpi-1)^2\left(M_b^2\varpi^2-1\right) - \varpi^2\right] = 0. \tag{2.21}$$

The roots from the quadratic equation correspond to the solution of $Z = -1$. Only the two complex roots of the quartic are solution of $Z = 1$ under $\mathcal{M}_{crit}$ while above two real roots are solution of $Z = 1$. Considering the two roots for $\mathcal{M}_b < \mathcal{M}_{crit}$, it consist of a complex number and its conjugate. The one with positive imaginary part refer to the growing mode while the other refer to the decaying mode. This two mode reveal the unstable nature of instabilities growth.

In the right panel of Fig. 2.3, the phase-velocity $\varpi_d = \omega/k$ for the growing mode is plotted in the $(\mathcal{M}_b, \delta)$ space. The higher is the phase-velocity and the faster the KHI will grow. For a fixed density ratio δ, ϖ as an inverted U-shape in function of $\mathcal{M}$ reaching a maximum KHI growth around $\mathcal{M} \sim 1 - 1.5$. Such behaviour is specific to compressible KHI. An increase of velocity induces an increase of shear leading to higher KHI growth. However, at some point, the dynamical pressure experienced by the surface instabilities will counteract their growth up to the point where the system becomes stable. In other word, for a sufficiently high $\mathcal{M}$, the surface mode of KHI can not grow. To provide an additional interpretation of those surface modes, we consider the case of a small sinusoidal perturbation of the interface with an

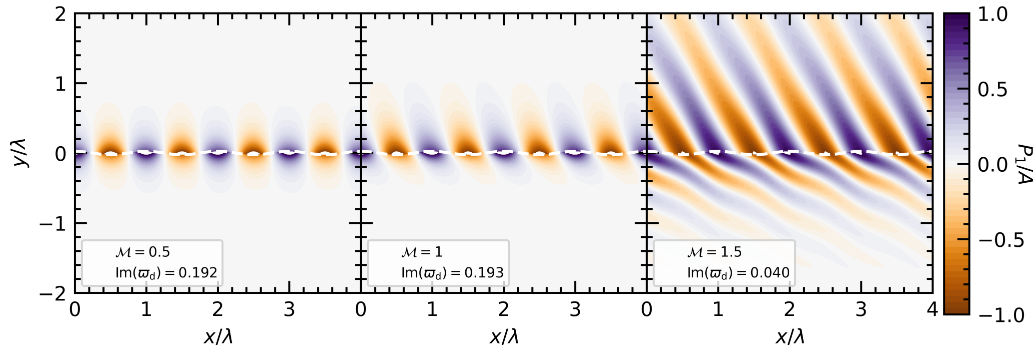

FIGURE 2.4: Pressure perturbation normalized by the initial amplitude in the limit of $t \to \infty$ for $\mathcal{M}_b = 0.5, 1, 1.5$ at a fixed $\delta = 30$. The initial interface perturbation is represented by the white dashed line. For each cases, the phase-velocity ϖ_d is shown.

amplitude $h = 0.025\lambda$, λ being the arbitrary wavelength of the perturbation. As a reminder, it is a temporal stability, hence we study the evolution limit of P_1 in equation 2.15) for $t \to \infty$, with,

$$\lim_{t \to \infty} P_1(x, z, t) = P_{g,1}(x) e^{ikz} = P_{1,lim}(x, z), \tag{2.22}$$

also remember that we consider a 2D geometry into the (x, z) plane. Hence at $x = 0$ we obtain,

$$P_{1,lim}(x = 0, z) = \frac{h}{\lambda} e^{ikz} \tag{2.23}$$

Using also the limit for $x \to \infty$, we obtain,

$$A(z) = \frac{h}{\lambda} e^{ikz}, \tag{2.24}$$

so the final expression of $P_{1,lim}(x, z)$ is,

$$P_{1,lim}(x, z) = \frac{h}{\lambda} e^{ikz} \times e^{rx}, \tag{2.25}$$

with $\forall x > 0, r = -r_b$ and $\forall x < 0, r = r_s$. The resulting pressure perturbation is shown in Fig. 2.4 for different $\mathcal{M}_b$ at a fixed $\delta = 30$. As the velocity increases, the pressure perturbations can penetrates deeper in both the dense and diffuse phases for $t \to \infty$ with a penetration angle more and more inclined toward the stream for increasing $\mathcal{M}$. However, in realistic cases, the KHI may reach a non-linear evolution before reaching this steady state, thus the importance of the phase-velocity ϖ_d (see equation 2.19). The cases $\mathcal{M} = 0.5, 1$ are both near the KHI growth peaks as seen in Fig. 2.3 and have similar value ϖ_d. Hence, in this case, a higher $\mathcal{M}$ means that the perturbation can penetrate deeper for a given timescale as both KHI have similar growth. This indicate that for surface modes, KHI can grow on longer timescale for $\mathcal{M} = 1$ compared to $\mathcal{M} = 0.5$. However, as shown in Fig. 2.3, the KHI surface modes stabilize for sufficiently high Mach number. This behaviour is particular to the KHI in the compressible regime. The higher the Mach number, the stronger the dynamical pressure a perturbation will experience, leading to the perturbation propagation more and more inclined toward the stream as shown in Fig. 2.4. At some point, the inclination is such that the surface mode cannot propagate anymore, leading to the stable region after a critical $\mathcal{M}$ shown in Fig. 2.3. To note, in the compressible regime, because of such inclination, a perturbation will shock at the interface of the stream leading to the propagation of a shock in the stream and the background. Such waves are called reflective or body modes and originate from this inclination angle.

2.3.2 KHI in the context of cold streams

The above results only holds for the slab geometry for purely hydrodynamics flow and surface modes. The addition of a physical process or the change of the geometry can change the stability conditions of the system, if any. As additional physics also drastically complicate the resolution of the system , one may use computational methods to either solve the system of the linear perturbation analysis (see the code PSECAS, Berlok & Pfrommer, 2019a), or directly performs hydrodynamics simulations with the additional physics.

We hereby presents from literature the impacts of hydrodynamics and additional physics considering a cold stream geometry idealized as a cold cylinder inside a hot CGM background.

Purely hydrodynamics : From linear analysis, Mandelker et al. (2016) determined that the surface modes (described in Sec. 2.3.1) were dominant for the subsonic regime but for supersonic regime, body modes or reflective modes can also make the system unstable. Body modes are the results of the perturbation "shocking" at the interface of the stream and the CGM, creating a sound or shock wave on each side of the interface. Hence, the this wave inside the stream will propagate until reaching the other edge of the stream where it reflects back, thus the name "reflecting" mode. While the unstable surface modes will cause the stream to disrupt due to the growing eddies in the interface, the unstable body modes leads a fragmentation of the stream into smaller over dense filaments which then eventually leads to the stream disruption. From HD simulations, Padnos et al. (2018) and Mandelker et al. (2019) investigates the stream evolution in 2D and 3D, respectively. They concluded that surface modes have the highest growth rate and were the dominant mode that could alter the cold stream evolution for 3D simulations. To mention, Vossberg et al. (2019) studied from 2D HD simulations the over-dense stream regions.

HD and Self-gravity : Self-gravity can lead to the collapse of the stream when its line-density is above a threshold for which an isothermal stream cannot reach the hydrostatic equilibrium (Ostriker, 1964). Under this threshold, Aung et al. (2019), from hydrodynamic simulations without radiative cooling, found that KHI can still trigger the fragmentation of the stream due to Gravitational instability under a second line-density threshold. The addition of cooling and self-shielding can enhance the gravitational instability but magnetic field and thermal conduction are expected to inhibit them.

Magnetic field (purely MHD) : With 2D and 3D magnetohydrodynamic (MHD) simulations, Berlok & Pfrommer (2019b) studied the impact of the magnetic field parallel to the stream, and found that it can help the stream to stabilize against KHI if the field strength is strong enough ($B \gtrsim 0.3$–$0.8\,\mu$G). Indeed, for sufficiently strong magnetic field perpendicular to the KHI propagation, a tension force appears and acts against the KHI growth.

HD and Radiative cooling : While all latter works mainly addressed the cold stream evolution, Mandelker et al. (2020a) provided valuable insights into the emission signature of cold streams by incorporating radiative cooling into HD simulations. They demonstrated that for HD simulation, radiative cooling leads to broadly two stream regime: a Disrupting Stream regime, where the KHI growth is too fast compared to the cooling time of gas; a Condensing Stream regime, where as soon hot CGM gas mixes with the stream gas, it cools efficiently down to the stream temperature, in other word condensate. Mandelker et al. (2020a) showed that the cooling emission from this condensation scales with the cooling time as $\propto t_{\rm cool}^{-1/4}$.

2.3.3 The mixing layer

The initial growth of KHI leads to the mixing of both the stream and CGM gas. In the case were radiative losses from the mixed phase are negligible, the development of the mixing layer does not play an active role in the dynamics of the system. However, often, the mixed phase reach temperature were the radiative cooling peaks. From KHI in the solar corona (Hillier & Arregui, 2019, Hillier et al., 2020), to cold clouds Gronke & Oh (2018, 2020) embedded inside galactic winds or cold streams in the

CGM (Mandelker et al., 2020a), the development of a radiative mixing layer can lead to significant emission and potentially alter the dynamics of the system.

We hereby summarise previous studies on the mixing layer relevant to our work. Begelman (1990) and Slavin et al. (1993) first described the physical properties of the mixing of two gas from a shear interface in the case of the interstellar medium. In particular, considering the mass accretion rate $\dot{m}_{\rm c}$ and $\dot{m}_{\rm h}$ of the cold and the hot phase, they defined the temperature of the mixed phase as,

$$T_{\rm mix} = \frac{\dot{m}_{\rm c} T_{\rm c} + \dot{m}_{\rm h} T_{\rm h}}{\dot{m}_{\rm c} + \dot{m}_{\rm h}} \sim (T_{\rm c} T_{\rm h})^{\frac{1}{2}}\,, \tag{2.26}$$

assuming ideal mass accretion rate as $\dot{m}_{\rm h-c} \sim \rho_{\rm h-c} v_{\rm t,h-c}$ for both phases with $v_{\rm t,h-c}$ being the turbulent velocity for the hot and the cold phases, linked by equating their kinetic energies, $\rho_{\rm c} v_{\rm t,c}^2 = \rho_{\rm h} v_{\rm t,h}^2$[1]. This was later followed by detailed studies from simulations on interface geometry (e.g. Kwak & Shelton, 2010, Ji et al., 2019, Fielding et al., 2020, Tan et al., 2021, Yang & Ji, 2023), on the cold gas entrained in hot wind (Gronke & Oh, 2018, 2020), and on cold streams (Mandelker et al., 2020a).

In the case where the radiative cooling is strong enough to condense gas from the hot phase, the mixing velocity or the inflow velocity of CGM gas into the mixing layer scales as (Gronke & Oh, 2020, Mandelker et al., 2020a, Fielding et al., 2020, Tan et al., 2021)

$$v_{\rm in} \propto t_{\rm cool}^{-1/4}. \tag{2.27}$$

The inflow of the hot gas in the mixing layer occurs at a steady rate. Once at the temperature $T_{\rm mix}$, the gas mixture cools efficiently, leading to a steady cooling emission which also scales as $L_{\rm net} \propto t_{\rm cool}^{-1/4}$. From $v_{\rm in}$, one can also recover the mass evolution of the cold stream for sufficiently strong cooling due to the condensation of CGM gas,

$$\dot{M}_{\rm s} \sim \rho_{\rm cgm} v_{\rm in} S, \tag{2.28}$$

where S is the surface between the stream and the CGM. We note that a different scaling is found by Ji et al. (2019) with $v_{\rm in} \propto t_{\rm cool}^{-1/2}$, similarly to the weak cooling case in Tan et al. (2021). While we discuss the scaling in our simulations, higher resolution simulations targeting specifically the mixing layer (Fielding et al., 2020, Tan et al., 2021) might be needed to investigate the origin of the scaling properly in the presence of magnetic field and thermal conduction. Such work is beyond the scope of this paper.

[1] The turbulent kinetic energy equality is not explicitly mentioned by Begelman (1990) but is implicitly contained in his definition of $v_{\rm t,c}$.

The initial evolution of the mixing layer is also important as it can define the strength of the initial KHI growth. The initial growth of the mixing layer before its steady evolution due to cooling can be described by the shearing time (Mandelker et al., 2019, 2020a),

$$t_{\mathrm{sh}} = \frac{R_{\mathrm{s}}}{\alpha v_{\mathrm{s},0}}, \tag{2.29}$$

with the dimensionless growth rate defined by the empirical fitting value $\alpha \sim 0.042 + 0.168 \exp\left(-3\mathcal{M}_{\mathrm{tot}}^2\right)$ (Dimotakis, 1991), where the total Mach number is defined with the sound speed of both phases $\mathcal{M}_{\mathrm{tot}} = V_{\mathrm{s}} / \left(c_{\mathrm{s}} + c_{\mathrm{cgm}}\right)$.

2.4 Thermal conduction

2.4.1 Introduction to non-linear conductivity

In the assumption of fully ionized gas, the thermal conduction is dominated by the transport of energy by electrons, with, in the presence of magnetic fields, the electrons following the fields lines. The conduction coefficient in such case becomes temperature dependent and is defined by the Spitzer coefficient (Spitzer, 1962)

$$\kappa = \kappa_0 T^{2.5} \tag{2.30}$$

with $\kappa_0 = 1.84 \times 10^{-5} / \log\Omega$, and $\log\Omega \sim 29.7 + \log\left[T/\left(10^6\sqrt{n_{\mathrm{e}}}\right)\right]$ being the Coulomb logarithm. In such case, the conductivity coefficient is temperature dependent, leading to a diffusion mechanism very different than in the case of a constant coefficient.

For illustration, let's assume a one-dimension domain defined by $x \in [x_1, x_2]$ with for boundary condition a wall with fixed temperature $T(x_1) = T_1$ and $T(x_2) = T_2$. Considering that only the temperature changes, the heat conduction equation, which is a parabolic Partial Differential Equation (PDE), takes the form of,

$$\frac{\partial T}{\partial t} = \frac{\partial}{\partial x}\left(\kappa(T)\frac{\partial T}{\partial x}\right), \tag{2.31}$$

where in our case we consider Spitzer conductivity defined by equation 2.30 Transient trivial solutions of this PDE cannot be obtained analytically as in the linear case. However, we can derive the steady state solution out of it. This steady-state solution represents the asymptotic solution that is reached after a typical timescale.

We then consider the steady-state solution of equation (2.31),

$$\frac{\partial}{\partial x}\left(\kappa(T)\frac{\partial T}{\partial x}\right) = 0. \tag{2.32}$$

After a first integration and considering one of the boundary conditions, it is obtained,

$$\kappa_0 T^{2.5}\mathrm{d}T = C_1\mathrm{d}x,$$

with $C1$ the integration constant. Then, we can solve the integral,

$$\int_{T_1}^{T} T'^{2.5}\mathrm{d}T' = \int_{x_1}^{x} C_1\mathrm{d}x',$$

which has for solution,

$$\Leftrightarrow T^{3.5} = 3.5C_1(x-x_1) + T_1^{3.5}.$$

Considering the boundary condition at $x = x_2$ with $T(x = x_2) = T_2$ to find C_1 yields to,

$$\frac{1}{3.5}T_2^{3.5} - \frac{1}{3.5}T_1^{3.5} = C_1(x_2 - x_1),$$

$$\Leftrightarrow C_1 = \frac{1}{3.5(x_2-x_1)}\left(T_2^{3.5} - T_1^{3.5}\right),$$

and inserting C_1 into the analytical solution we finally have,

$$T(x) = \left[\frac{x-x_1}{x_2-x_1}\left(T_2^{3.5} - T_1^{3.5}\right) + T_1^{3.5}\right]^{2/7}. \tag{2.33}$$

Following the same method for a constant conductivity coefficient $\kappa^{\mathrm{lin}} = \kappa_0$ leads to the solution,

$$T^{\mathrm{lin}}(x) = \frac{x-x_1}{x_2-x_1}\left(T_2 - T_1\right) + T_1. \tag{2.34}$$

To note, none of the solutions are dependent of κ_0 as this parameter only define the speed at which the system reaches the steady solution without affecting the solution itself. The solutions of equation 2.33 and equation 2.4.1 are shown in Fig. 2.5 for the space domain $(x_1, x_2) = (0, 1)$ and boundary conditions $(T_1, T_2) = (0.1, 1)$. The length and temperature are here in arbitrary units. As shown in the figure, the solution for κ^{lin} exhibits a simple straight line, which in other words leads to a flat temperature power distribution function (PDF). In the case of non-linear conduction, the temperature profile changes drastically leading to a diffusion front with a rather high temperature jump. Hence, considering the temperature PDF for an unsteady case would lead to a rather bimodal trend where the gas is either hot or cold, with very little gas at intermediate temperature.

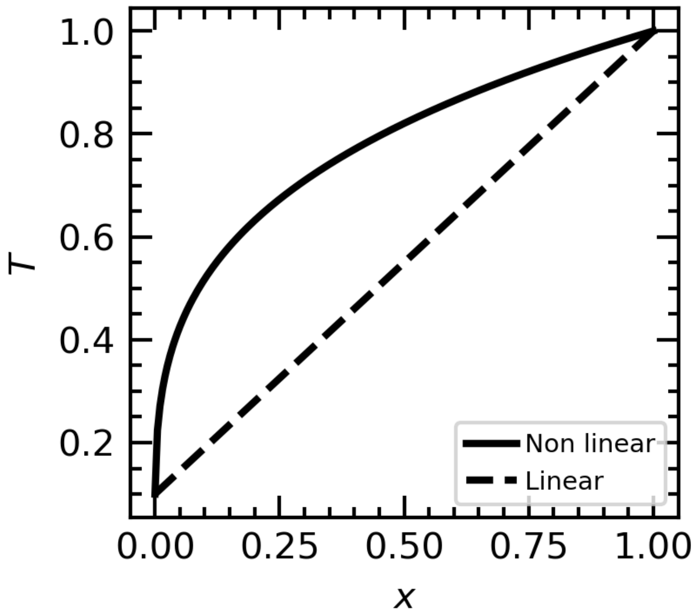

FIGURE 2.5: Steady state solution of the one-dimension heat PDE for both non-linear and linear conductivity.

This specificity of the Spitzer conductivity is crucial in the case of cold streams as it will counteract the development of the mixing layer described in Sec. 2.3.

2.4.2 Anisotropic thermal conduction efficiency

The thermal conduction in plasma is known to be dominated by electrons transporting the dominant part of the conduction flux along magnetic field lines. However, some uncertainties remain on the efficiency of the descriptions of the ideal case described by Spitzer (1962) as multiple phenomena can alter the flux transport. The basis of the conduction hold from two crucial length scale which are the temperature scale defined as,

$$L_{\mathrm{T}} = \frac{T}{\nabla T}, \tag{2.35}$$

and the electron mean free path,

$$\lambda_{\mathrm{mfp}} = t_{\mathrm{e}} \left(\frac{3 k_{\mathrm{b}} T}{m_{\mathrm{e}}} \right)^{1/2}, \tag{2.36}$$

where m_{e} is the electron mass, and t_{e} the electron-electron equipartition time defined by,

$$t_{\mathrm{e}} = \frac{3\sqrt{m_{\mathrm{e}}}\,(k_{\mathrm{b}} T)^{3/2}}{4\sqrt{\pi} n_{\mathrm{e}} e^4 \log \Omega}, \tag{2.37}$$

with n_{e} the electron number density and e the electron charge.

From early plasma experiments, the thermal conduction flux can exhibit a saturation of its efficiency down to $\sim 10\%$ its ideal value when $L_{\mathrm{T}} \sim 30\lambda_{\mathrm{mfp}}$ (Gray & Kilkenny, 1980, Matte & Virmont, 1982). Such saturation is also supported in the observation of solar-wind (Bale et al., 2013). Further mechanisms can also reduce the efficiency of thermal conduction such as in the case of weakly magnetized plasmas with small temperature gradient (Komarov et al., 2018), or in the case of the twisting of the magnetic field lines from turbulence (e.g. Meinecke et al., 2022).

The exact value of the efficiency decrease of thermal conduction is not well constrained and can vary depending on the considered plasma. Furthermore, the commonly used saturation formulation of the thermal flux from Cowie & Mckee (1977) transform the parabolic PDE formulation of the energy equation into a hyperbolic one, which can lead to the creation of unphysical thermal shock. The effect of such saturation has been recently assessed in the case of cold clouds inside the CGM (Sander & Hensler, 2023), showing that saturated thermal flux indeed decreases the efficiency and the impact of the thermal conduction, but considering a transition condition between the classical and the saturated flux for $L_{\mathrm{T}} \sim 500\lambda_{\mathrm{mfp}}$, which seems relatively high. Considering these uncertainties, we do not consider the saturated flux in this work.

About the decreases in efficiency of the thermal conduction due to turbulence, as seen the Section 4.2.3, we consider that this effect is explicitly solved in our simulations.

2.4.3 Thermal conduction timescales

The thermal conduction time-scale for the stream is defined as

$$\tau_{\mathrm{s}} \equiv \frac{\rho_{\mathrm{mix}} R_{\mathrm{s}}^2}{\kappa_0 T_{\mathrm{mix}}^{2.5}}, \tag{2.38}$$

where the conductivity is defined based on the mixing phase, as the temperature of the diffusion front is approximately the same value.

This diffusion time, along with the cooling time, determines whether the stream will grow in mass or diffuse. However, we are also interested in the impact of thermal conduction on the mixing between the stream and the CGM due to the growth of the KHI. Therefore, we also define the diffusion time for a small perturbation or clump of size $0.1R_{\mathrm{s}}$, as

$$\tau_{\mathrm{p}} \equiv \frac{\rho_{\mathrm{mix}} \left(0.1 R_{\mathrm{s}}\right)^2}{\kappa_0 T_{\mathrm{mix}}^{2.5}}, \tag{2.39}$$

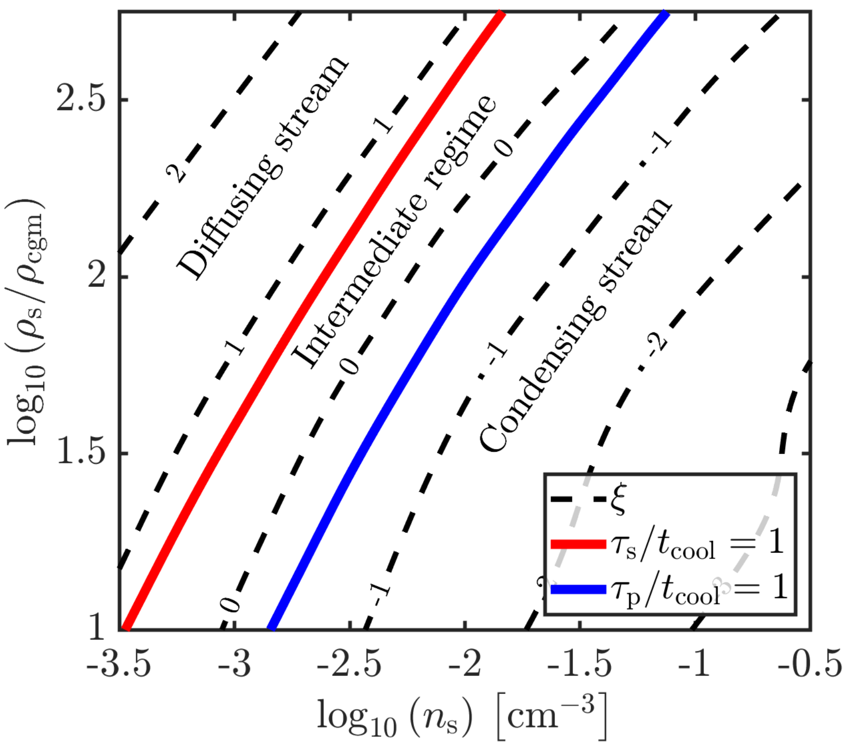

FIGURE 2.6: Contour lines of the ratio $\xi = t_{cool}/t_{sh}$ (dashed black lines) in log-scale as functions of stream number density, and density ratios of the stream over CGM. Each contour lines displays their respective value of $\log_{10}(\xi)$. The cold stream is considered to be at the virial radius of a $M_h = 10^{12}M_\odot$ halo at $z = 2$, with $R_s = 1$ kpc, metallicity $Z_s/Z_\odot = 10^{-1.5}$, Mach number $\mathcal{M}_{cgm} = 1$, and CGM metallicity $Z_{cgm}/Z_\odot = 10^{-1}$. The contours for which the diffusion times τ_s and τ_p equate t_{cool} are depicted by the blue and red curves, respectively. Those limits define three different regimes for the cold stream evolution in the presence of TC: *diffusing stream*, *intermediate*, and *condensing stream* regimes.

with the subscript p standing for perturbation and where the diffusivity is also defined from the mixing phase.

2.5 Timescale comparison

From the physical processes presented above, we can assume the evolution of the stream by considering the different time-scales t_{sh}, t_{cool}, τ_s, and τ_p. An important parameter to describe the stream evolution is the ratio of the cooling time over the shearing time,

$$\xi = \frac{t_{cool}}{t_{sh}}. \tag{2.40}$$

Figure 2.6 plots contours of the ratio ξ on the plane of stream density n_s and density ratio $\delta = \rho_s/\rho_{cgm}$. In the hydrodynamic case, the stream evolution can be defined by ξ as follows:

- Disrupting stream regime: $\xi > 1$,
- Condensing Stream regime: $\xi < 1$.

In the presence of thermal conduction, the above categorization is modified by the ratios $\tau_{\rm s}/t_{\rm cool}$ and $\tau_{\rm p}/t_{\rm cool}$, both shown in the plot. Those two ratios are an equivalent formulation to the Field length, which defines the limit at which a structure either diffuses or condenses. Hence, $\tau_{\rm s}/t_{\rm cool} = 1$ and $\tau_{\rm p}/t_{\rm cool} = 1$ mark the limit for which the stream or a cold clump, respectively, either diffuse or survive. Including thermal conduction with our cold stream parameters, we end up with three different regimes of interest:

- **Diffusing Stream regime:** $\tau_{\rm p} < \tau_{\rm s} < t_{\rm sh} < t_{\rm cool}$
  In this case, the diffusion from thermal conduction (TC) is too rapid and overcomes all other processes. The stream diffuses faster than it can condense gas from itself or the CGM. This regime is analogous to a Field length larger than the stream radius. In practice for our model, this regime is obtained with the condition $\xi \gtrsim 8$.
- **Intermediate regime:** $\tau_{\rm p} < t_{\rm sh} < t_{\rm cool} < \tau_{\rm s}$
  In this regime, the cooling time and the shearing time are about the same magnitude and are bigger than the diffusion time $\tau_{\rm p}$. Hence, the diffusion of perturbations or small clumps smaller than $0.1R_{\rm s}$, happens faster than their growth, potentially shutting off the mixing and the subsequent condensation of CGM gas. In this regime, the mixing layer should diffuse and the stream remains at a constant mass while possibly fragmenting due to long-wavelength KHI modes. From our parameters, this regime can be roughly defined by $0.3 < \xi < 8$.
- **Condensing Stream regime:** $t_{\rm cool} < t_{\rm sh} < \tau_{\rm p} < \tau_{\rm s}$
  In this regime, radiative cooling occurs faster than both diffusion and KHI growth. The gas in the mixing layer cools efficiently, hence condensing on to the stream. We found that this regime is satisfied for $\xi \lesssim 0.3$.

The regime map of Fig. 2.6 is also dependent on the assumed stream radius $R_{\rm s}$ and the metallicities of CGM and stream. For a bigger or smaller radius, the Condensing regime region in the $n_{\rm s} - \delta$ map would widen or reduce, respectively. Similarly, increasing or decreasing the metalicities would widen or reduce the Condensing regime region, respectively.

Chapter 3

Numerical set-up

3.1 Governing equations and computational method

We solve the following normalized MHD equations in conservative form using the finite volume mesh code Athena++ (Stone et al., 2020), in which we implemented anisotropic thermal conduction and radiative cooling:

$$\begin{cases} \dfrac{\partial \rho}{\partial t} + \nabla \cdot (\rho \mathbf{u}) = 0\,, \\[2ex] \dfrac{\partial (\rho \mathbf{u})}{\partial t} + \nabla \cdot [\rho (\mathbf{u} \otimes \mathbf{u}) - (\mathbf{B} \otimes \mathbf{B}) + p_{\mathrm{T}} \mathbb{I}] = 0\,, \\[2ex] \dfrac{\partial \mathbf{B}}{\partial t} - \nabla \times (\mathbf{u} \times \mathbf{B}) = 0\,, \\[2ex] \dfrac{\partial e}{\partial t} + \nabla \cdot [(e + p_{\mathrm{T}}) \mathbf{u} - \mathbf{B} (\mathbf{B} \cdot \mathbf{u}) + \mathbf{Q}] = \rho^2 (\mathcal{H} - \Lambda)\ , \end{cases} \tag{3.1}$$

where $\mathbb{I}$ is the identity matrix. The total pressure p_{T} is defined as

$$p_{\mathrm{T}} = p + \frac{B^2}{2}. \tag{3.2}$$

Notations ρ, $\mathbf{u}$, $\mathbf{B}$, e, p, stand for the mass density, velocity vector, magnetic vector, total energy density, and pressure, respectively. The total energy density is defined as

$$e = \frac{p}{\gamma - 1} + \frac{B^2}{2} + \rho \frac{u^2}{2}. \tag{3.3}$$

The anisotropic thermal conduction term $\mathbf{Q}$ is defined as

$$\mathbf{Q} = -\kappa \mathbf{b} (\mathbf{b} \cdot \nabla T), \tag{3.4}$$

TABLE 3.1: Normalisation Units.

Quantity	Normalised unit	Values
Length	$L_0 = R_\mathrm{s}$	1 kpc
Velocity	$c_0 = c_\mathrm{s} = (\gamma T_0 k_\mathrm{b}/m)^{1/2}$	18–27 $\mathrm{km\,s^{-1}}$
Time	$t_0 = L_0/c_0$	37–56 Myr
Temperature	$T_0 = T_\mathrm{s}$	$(1.3\text{–}3.1) \times 10^4$ K
Density	$\rho_{\mathrm{s},0} = n_\mathrm{s} m_0$	10^{-27}–10^{-25} $\mathrm{g\,cm^{-3}}$
Pressure	$P_0 = \rho_0 k_\mathrm{b} T_0/m_0$	10^{-14}–10^{-13} $\mathrm{dyn\,cm^{-2}}$
Magnetic field	$B_0 = (8\pi P_0/\beta)^{1/2}$	$(1\text{–}6, 8) \times 10^{-3}$ μG

with $\mathbf{b} = \mathbf{B}/B$ the magnetic field unit vector, and $\kappa = \kappa_0 T^{2.5}$ the Spitzer thermal conduction coefficient (Spitzer, 1962). The radiative cooling terms $\mathcal{H} - \Lambda$ are interpolated from tables of our model described in Sec. 2.2.2. We summarise the normalisation units in Table 3.1.

We also trace the mass fraction of gas in the initial stream and CGM gas using a passive scalar transport equation, defined as

$$\frac{\partial\,(\rho\mu_\mathrm{s})}{\partial t} + \nabla \cdot (\rho\mathbf{u}\mu_\mathrm{s}) = 0, \tag{3.5}$$

where $\mu_\mathrm{s} = \rho_\mathrm{s}/\rho$ is, in other words, the mass fraction of the gas at the initial stream metallicity. In practice, we use this scalar to compute the metallicity of the gas when computing the cooling rate.

The conservative MHD formulation is solved using the HLLD Riemann solver from Miyoshi & Kusano (2005) using the spatial PLM reconstruction which is second-order accurate. The divergence-free constraint of the magnetic field is ensured with the Constrained-Transport-scheme introduced in Gardiner & Stone (2005, 2008). For time integration, the second-order Runge-Kutta scheme is used for simulations without thermal conduction. In the case of thermal conduction, the conduction time-step is proportional to Δx^2, leading to high computational costs. To reduce the computational cost, the super-time-stepping (STS) Runge-Kutta-Legendre second-order solver from Meyer et al. (2014) is used to solve the thermal conduction equation. We apply the limiting scheme developed by Sharma & Hammett (2007) which avoids overestimation of the conduction flux when this one is anisotropic.

3.2 Initial conditions

Our initial conditions are similar to those used in the simulations from Mandelker et al. (2020a) and are summarised here. Fig. 3.1 shows the initial setup.

TABLE 3.2: List of simulation parameters. From left to right, the physics ID stands for hydrodynamic (HD), magnetohydrodynamic (MHD), and MHD with anisotropic thermal conduction (MHD+TC); the density ratio δ; the stream number density n_{s}; the magnetic field angle α, such that $\alpha = 0°$ is a field parallel to the stream; the magnetic field initial strength, the stream Mach number with respect to the CGM sound speed, $\mathcal{M} = \mathcal{M}_{\mathrm{cgm}}$; the CGM sound speed; the ratio of the virial crossing time and t_0 for $\mathcal{M} = 1$; the stream temperature; the ratio of cooling time over shearing time ξ, and the temperature at which the cooling is maximum. For each row, simulations are performed for the three Mach numbers $\mathcal{M} = (0.5, 1, 2)$ or less if specified. The total number of simulations is about 120.

Physics ID	δ $\rho_{\mathrm{s}}/\rho_{\mathrm{cgm}}$	n_{s} [cm^{-3}]	**B**-field angle α	B_0 $10^{-3}\,\mu\mathrm{G}$	$\mathcal{M}$ [-]	c_{cgm} [$\mathrm{km\,s^{-1}}$]	t_{vir}/t_0 ($\mathcal{M}=1$) [-]	T_{s} [10^4 K]	ξ [-]	$T_{\mathrm{cool,max}}$ [10^4 K]
HD	30	10^{-3}	-	-	$(0.5, 1, 2)$	146	18.26	3.11	2.9	4.46
HD	30	10^{-2}	-	-	$(0.5, 1, 2)$	116	18.26	1.96	0.6×10^{-1}	2.99
HD	30	10^{-1}	-	-	$(0.5, 1, 2)$	96	18.26	1.33	2.5×10^{-3}	2.27
HD	100	10^{-3}	-	-	$(0.5, 1, 2)$	267	10.00	3.11	2.1×10^{1}	4.79
HD	100	10^{-2}	-	-	$(0.5, 1, 2)$	212	10.00	1.96	0.3	3.02
HD	100	10^{-1}	-	-	$(0.5, 1, 2)$	175	10.00	1.33	1.2×10^{-2}	2.29
MHD	30	10^{-3}	90°	1.0	$(0.5, 1, 2)$	146	18.26	3.11	2.9	4.46
MHD	30	10^{-3}	45°	1.0	$(0.5, 1, 2)$	146	18.26	3.11	2.9	4.46
MHD	30	10^{-3}	0°	1.0	$(0.5, 1, 2)$	146	18.26	3.11	2.9	4.46
MHD	30	10^{-2}	90°	2.6	$(0.5, 1, 2)$	116	18.26	1.96	0.6×10^{-1}	2.99
MHD	30	10^{-2}	45°	2.6	$(0.5, 1, 2)$	116	18.26	1.96	0.6×10^{-1}	2.99
MHD	30	10^{-2}	0°	2.6	$(0.5, 1, 2)$	116	18.26	1.96	0.6×10^{-1}	2.99
MHD	30	10^{-1}	90°	6.8	$(0.5, 1, 2)$	96	18.26	1.33	2.5×10^{-3}	2.27
MHD	30	10^{-1}	45°	6.8	$(0.5, 1, 2)$	96	18.26	1.33	2.5×10^{-3}	2.27
MHD	30	10^{-1}	0°	6.8	$(0.5, 1, 2)$	96	18.26	1.33	2.5×10^{-3}	2.27
MHD	100	10^{-3}	90°	1.0	$(0.5, 1, 2)$	267	10.00	3.11	2.1×10^{1}	4.79
MHD	100	10^{-3}	45°	1.0	$(0.5, 1, 2)$	267	10.00	3.11	2.1×10^{1}	4.79
MHD	100	10^{-3}	0°	1.0	$(0.5, 1, 2)$	267	10.00	3.11	2.1×10^{1}	4.79
MHD	100	10^{-2}	90°	2.6	$(0.5, 1, 2)$	212	10.00	1.96	0.3	3.02
MHD	100	10^{-2}	45°	2.6	$(0.5, 1, 2)$	212	10.00	1.96	0.3	3.02
MHD	100	10^{-2}	0°	2.6	$(0.5, 1, 2)$	212	10.00	1.96	0.3	3.02
MHD	100	10^{-1}	90°	6.8	$(0.5, 1, 2)$	175	10.00	1.33	1.2×10^{-2}	2.29
MHD	100	10^{-1}	45°	6.8	$(0.5, 1, 2)$	175	10.00	1.33	1.2×10^{-2}	2.29
MHD	100	10^{-1}	0°	6.8	$(0.5, 1, 2)$	175	10.00	1.33	1.2×10^{-2}	2.29
MHD+TC	30	10^{-3}	90°	1.0	$(0.5, 1, 2)$	146	18.26	3.11	2.9	4.46
MHD+TC	30	10^{-3}	45°	1.0	$(0.5, 1, 2)$	146	18.26	3.11	2.9	4.46
MHD+TC	30	10^{-3}	0°	1.0	$(0.5, 1, 2)$	146	18.26	3.11	2.9	4.46
MHD+TC	30	10^{-2}	90°	2.6	$(0.5, 1, 2)$	116	18.26	1.96	0.6×10^{-1}	2.99
MHD+TC	30	10^{-2}	45°	2.6	$(0.5, 1, 2)$	116	18.26	1.96	0.6×10^{-1}	2.99
MHD+TC	30	10^{-2}	0°	2.6	$(0.5, 1, 2)$	116	18.26	1.96	0.6×10^{-1}	2.99
MHD+TC	30	10^{-1}	90°	6.8	$(0.5, 1, 2)$	96	18.26	1.33	2.5×10^{-3}	2.27
MHD+TC	30	10^{-1}	45°	6.8	$(0.5, 1, 2)$	96	18.26	1.33	2.5×10^{-3}	2.27
MHD+TC	30	10^{-1}	0°	6.8	$(0.5, 1, 2)$	96	18.26	1.33	2.5×10^{-3}	2.27
MHD+TC	100	10^{-3}	90°	1.0	$(0.5, 1, 2)$	267	10.00	3.11	2.1×10^{1}	4.79
MHD+TC	100	10^{-3}	45°	1.0	$(0.5, 1)$	267	10.00	3.11	1.6×10^{1}	4.79
MHD+TC	100	10^{-2}	90°	2.6	$(0.5, 1, 2)$	212	10.00	1.96	0.3	3.02
MHD+TC	100	10^{-2}	45°	2.6	$(0.5, 1, 2)$	212	10.00	1.96	0.3	3.02
MHD+TC	100	10^{-2}	0°	2.6	$(0.5, 1, 2)$	212	10.00	1.96	0.3	3.02
MHD+TC	100	10^{-1}	90°	6.8	$(0.5, 1, 2)$	175	10.00	1.33	1.2×10^{-2}	2.29
MHD+TC	100	10^{-1}	45°	6.8	$(0.5, 1, 2)$	175	10.00	1.33	1.2×10^{-2}	2.29
MHD+TC	100	10^{-1}	0°	6.8	$(0.5, 1, 2)$	175	10.00	1.33	1.2×10^{-2}	2.29

The stream is initialized at the centre of a two-dimensional rectangular domain of size $64R_{\mathrm{s}} \times 32R_{\mathrm{s}}$, the stream axis being the y-axis and with $R_{\mathrm{s}} = 1\,\mathrm{kpc}$. Boundary conditions are set as periodic in the stream parallel direction and as fixed CGM fluid values along the perpendicular directions. Compared to previous works (Mandelker et al., 2019, Berlok & Pfrommer, 2019b, Mandelker et al., 2020a), we extended the domain transversal to the stream by a factor of two to avoid boundary effects on the stream due to thermal conduction and the fixed boundary conditions. About the resolution, we use static mesh refinement with the highest resolution of $\Delta x = \Delta y = R_{\mathrm{s}}/64$ defined in the near-stream region ($< 2R_{\mathrm{s}}$). The grid size is then doubled up every $2R_{\mathrm{s}}$ along the x-axis up to a maximum cell size of R_{s}.

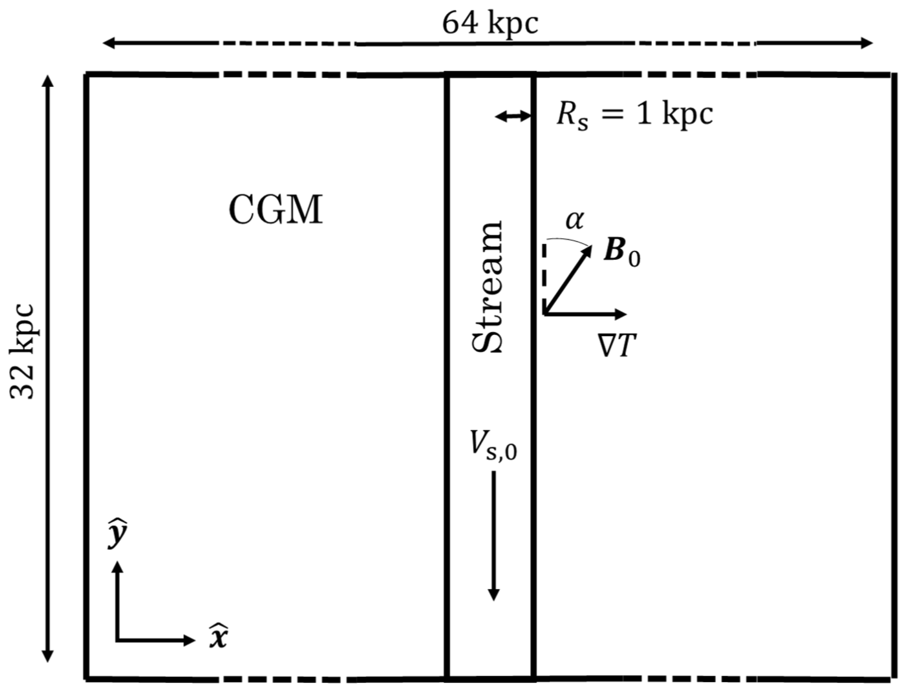

FIGURE 3.1: Schematic of the initial conditions of our simulations. The stream region is cold and dense, while the CGM background is defined as hot and diffuse. The initial angle of the magnetic field α is defined towards the unit vector $\hat{y}$. The stream vector velocity is defined towards the $-\hat{y}$, in the downward direction. The resulting direction of the initial temperature gradient is along the x-axis, perpendicular to stream.

The stream is defined in the density field by

$$\frac{\rho(x)}{\rho_{\rm s,0}} = \frac{\rho_{\rm cgm}}{\rho_{\rm s,0}} + \frac{1}{2}\left(1 - \frac{\rho_{\rm cgm}}{\rho_{\rm s,0}}\right)\left(1 - \tanh\left(\frac{|x| - R_{\rm s}}{h}\right)\right), \tag{3.6}$$

where h determines the smoothness of the transition[1] between the stream and the CGM gas, with $h = R_{\rm s}/32$. In a similar way, the stream velocity is defined as

$$v(x) = -\frac{v_{s,0}}{2}\left(1.0 - \tanh\left(\frac{|x| - R_{\rm s}}{h}\right)\right), \tag{3.7}$$

where $v_{s,0} = \mathcal{M}c_{\rm cgm}$, and $\mathcal{M}$ is the Mach number of the stream based on the sound speed in the CGM. We considered values of $\mathcal{M} \in [0.5, 1.0, 2.0]$. To initialize the KHI, the transverse velocity field is initially seeded by perturbations,

$$u\,(x, y) = u_0 \sum_{j}^{N_{\rm k}} \left[\cos\left(k_j y\right)\right] \exp\left(-\frac{(|x| - R_{\rm s})^2}{8h^2}\right), \tag{3.8}$$

[1]As discussed in Mandelker et al. (2020a), this smoothness layer is not needed for HD simulations with cooling as the layer would shrink by condensation. However, in the presence of magnetic field and thermal conduction, we found that in the case of the Stream Diffusion regime, a step transition can lead to the divergence of the simulation. We hence kept the relatively sharp but non-zero smoothing layer from Mandelker et al. (2019).

where N_k is the total number of perturbations defined by $k_j = 2\pi/\lambda_j$ with $\lambda_j \in [0.5R_\mathrm{s}, 16R_\mathrm{s}]$, and $u_0 = 0.01c_\mathrm{s}$ is the amplitude[2] of the perturbed modes.

The magnetic field is defined by an initial angle α,

$$\mathbf{B} = (B_0 \sin\alpha, B_0 \cos\alpha, 0) \tag{3.9}$$

such as $\alpha = 0°$ corresponds to the case where the magnetic field is aligned to the stream (and perpendicular to the temperature gradient), and $\alpha = 90°$ corresponds to the case where the magnetic field is transverse to the stream (and aligned with the temperature gradient). As the magnetic field is constant over the entire domain, hydrostatic equilibrium gives us a constant pressure P_0 both in the CGM and in the stream.

Table 3.2 lists all simulations and their parameters. For each row of parameters, unless specified, three simulations with $\mathcal{M} = 0.5, 1$ and 2 are run, leading to a total of about 120 simulations. The resulting stream velocities span over 48–534 kms^{-1} in good agreement with observations. Simulations are run for a total time of $t_\mathrm{end} = 22t_0 \sim 0.8$–$1.2\,\mathrm{Gyr}$.

[2] To check the impact of the chosen value of u_0, we ran MHD simulations (with $\alpha = 45°$, $\mathcal{M} = 1$, $n_\mathrm{s} = 0.01$) with u_0 10 times and 50 times stronger, i.e., $u_0 = 0.1c_\mathrm{s}$ and $u_0 = 0.5c_\mathrm{s}$, respectively. The simulation with $u_0 = 0.1c_\mathrm{s}$ does not show a significant difference compared to the fiducial one. The simulation with $u_0 = 0.5c_\mathrm{s}$ exhibits stronger mixing between the stream and the CGM leading to higher cold stream mass growth.

Chapter 4

Results

4.1 General evolution and emission of the stream

4.1.1 Fiducial results from HD simulations

We provide an overview of the stream's evolution based on our HD simulations. In Fig. 4.1, we present temperature maps from HD simulations, each corresponding to different $\xi = t_{\rm cool}/t_{\rm sh}$ ratios at early ($t = 0.8t_0$), intermediate ($t = 11t_0$), and final ($t = 22t_0$) times. The displayed maps, rotated by 90° compared to Fig. 3.1, illustrate the stream's fate determined by ξ. As detailed in Sec.2.5, when $\xi < 1$ (the *condensing stream* regime), CGM gas condenses onto the stream, increasing its mass. Conversely, for $\xi > 1$ (the *disrupting stream* regime), more cold stream gas mixes into the CGM, leading to stream disruption. This aligns with Mandelker et al. (2020a) findings, for which, considering the same definition of ξ, the evolution of the stream was also divided in those two regimes. The simulation at $\xi \sim 1$ represents the threshold at which cooling can sustain the cold stream mass but not efficiently cool the mixing layer gas, resulting in a relatively thick mixing layer. At this limit, the stream fragments into large clouds ($> R_{\rm s}$) at a later stage due to the growth of longer wavelength KHI modes.

4.1.2 Evolution from MHD simulations

Fig. 4.2 displays temperature maps from MHD simulations at $t = 11t_0$, the half simulation time, for $\mathcal{M} = 1$ and $\delta = \rho_{\rm s}/\rho_{\rm cgm} = 100$, with varying values of $\xi = t_{\rm cool}/t_{\rm sh}$ and initial magnetic field angles. Comparing these maps with the middle column of Fig. 4.1, we observe that the magnetic field can significantly influence

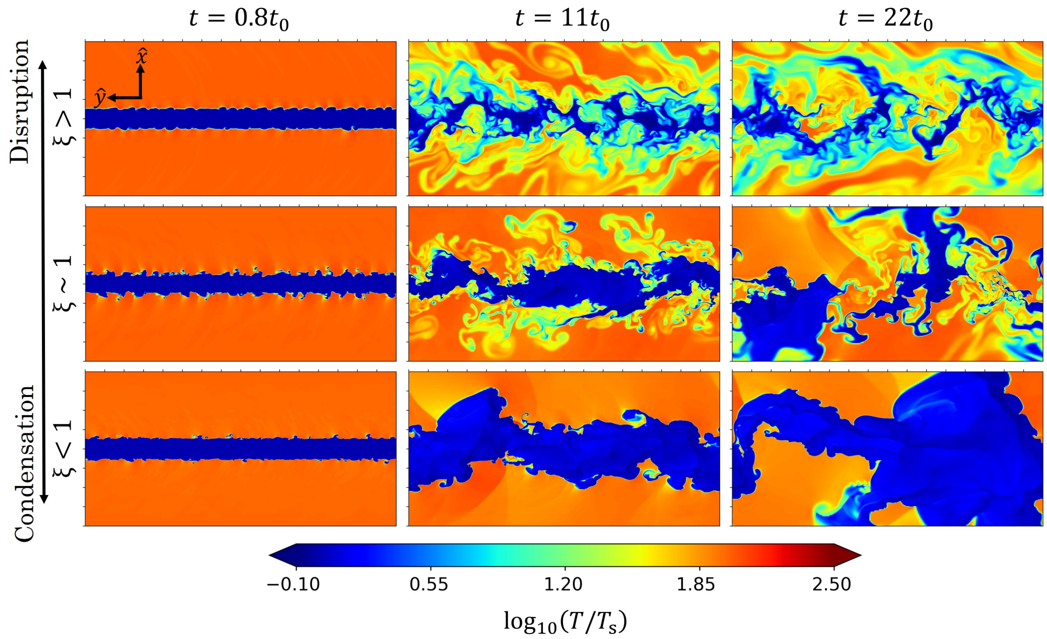

FIGURE 4.1: Maps of the gas temperature in the HD simulations at different times with a density contrast $\delta = 100$, for $\mathcal{M} = 1$, and for three different values of the ratio ξ (cooling time over shearing time). Each panel shows the full 32 kpc length in the y-axis (stream axis), and a zoomed region of 16 kpc in the x-axis (the vertical direction). The maps displayed are rotated by 90° compared to the illustration in Fig. 3.1.

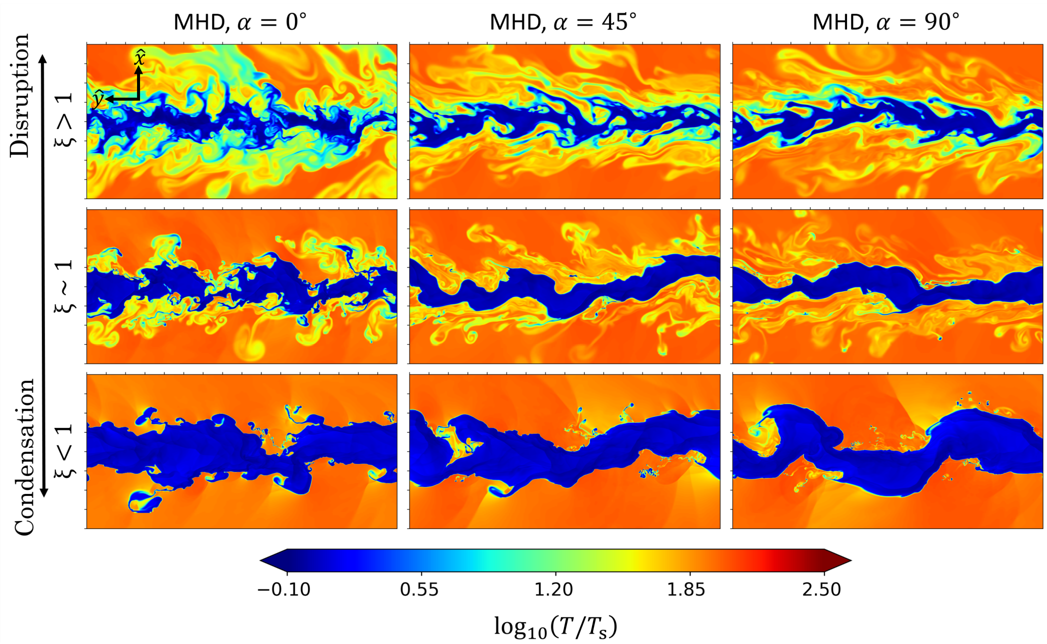

FIGURE 4.2: Maps of gas temperature in the MHD simulations for $\mathcal{M} = 1$, with a density contrast $\delta = 100$, with $\alpha = 0°, 45°, 90°$, and at a fixed time $t = 11\,t_0$. The top, middle, and bottom rows spans over the two different regimes defined by the ratio ξ. Each panel shows the full 32 kpc length in the y-axis (stream axis), and a zoomed region of 16 kpc in the x-axis (the vertical direction). The maps displayed are rotated by 90° compared to the illustration in Fig. 3.1.

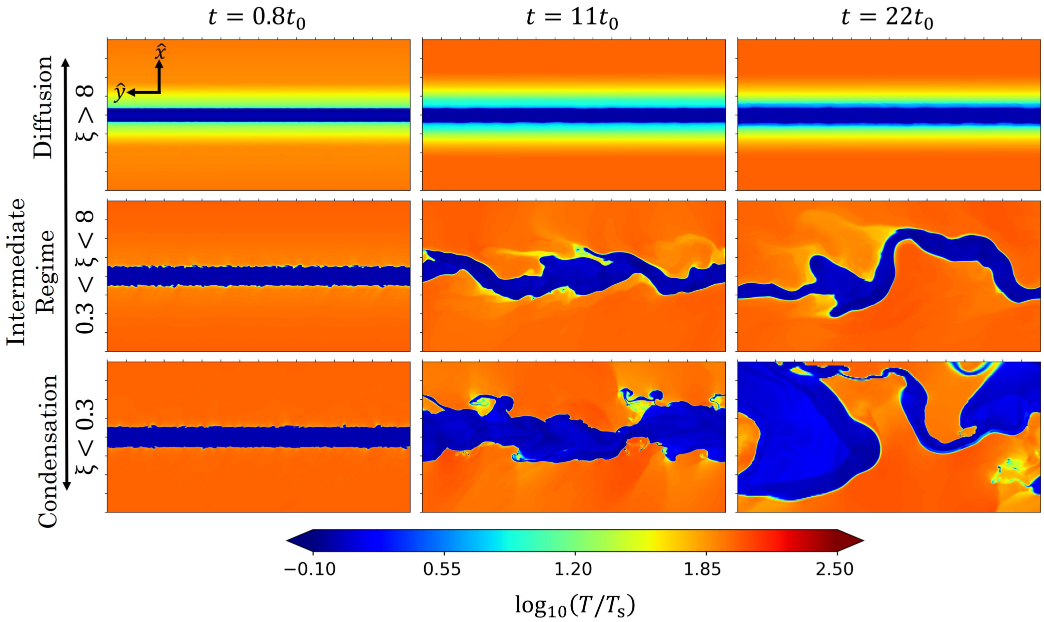

FIGURE 4.3: Maps of the gas temperature in the MHD+TC simulations at different times with a density contrast $\delta = 100$, for $\mathcal{M} = 1$, and for three different values of the ratio ξ (cooling time over shearing time) corresponding to the three different stream regimes in the presence of TC, i.e. *diffusing stream*, *intermediate*, *condensing stream* regimes (see Sec. 2.5). Each panel shows the full 32 kpc length in the y-axis (stream axis), and a zoomed region of 16 kpc in the x-axis (the vertical direction). The maps displayed are rotated by 90° compared to the illustration in Fig. 3.1.

stream evolution, primarily when the initial magnetic field is not aligned with the stream ($\alpha \neq 0°$) and when the stream is not in the *condensing stream* regime ($\xi \gtrsim 1$). The primary visual distinction is a reduction in the amount of gas in the mixing layer when $\alpha \neq 0°$,' particularly in the *disrupting stream* regime ($\xi > 1$). The initial magnetic field strength is relatively weak ($\beta = 10^5$), underscoring the need for a substantial increase in field strength to impact stream evolution, as elaborated in Sec. 4.2.3. Across all regime and values of ξ, the decrease of gas in the mixing layer is apparently due to the inhibition of surface modes.

4.1.3 Evolution from MHD+TC simulations

Fig. 4.3 displays temperature maps for MHD+TC simulations with varying $\xi = t_{\rm cool}/t_{\rm sh}$ ratios, all featuring an initial magnetic field angle of $\alpha = 45°$ at early, median, and final times ($t = 0.8, 11, 22t_0$, respectively).

In the *diffusing stream* regime ($\xi > 8$), as anticipated, thermal conduction (TC) effectively suppresses instabilities and diffuses the stream into the CGM. Initially, the rate of diffusion depends on the magnetic field angle and can be expressed as an efficiency parameter for the thermal conduction flux, such that $\mathbf{Q} = \mathbf{0}$ for $\alpha = 0°$.

Over time, the magnetic field lines bend at the stream-CGM interface, reducing conduction efficiency. Consequently, at $t = 22t_0$, thermal conduction becomes insufficient to counteract cooling, resulting in a slight increase in cold gas mass at later times.

Within the *intermediate* regime ($0.3 < \xi < 8$), TC diffuses the mixing layer and eliminates small-scale perturbations. This aligns with the fastest timescale τ_{p} in the *intermediate* regime, governing the diffusion of small cold clumps of size $0.1R_{\mathrm{s}}$. Thus, TC stabilizes the stream against small-scale surface modes, as a consequence of mixing layer structures and perturbations diffusing into the CGM.

In the *condensing stream* regime ($\xi < 0.3$), there are minimal differences between HD, MHD, and MHD+TC simulations. Notably, in later stages of MHD+TC simulations, the stream begins to fragment into large cold clumps. This evolution is also observed in MHD simulations and results from the magnetic field's tension force, inhibiting only smaller-scale perturbations (Berlok & Pfrommer, 2019b). Consequently, as time progresses, longer wavelength KHI modes grow sufficiently to induce stream fragmentation.

4.1.4 Cold stream mass and emission

To evaluate cooling within the mixing layer, we calculate the net cooling emission for gas cells with temperatures below a threshold $T_{\mathrm{u}} = (T_{\mathrm{mix}} + T_{\mathrm{cgm}})/2$. This threshold specifically addresses emissions within the mixing layer[1]. In equilibrium between heating from the UV background and cooling, the gas in the stream contributes negligible net cooling, and hence, we don't need to use a lower bound for the cooling emissions. We observed that slight variations in the threshold have minimal impact on our results. It's important to note that we exclusively consider net cooling. Accounting for cooling induced by photon ionization from the UV background might lead to an overestimation of total cooling, given that our simulations do not incorporate self-shielding. The cooling rate is integrated across all gas below T_{u} and subsequently averaged over time, starting when the mixing layer achieves quasi-steady state:[2]

$$L_{\mathrm{net}} = \left\langle \pi R_{\mathrm{s}} \iint_{\mathrm{ML}} \rho^2 \left(\Lambda - \mathcal{H}\right) \mathrm{d}x\mathrm{d}y \right\rangle_{\log_{10}}, \tag{4.1}$$

[1] Appendix B provides an in-depth discussion and analysis of these thresholds.

[2] In practice, a fixed time of $t = 5t_0$ is applied to all simulations. As evident in the time profile plot in Appendix A and Sec. 4.2.3.2, the mixing layer in all simulations reaches quasi-steady state (as defined in Equation 4.3), characterized by nearly constant stream mass growth/loss, net cooling emissions, and magnetic field growth.

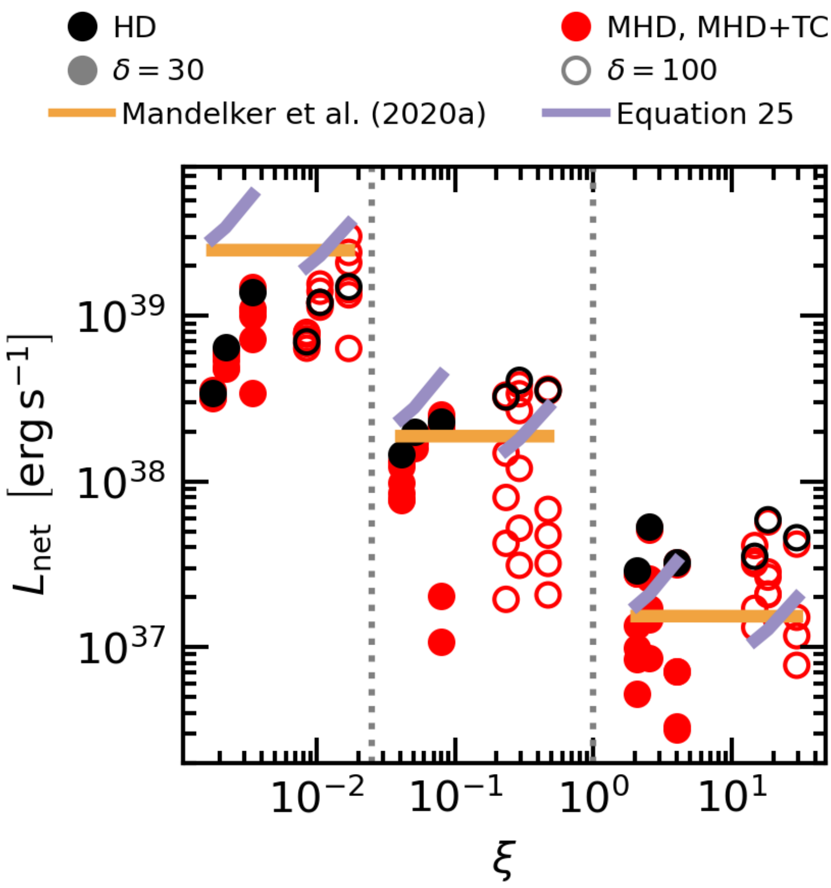

FIGURE 4.4: Average cooling emission in the mixing layer for all simulations. Black points red points refer to the HD simulations and the MHD and MHD+TC simulation, respectively. Analytical models from Mandelker et al. (2020a) and models from our fitted value of the condensation speed $v_{\rm in}$ are plotted in orange and purple, respectively. *Details of the distribution of the points:* Filled and open circles represent simulations with $\delta = 30$ and 100, respectively. From left to right, the vertical grey dotted lines delimit the regions with simulations with $n_{\rm s} = 10^{-1}, 10^{-2}, 10^{-3}\,{\rm cm}^{-3}$. For a subgroup of points with a given δ and $n_{\rm s}$, the variation of ratio ξ originate from their Mach number $\mathcal{M} = 0.5, 1, 2$ from left to right.

where the factor $\pi R_{\rm s}$ represents integration around the stream axis to mimic a cylindrical stream. The stream radius is $R_{\rm s} = 1\,{\rm kpc}$ in all our simulations. The brackets define the time log-average[3],

$$\langle X \rangle_{\log_{10}} = 10^{\sum \log_{10}(X_i)/N} \tag{4.2}$$

with N the total number of averaged variables X_i.

[3]In a few simulations with strong cooling ($\xi < 10^{-2}$), the stream grows in size, and the mixing layer is shifted to regions with lower resolutions leading to excessive cooling due to the lack of resolution (see Fielding et al., 2020). The log-average allows us to smooth out the effect of those peaks, without changing results for all other simulations.

The resultant net cooling emission is depicted in Fig. 4.4 as a function of ξ across all simulations. Generally, the HD simulations exhibit the highest $L_{\rm net}$ values compared to the MHD and MHD+TC simulations for nearly all ξ values. In relative terms, the net cooling emissions in the HD simulations align with those reported by Mandelker et al. (2020a, Fig. 13) from their three-dimensional simulations. To note, most of their simulations correspond to our $n_{\rm s} = 10^{-2}\,{\rm cm}^{-3}$ scenarios, albeit with a larger radius ($R_{\rm s} = 3\,{\rm kpc}$). Our $L_{\rm net}$ values closely match theirs after accounting for a factor of approximately 10 multiplication, which not only considers the change in $R_{\rm s}$ in equation 4.1 but also a factor due to the enhanced condensation from the consequent lower ξ.

For $\xi \lesssim 0.05$, the HD simulations exhibit a maximum factor of 5 difference compared to MHD and MHD+TC simulations. However, for $\xi \gtrsim 0.05$, discrepancies increases to approximately a factor of ~ 20, signifying a notable reduction in the stream's emission signature when incorporating magnetic fields and thermal conduction. It's essential to note that these differences originate from both magnetic fields and thermal conduction. To ease comparison with analytical models, we plot both the model from Mandelker et al. (2020a, equations 31 and 37) and our fitted model. Similar to recent simulations of individual planar mixing layers (Fielding et al., 2020, Tan et al., 2021, Yang & Ji, 2023), we model cooling emission under the assumption that the mixing layer has attained a quasi-steady state concerning its energetics. In physical terms, this quasi-steady state represents a balance between the flux of kinetic energy, enthalpy, and the net radiative cooling rate. In the hydrodynamic case, this quasi-steady state can be expressed as,

$$\nabla \cdot [(e + p)\,\mathbf{u}] = \dot{e}_{\rm cool}, \tag{4.3}$$

which, upon integration over the mixing layer, results in,

$$L_{\rm cool} = v_{\rm in} \left(\frac{\gamma}{\gamma - 1} p + \frac{\gamma}{2} p \mathcal{M}^2 \right) S, \tag{4.4}$$

where S represents the surface between the stream and the background, and $L_{\rm cool}$ denotes the cooling emission in the mixing layer. To obtain $v_{\rm in}$, we first calculate the stream mass growth rate $\dot{M}_{\rm s}$ from the simulations (as later shown in equation 4.7). Considering Equation 2.28, we then compute the simulation's $v_{\rm in,sim}$, taking into account the surface of a cylindrical stream with $S = 32 R_{\rm s} \times 2\pi\,{\rm kpc}^2$. The mixing velocity $v_{\rm in}$ is subsequently fitted directly from the simulation values $v_{\rm in,sim}$ obtained using Equation 2.28. The fit for the only the HD results yields,

$$v_{\rm in} \sim 0.4 \xi^{-1/4}. \tag{4.5}$$

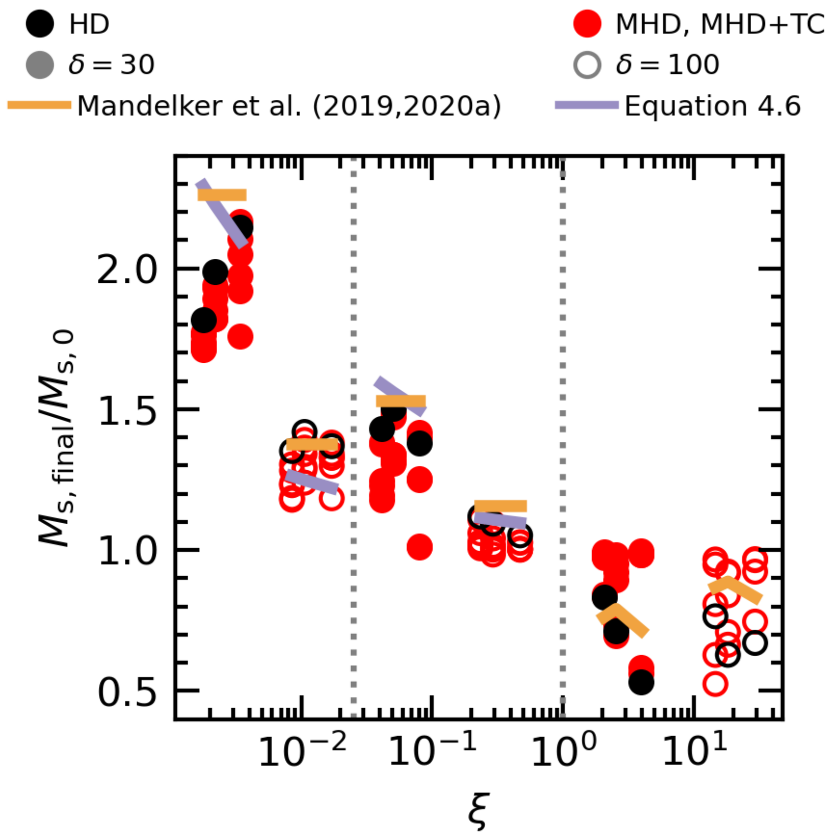

FIGURE 4.5: Cold mass of the stream at the final simulation time for all simulations. Black points red points refer to the HD simulations and the MHD and MHD+TC simulation, respectively. Analytical models from Mandelker et al. (2020a) (for $\xi < 1$) and Mandelker et al. (2019) (for $\xi > 1$), and model from our fitted value of the condensation speed $v_{\rm in}$ are plotted in orange and purple, respectively. The detailed distribution (grey dashed lines, filled and open circles) of the points is the same as in Fig. 4.4.

Both models provide a rough approximation of the expected emissions of the HD simulations. Our model shows an average factor difference of ~ 1.5 and a maximum factor difference of ~ 7.3. Conversely, the models presented by Mandelker et al. (2020a, equations 31 and 37) display a flat trend. This variance can be attributed to their adoption of different definitions for the relevant timescales for ξ. Moreover, their model assumes that the cooling emission primarily results from thermal energy loss by the hot CGM gas. In contrast, our approach considers the energetic quasi-steady state within the mixing layer, linking the cooling emission to the mixing layer's gas enthalpy.

To study the evolution of the stream mass, we compute the total cold mass in each simulation. The cold stream mass is defined as the gas below a temperature threshold $T_{\rm d} = (T_{\rm s}T_{\rm mix})^{1/2}$[4]. The final mass, denoted as $M_{\rm s,final}$, is obtained through integration over all domains.

Fig. 4.5 presents the final stream mass normalized by its initial value for all simulations. Among simulations with $\xi < 1$ and $\xi > 1$, the HD simulations represent the maximum and minimum cases of mass growth and loss, respectively. The differences between HD and MHD/MHD+TC simulations are less pronounced than for cooling emissions, showing a maximum difference of $\sim 0.4\, M_{\rm s,0}$. It's noteworthy that for simulations with $\xi > 1$, corresponding to the *disrupting stream* regime for HD and MHD simulations, some simulations exhibit a final stream mass very close to their initial value, indicating that MHD and MHD+TC can, in some cases, stabilize the stream against KHI.

Our numerical results are compared to analytical models in Fig. 4.5. Using our fitted value of $v_{\rm in}$ from equation 4.5, we recover the steady mass growth $\dot{M}_{\rm s}$ from equation 2.28. The theoretical final stream mass is then expressed as,

$$\frac{M_{\rm s,th}\,(t)}{M_{\rm s,0}} = 1 + \frac{\dot{M}_{\rm s}}{M_{\rm s,0}}\frac{t}{t_0}, \tag{4.6}$$

with $t = 22t_0$ being the final simulation time. The predicted final mass from our model, and that from Mandelker et al. (2019) for $\xi > 1$, and Mandelker et al. (2020a) for $\xi < 1$, are in reasonable agreement with the results of the HD cases. For simulations with $\xi > 1$, the theoretical prediction is not applicable, as it assumes CGM gas condensation onto the stream. Instead, we present the expected mass loss rate based on the deceleration of the stream $V_{\rm s}\,(t)$ from Mandelker et al. (2019, equations 10 and 38) for two dimensions. Quantitatively, the predicted mass loss rate also roughly agrees with the simulated values.

[4]Notably, variations in this threshold temperature have a minimal impact on our results, altering the cold mass by only a few percent.

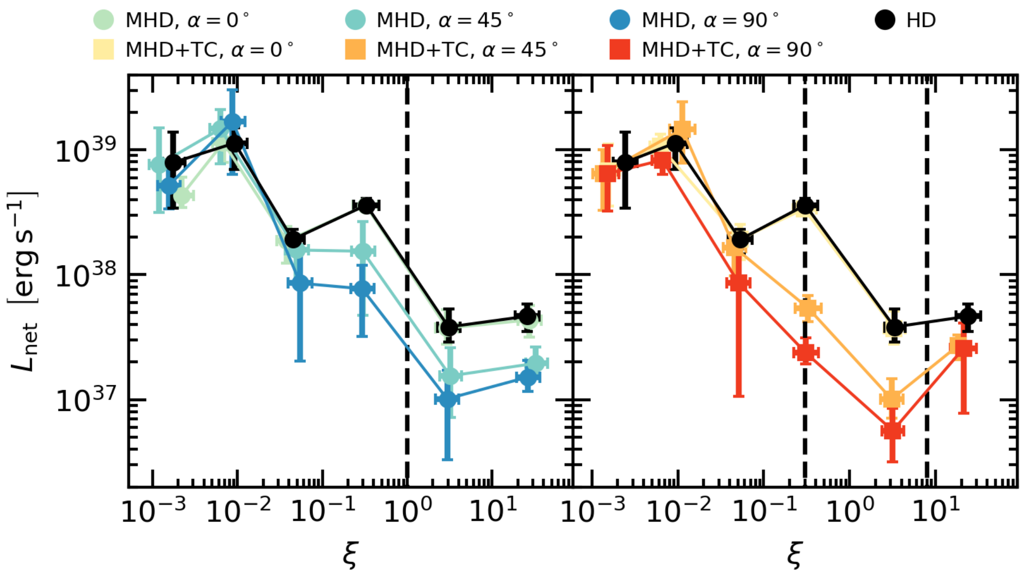

FIGURE 4.6: Net cooling emission in the mixing layer. *Left panel:* Comparison between HD and MHD simulations. The vertical dashed black line represents the limit between the *condensing stream* regime ($\xi < 1$) and the *disrupting stream* regime ($\xi > 1$). *Right panel:* Comparison between HD and MHD+TC simulations. The vetical black dashed lines represent the boundaries between the *condensing stream* regime ($\xi < 0.3$), the *intermediate* regime ($0.3 < \xi < 8$), and the *diffusing stream* regime ($\xi > 8$). Each point are an averaged value of the three Mach numbers $\mathcal{M} = 0.5, 1, 2$ for fixed $(n_{\rm s}, \delta, \alpha)$, with the error bars representing the range of minimum and maximum values. A small random offset in the x coordinate is included for clarity between the points.

4.2 Impact of magnetic field and thermal conduction

4.2.1 Cold stream emissions

4.2.1.1 Net emissions

The net cooling emissions, denoted as $L_{\rm net}$, for our simulations are depicted in Fig. 4.6. To improve clarity, each data point represents an average value across the three Mach numbers, $\mathcal{M} = 0.5, 1, 2$, for each simulation set, corresponding to each row in Table 3.2. The scatter denotes the range between the maximum and minimum values observed within the simulations for the three Mach numbers. A slight random offset is added to the abscissa for better visual distinction.

The influence of MHD becomes noticeable in the cooling emission $L_{\rm net}$ at $\xi \sim 0.1$. Above this threshold, the emission gradually decreases with increasing α, directly tied to the reduction of gas in the mixing layer, as illustrated in Fig. 4.2. Across all ξ values, MHD simulations with $\alpha = 0^\circ$ exhibit identical $L_{\rm net}$ compared to the HD simulations, while the difference reaches a factor of 10 for MHD simulations with $\alpha = 90°$.

Similarly, in line with the MHD simulations, MHD+TC starts to impact the emission $L_{\rm net}$ at $\xi \sim 0.1$, leading to a further decline. In the *condensing stream* regime ($\xi < 0.3$), thermal conduction does not significantly alter the emissions except when $\alpha = 90°$ and $\xi \sim 0.06$. Here, the cooling emission drops by a factor of 20 compared to the HD case, although this decrease is observed only at a specific Mach number ($\mathcal{M} = 2$), as indicated by the scatter. The scatter can be attributed to the influence of stream velocity on magnetic field growth, as elaborated in the following section.

Within the *intermediate* regime ($0.3 < \xi < 8$), thermal conduction further reduces cooling emissions in MHD+TC by over a factor of $\gtrsim 2$ compared to MHD, particularly for simulations with $\alpha \neq 0°$. As evident from the temperature maps in Fig. 4.3 and consistent with the definition of the *intermediate* regime in Sec. 2.5, thermal conduction diffuses the mixing layer, resulting in a smaller amount of gas in the temperature range $T_{\rm s}$–$T_{\rm mix}$ available for efficient cooling and radiation. Notably, within this regime, thermal conduction also mitigates the dependence of $L_{\rm net}$ on $\mathcal{M}$ when compared to MHD simulations.

In the *diffusing stream* regime ($\xi \gtrsim 8$), the stream exhibits a slight enhancement in its emission for $\alpha \neq 0°$ compared to the MHD+TC simulations at $\xi \sim 3$. As the stream diffuses, a significant amount of gas is heated beyond the radiative temperature equilibrium in the stream, $T_{\rm s} \sim 10^4\,{\rm K}$, resulting in more gas available to radiatively cool. As detailed in Sec. 4.2.1.2, in the *condensing stream* and *intermediate* regimes, the dominant cooling processes are governed by hydrogen. However, in the *diffusing stream* regime, the contribution from hydrogen actually decreases and accounts for approximately $4-10\%$ of the total cooling emission. The overall increase in the total cooling emission can be attributed to helium and various metals such as oxygen and neon.

4.2.1.2 Emission composition

We now investigate the contribution of hydrogen to the overall net cooling emission. Using the cooling model described in Sec. 2.2.2, we calculate the ratio of hydrogen's net cooling emission to the total net cooling emission within the mixing layer. This ratio holds significance in estimating the portion of the emission associated with Lyα. Both cooling emissions are computed using Equation 4.1.

Fig. 4.7 presents a comparison of the ratio $L_{\rm H,net}/L_{\rm net}$ between HD and MHD, as well as between HD and MHD+TC simulations as a function of $\xi = t_{\rm cool}/t_{\rm sh}$. For

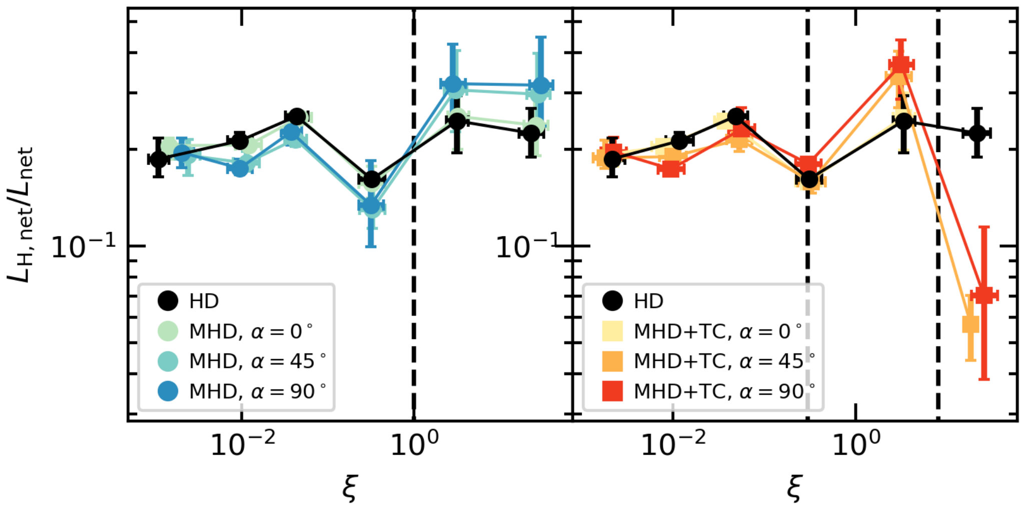

FIGURE 4.7: Ratio of the cooling emission contribution from hydrogen (L_{H}) over the total cooling emission in the mixing layer (L_{net}) as a function of ξ *Left panel:* Comparison between HD and MHD simulations. The vertical dashed black line represents the limit between the *condensing stream* regime ($\xi < 1$) and the *disrupting stream* regime ($\xi > 1$). *Right panel:* Comparison between HD and MHD+TC simulations. The vetical black dashed lines represent the boundaries between the *condensing stream* regime ($\xi < 0.3$), the *intermediate* regime ($0.3 < \xi < 8$), and the *diffusing stream* regime ($\xi > 8$). Each point are an averaged value of the three Mach numbers $\mathcal{M} = 0.5, 1, 2$ for fixed $(n_{\mathrm{s}}, \delta, \alpha)$, with the error bars representing the range of minimum and maximum values. A small random offset in the x coordinate is included for clarity between the points.

HD simulations, the ratio remains relatively constant across different values of ξ, hovering around ~ 0.2, showcasing minimal dependence on the stream velocity. Conversely, the MHD simulations impact this ratio differently depending on the stream regime and for angles $\alpha \neq 0°$.

In the *condensing stream* regime ($\xi < 1$), the hydrogen contribution exhibits a slight decrease, whereas in the *disrupting stream* regime ($\xi > 1$), it increases to approximately 0.3. It is worth noting that as ξ increases, the stream velocities also impact the hydrogen contribution, leading to values of $L_{\mathrm{H,net}}/L_{\mathrm{net}}$ of up to ~ 0.45.

Thermal conduction does not significantly alter the results within the *condensing stream* regime. In the *intermediate* regime, MHD+TC appears to increase $L_{\mathrm{H,net}}/L_{\mathrm{net}}$ to $\lesssim 0.4$ as ξ increases. Finally, within the *diffusing stream* regime, the hydrogen contribution in the cooling emissions notably diminishes, falling within the range of 0.03–0.1, contingent on both stream velocity and angle α, as both factors directly influence thermal conduction efficiency.

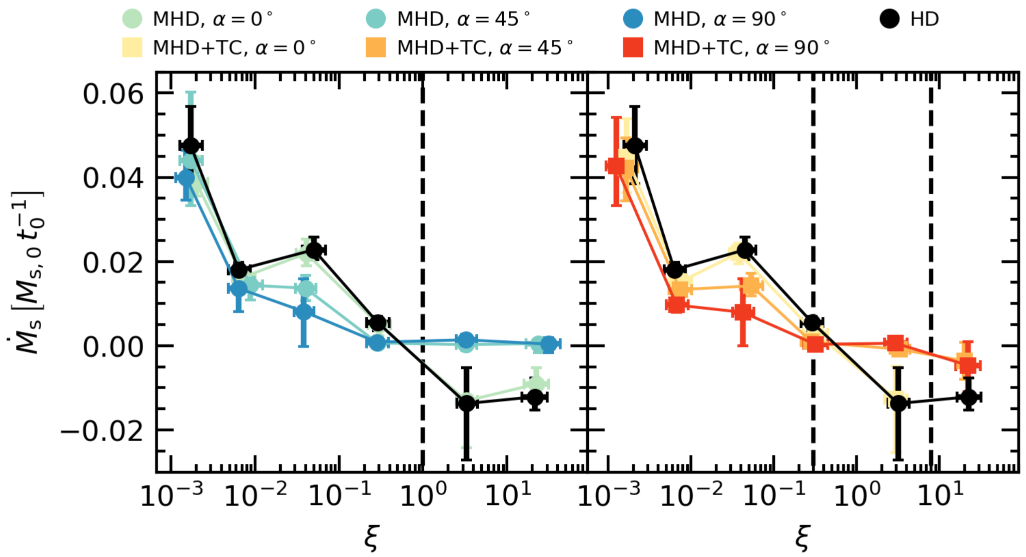

FIGURE 4.8: Stream mass rate in units of stream initial mass per $t_0 = R_\mathrm{s}/c_\mathrm{s}$ as a function of ξ. *Left panel:* Comparison between HD and MHD simulations. The vertical dashed black line represents the limit between the *condensing stream* regime ($\xi < 1$) and the *disrupting stream* regime ($\xi > 1$). *Right panel:* Comparison between HD and MHD+TC simulations. The vetical black dashed lines represent the boundaries between the *condensing stream* regime ($\xi < 0.3$), the *intermediate* regime ($0.3 < \xi < 8$), and the *diffusing stream* regime ($\xi > 8$). Each point are an averaged value of the three Mach numbers $\mathcal{M} = 0.5, 1, 2$ for fixed $(n_\mathrm{s}, \delta, \alpha)$, with the error bars representing the range of minimum and maximum values. A small random offset in the x coordinate is included for clarity between the points.

4.2.2 Mass evolution

We also calculate the mean stream mass growth/loss to provide a more comprehensive representation of the stream's mass evolution,

$$\dot{M}_\mathrm{s} = \left\langle \frac{\mathrm{d}M_\mathrm{s}}{\mathrm{d}t} \right\rangle, \tag{4.7}$$

where the $\langle\rangle$ notation signifies linear arithmetic averaging over time, spanning from the commencement of the quasi-steady state in the mixing layer to the conclusion of the simulation, mirroring the log-averaging approach used for L_net.

The stream mass growth/loss, denoted as $\dot{M}_\mathrm{s}$, is displayed in Fig. 4.8 for HD, MHD, and MHD+TC scenarios. Within the *condensing stream* regime ($\xi < 1$), MHD simulations exhibit a slight decrease in stream mass growth, on the order of $\lesssim 10\%$, in comparison to the HD simulations. An exception arises at $\xi \sim 0.06$, where MHD simulations progressively reduce the stream mass growth with increasing α. Notably, minimal distinctions are observed between HD simulations and MHD simulations with $\alpha = 0°$. Within the *disrupting stream* regime ($\xi > 1$), MHD simulations exert

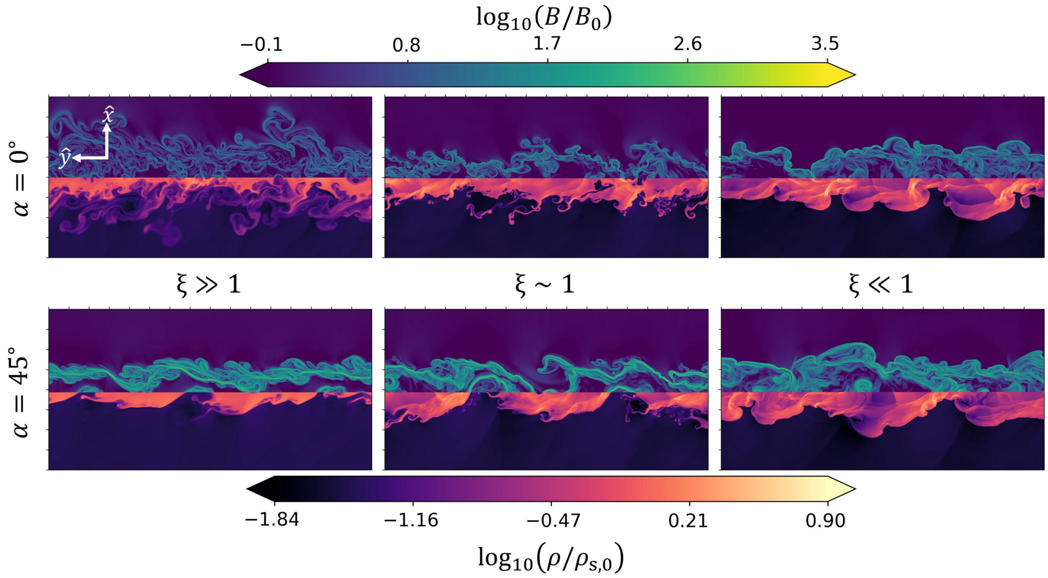

FIGURE 4.9: Comparison of the magnetic field (top) and density (bottom) at the half time $t = 11\,t_0$ in MHD+TC simulations with $\alpha = 0°$ (field aligned to the stream) and $\alpha = 45°$. From left to right, the maps show the simulations with decreasing ξ. Each panel shows the full 32 kpc length in the y-axis (stream axis), and a zoomed region of 16 kpc in the x-axis (the vertical direction). The maps displayed are rotated by 90° compared to the illustration in Fig. 3.1.

a substantial influence. Streams with $\alpha \neq 0°$ do not undergo mass loss in contrast to HD and MHD simulations with a magnetic field parallel to the stream ($\alpha = 0°$).

Thermal conduction impacts the stream mass evolution solely for $\xi > 8$, which corresponds to a stream in the *diffusing stream* regime. As anticipated, in such instances, the stream diffuses into the CGM. However, the effectivity of the conduction can significantly drop by the initial magnetic field angle and the bending of field lines over time. Consequently, this results in a stable stream with nearly no mass loss, particularly for both $\mathcal{M}$ and α increase.

4.2.3 Magnetic field growth

4.2.3.1 General evolution

We now focus on the amplification of the magnetic field. Fig. 4.9 depicts contour plots illustrating the magnetic field strength and density for angles $\alpha = 0°$ and $\alpha = 45°$ at various ξ values. These contours are derived from MHD+TC simulations with $\delta = 30$. Notably, they do not exhibit qualitative distinctions from the MHD simulations or those with $\delta = 100$, provide that $\xi < 8$, i.e., outside the *diffusing stream* regime. In all these contour plots, the magnetic field increases at the interface of the stream and the surrounding CGM, as well as within the stream itself.

In cases where the magnetic field is initially parallel to the stream ($\alpha = 0°$), the magnetic field can amplifies mainly by two processes. First, the field lines undergo stretching due to the eddies generated by the Kelvin-Helmholtz instability (KHI). Second, in case of condensation, as the field is frozen to the flow, the field is compressed. As ξ decreases, a slightly greater magnetic field amplification is observed.

For simulations with $\alpha = 45°$, there exists no significant disparity in magnetic field amplification across varying ξ values. Here, the magnetic field is magnified by up to a factor of $\sim 500B_0$, surpassing the amplification observed in the $\alpha = 0°$ simulations. This increase in magnetic field strength can be attributed to the presence of a component perpendicular to the stream, which continually undergoes stretching as the stream is advected.

4.2.3.2 Modeling of the amplification

We now focus on the modeling of magnetic field amplification due to shear velocity, the principal mechanism underlying the magnetic field growth illustrated in Fig. 4.9. Given that our magnetic field initially is uniform, we can simplify the analysis by focusing exclusively on the direction of a magnetic field line and representing it as a flux tube (Spruit, 2013). This flux tube has an initial density $\rho_{\rm i}(x)$ and length $l_{\rm i}$.

The total length of the magnetic field line can be approximated as $l(t) \sim l_{\rm i} + v_{\rm s,0}t$, with the elongation occurring primarily near the interface between the stream and the CGM. This results in a condition where $l_{\rm i}/R_{\rm s} \sim 1$. Our specific focus is on the segment of the field line that undergoes this elongation. As the stream advances, the field line will experience bending at the interface between the stream and the CGM. We assume that this bending only takes place along the initial section of the line, with a length of $R_{\rm s}$, positioned between each side of the interface $[0.5R_{\rm s}, 1.5R_{\rm s}]$ [5].

As the magnetic field is frozen into the flow, the total mass along the field line and the magnetic flux should remain constant,

$$M(x) = \rho(x,t)\,\sigma(t)\,l(t) = M_0, \quad \text{and} \quad \Phi = \sigma(t)\,B(t) = \Phi_0, \tag{4.8}$$

where $\sigma(t)$ represents the cross-section of the tube.

The total pressure should remain constant as well, defined as $p_{\rm T} = p + B^2/2 = p_0 + B_0^2/2$. Assuming a cold stream without perturbations, we can consider the

[5] This assumption aligns well with our simulation observations, as evident in Fig. 4.9. It indicates that, within a given stream cross-section, amplification predominantly occurs around the interface and is absent near the central region of the stream.

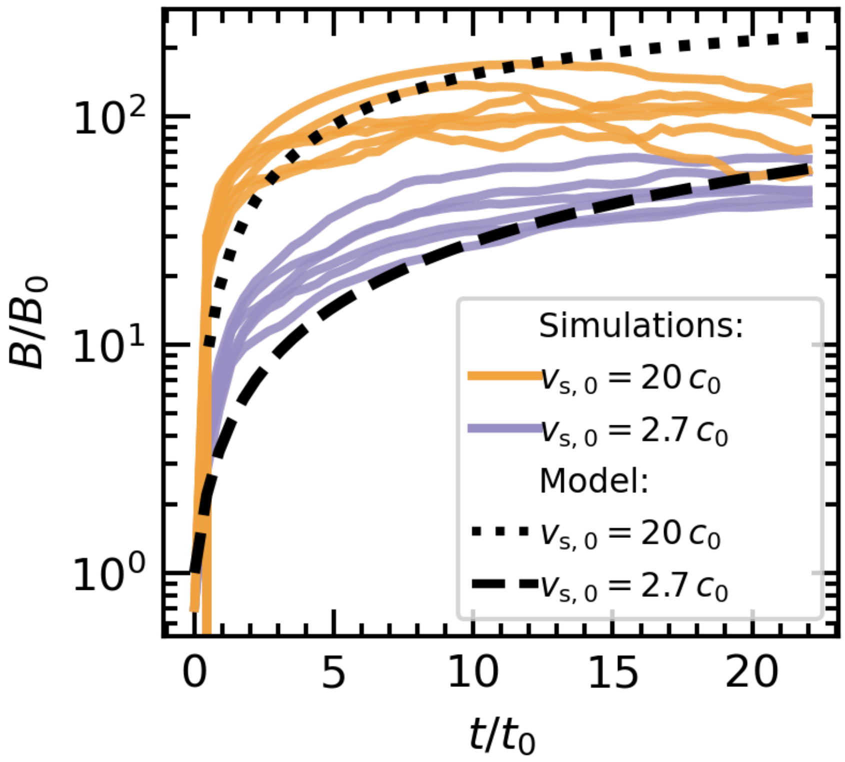

FIGURE 4.10: Comparison of the temporal magnetic field evolution between the simulations and our model from Equation 4.9. For clarity, only MHD simulations are plotted in cases with maximum (orange) and minimum (blue-navy) magnetic field growth, i.e., the cases where the stream velocity is the highest and lowest. All the lines with a same color are MHD simulations with the fixed $v_{\mathrm{s},0}$ and different $\alpha = 45°, 90°$ and $n_{\mathrm{s}} = 10^{-3}, 10^{-2}, 10^{-1}\,\mathrm{cm}^{-3}$ (leading to 6 lines per color).

tube to have a constant temperature $T(x,t) = T_0(x)$. Using the ideal gas law and substituting Equation 4.8 into the total pressure term, we can derive the following solution for magnetic field growth,

$$\frac{B(t)}{B_0} = \frac{1}{2}\left[\left(\beta\frac{l_{\mathrm{i}}}{l}\right)^2 + 4(\beta+1)\right]^{1/2} - \frac{1}{2}\beta\frac{l_{\mathrm{i}}}{l}, \tag{4.9}$$

where $\beta = p_0/\left(B_0^2/2\right) = 10^5$ represents the ratio of thermal pressure to magnetic pressure. It's important to note that in Equation 4.9, the time dependence is encapsulated within l.

We show a comparison between the model and simulation results in Fig. 4.10. The magnetic field in the simulations is averaged within both the stream and the mixing layer, as detailed in the next section. For clarity, the figure focuses on simulations with $\alpha \neq 0°$ where the magnetic field growth is expected to be at its maximum and minimum. These correspond to simulations with the highest and lowest stream velocities, denoted as $\mathcal{M} = 2, \delta = 100$ and $\mathcal{M} = 0.5, \delta = 30$, respectively.

The flux tube model exhibits relatively good agreement with the simulations. It successfully captures the initial rapid growth, followed by an asymptotic trend around $t \sim 5t_0$. It's worth noting the influence of velocity, which also accelerates the time required to reach the asymptotic behavior. There are some disparities between our simplified flux tube model and the actual magnetic field evolution observed in the simulations. These differences can be attributed to several factors.

Firstly, our model assumes that the magnetic field grows infinitely and uniformly within the segment of length l. In reality, field growth is limited by energy equipartition, where $B^2/2 \sim \rho\Delta v^2/2$, and it isn't uniform, with more pronounced growth near the interface between the stream and the CGM. In the mixing layer, equipartition imposes a constraint of $B \lesssim (300\text{–}500) \times \mathcal{M}$, which is either higher or similar with the maximum magnetic field observed in our simulations. Since our model represents the average magnetic field in the stream, it doesn't reach such maximum values, resulting in a deviation from the point where it should stabilize. Moreover, in realistic scenarios, the magnetic field can experience amplification due to turbulent eddies and compression from condensation. These additional mechanisms for magnetic field amplification aren't considered in our simplified model, contributing to a faster intial growth of the magnetic field, leading to reaching the asymptotic trend more rapidly in the simulations compared to the model. Furthermore, the simulations might exhibit non-monotonic behavior of the magnetic field, while our model assumes a constant magnetic field growth. Factors such as stream deceleration, numerical magnetic diffusion, and the widening of the mixing length can all influence the growth and behavior of the magnetic field, leading to deviations from the predictions of the idealized model.

4.2.3.3 Mean magnetic field results

To quantify the growth of the magnetic field, we first calculate the magnetic energy E_{m} averaged within the stream and the mixing layer, which is defined as the region below the temperature threshold T_{u} specified in Sec. 4.1.4. This calculation is expressed as,

$$B = \left(2\left\langle E_{\mathrm{m}}\right\rangle\right)^{1/2}, \tag{4.10}$$

with here, the angle brackets $\langle\rangle$ denote linear-arithmetic time averaging, consistent with Equation 4.7. The results for the B_{y} component are illustrated in Fig. 4.11. We specifically focus on this component because it is the one primarily amplified by the velocity shear term, which serves as the dominant mechanism for amplification in

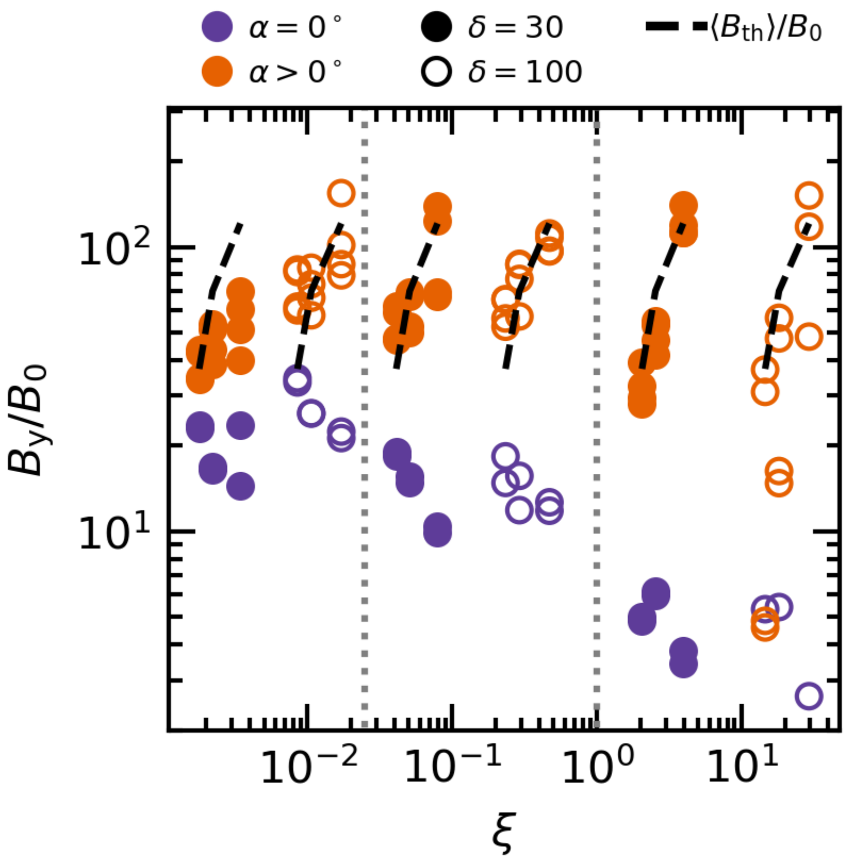

FIGURE 4.11: Time-averaged magnetic field B_y in unit of B_0 in the stream and mixing layer region for all MHD and MHD+TC simulations in function of ratio ξ. The blue-navy points refer to simulations with $\alpha = 0°$, and the orange points refer to simulations with $\alpha \neq 0°$ (i.e., 45° or 90°). The black dashed lines represent the time-average of our model value $\langle B_{th} \rangle$. The detailed distribution of the points (grey dashed line, filled and open circles) is the same as in Fig. 4.4.

our case. From the magnetic induction equation in Equation 3.1, considering our geometry and initial conditions, it becomes apparent that initially, $\partial_t B_y \sim B_{x,0} \partial_x v_{y,0}$ is the dominant term when $\alpha \neq 0$. This observation is supported by the data in Fig. 4.11, which clearly shows that in simulations where $\alpha = 0°$, meaning $B_{x,0} = 0$, magnetic fields exhibit considerably lower amplification compared to simulations with $\alpha > 0°$. When considering B_x and plotting B, our results remain consistent. Simulations with $\alpha = 0°$ and those with $\alpha \neq 0°$ display distinct trends, aligning with our qualitative observations in Fig. 4.9. In simulations where the magnetic field is parallel to the stream, we observe a peak of approximately 20–35B_0 at $\xi \lesssim 2 \times 10^{-2}$, followed by a gradual decline to around $B \sim 3B_0$ for $\xi \sim 10$. This decrease follows a nearly constant slope, described as $B \propto \xi^{-0.16}$. The scatter in the data remains relatively stable along this slope and primarily stems from variations in the Mach number ($\mathcal{M}$) and the density ratio (δ) among the simulations.

In contrast, when the magnetic field includes a component perpendicular to the stream ($\alpha > 0°$), the mean magnetic field amplifies to approximately 30–150B_0 across different ξ values, with the primary increase being in the scatter between the data points as ξ rises. Furthermore, for fixed δ and $n_{\rm s}$, the magnetic field grows as ξ increases (i.e., with increasing $\mathcal{M}$ and constant δ and $n_{\rm s}$). This trend aligns with the notion that the primary driver of magnetic field growth is the velocity shear occurring at the interface between the stream and the CGM, particularly when $\alpha \neq 0°$.

Considering the magnetic field amplfication model described in the previous section, we have for $\alpha \neq 0°$,

$$\frac{B_{\rm th}\left(t\right)}{B_0} = \frac{1}{2}\left[\left(\beta\frac{R_{\rm s}}{R_{\rm s}+v_{\rm s,0}t}\right)^2 + 4\left(\beta+1\right)\right]^{1/2} - \frac{1}{2}\beta\frac{R_{\rm s}}{R_{\rm s}+v_{\rm s,0}t}, \tag{4.11}$$

where here $\beta = 10^5$ represents the ratio of thermal pressure to magnetic pressure, and the term $R_{\rm s}/\left(R_{\rm s}+v_{\rm s,0}t\right)$ indicates the stretching of field lines over time. To show the consistency of our model with simulations where $\alpha > 0°$, we enforce the ξ dependence of $B_{\rm th}$ in Equation 4.11 with $v_{\rm s,0} = \xi \times R_{\rm s}/\left(\alpha t_{\rm cool}\right)$ using Equations 2.29 and 2.40. The average value of our model, denoted as $\langle B_{\rm th}\rangle$, is plotted in Fig. 4.11. It is worth noting that our model also effectively captures the time variation of the magnetic field, as shown in Fig. 4.10.

Notably, the resulsts for cases with $\alpha > 0°$ and $\xi > 10$ display relatively modest magnetic field growth. Specifically, these points correspond to MHD+TC simulations in the *diffusing stream* regime. As the stream diffuses into the CGM, the shear layer expands, diminishing the bending of field lines caused by velocity difference. Consequently, this leads to a reduced growth in the magnetic field.

The magnetic field experiences an approximately 100-fold increase, resulting in a substantial decrease in the average value of β from its initial average of approximately 10^5 to around ~ 10. This decrease in β arises because the magnetic field is not significantly amplified at the center of the stream, and the average thermal pressure remains relatively constant in this region.

However, as illustrated in Fig. 4.9, the magnetic field can be significantly amplified to values exceeding 200 to 500 times its initial strength, near the interface between the CGM and the stream. This amplification leads to values of β around 1 and actual magnetic field strengths exceeding $0.2\,\mu$G. This enhanced magnetic field strength explains the stabilization of the stream observed in the *disrupting stream* regime, as depicted in the mass rate plot shown in Fig. 4.8. These findings align with the conclusions of Berlok & Pfrommer (2019b), who determined that magnetic fields exceeding $0.4\,\mu$G, with initially a field aligned with the stream, exhibit sufficient magnetic tension to counteract the Kelvin-Helmholtz instability and stabilize the stream.

Hence, even though the magnetic field strength is initially relatively low, it is potentially significantly enhanced. This enhancement has a notable impact on both the emission characteristics of the stream and its evolutionary behavior, provided that the magnetic field is not aligned parallel to the stream.

4.2.4 Stream kinematics

4.2.4.1 Stream deceleration

Our simulations does not consider any source of gravitational force, hence the cold streams either keeps a constant velocity or ultimately decelerates due to momentum transfer. The mean stream deceleration of the stream $\dot{V}_{\mathrm{s}}$ is defined similarly to the stream mass rate in Equation 4.7,

$$\dot{V}_{\mathrm{s}} = \left\langle \frac{dV_{\mathrm{s}}}{dt} \right\rangle . \tag{4.12}$$

Fig. 4.12 shows the mean stream deceleration for all simulations. For decreasing ξ, the deceleration is increasing which clearly indicates that the condensation and the KHI are the main source of momentum transfer. Using the conservation of the momentum we can states that

$$\frac{\dot{V}_{\mathrm{s}}}{V_{\mathrm{s},0}} = -\frac{\dot{M}_{\mathrm{s}}}{M_{\mathrm{s},0}}. \tag{4.13}$$

Hence, using our fitted value of the condensing velocity v_{in} and Equation 4.7, we can obtain the resulting deceleration of the stream shown by the dashed black line. The deceleration obtained from the fit matches roughly the simulations data both in terms of value and trend. However the agreement for $\xi > 1$ should not be regarded, because in those regime the stream either have a decreasing or constant mass while our fitted model only consider condensation, i.e., the stream mass growth. In this case the deceleration is mainly due to the growth of KHI. For $\xi < 1$, the smaller is ξ, the higher is the mass growth of the stream, leading to a higher deceleration of the stream in order to keep a constant momentum. The fluctuations in the trend of the data and the model curve are due to the density ratio δ of each simulations. The smaller is δ and the higher is the density of the CGM gas leading to higher mass growth of the stream and higher deceleration. In accordance to the mass growth in

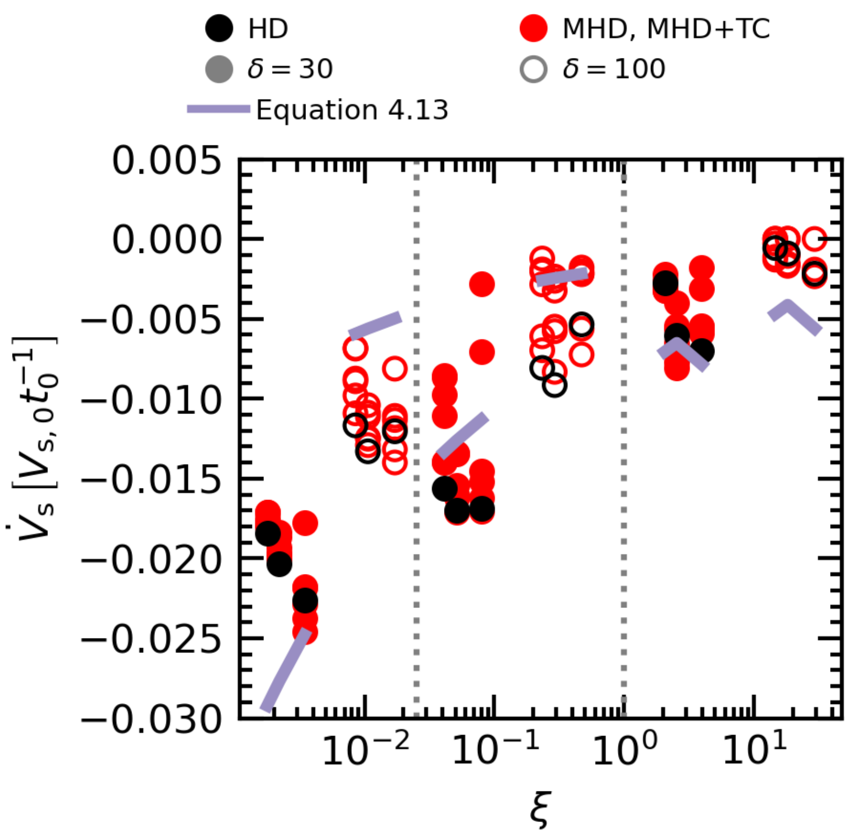

FIGURE 4.12: Stream deceleration in units of initial velocity per crossing time. Black points red points refer to the HD simulations and the MHD and MHD+TC simulation, respectively. Analytical model from our fitted value of the condensation speed v_{in} is plotted purple. The detailed distribution (grey dashed lines, filled and open circles) of the points is the same as in Fig. 4.4.

Fig. 4.5, in overall the HD simulations shows higher deceleration than their MHD and MHD+TC counterparts as they show higher mass growth.

We now focus on the impact of MHD and TC. In Fig. 4.13, we plot the stream deceleration rates where, similarly to Fig. 4.8 and Fig. 4.6, each points is an average over the different Mach number and where the error-bars represents the scatter from different Mach number with other simulation parameters fixed. In the MHD simulations, the deceleration rate decreases for α tending to 90°, i.e., for a stronger component of the magnetic field perpendicular to the stream, with simulations with $\alpha = 0°$ being almost identical to their HD counterparts. Similar is observed for the MHD+TC simulations, even though TC tend to decreases slightly more the deceleration of the stream. The decrease in the deceleration is the more drastic around $\xi \sim 0.1$ where the difference is up to factor 4 between HD and MHD+TC ($\alpha = 90°$) cases. This trend is explained by the momentum conservation while in most cases a smaller mass growth of the stream in Fig. 4.8 will lead to a smaller

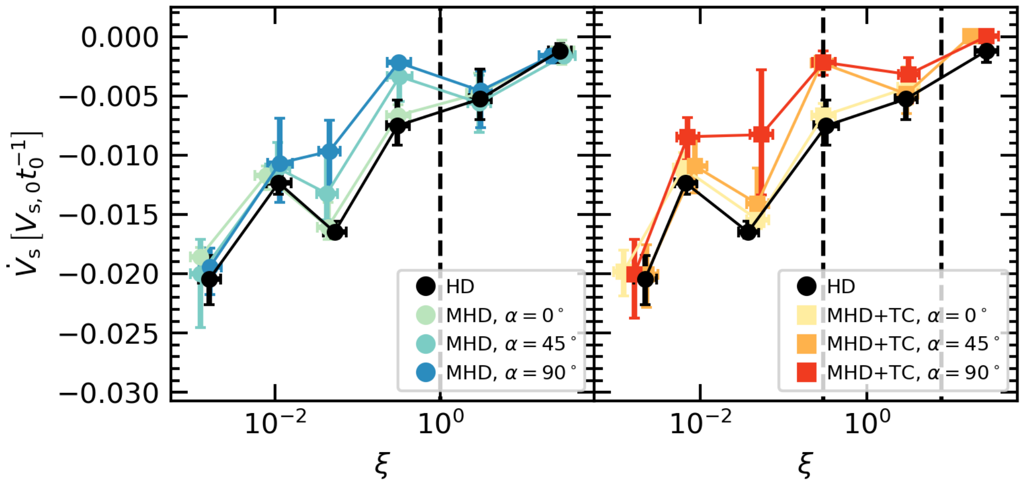

FIGURE 4.13: Stream deceleration in units of initial velocity per crossing time. *Left panel:* Comparison between HD and MHD simulations. The vertical dashed black line represents the limit between the *condensing stream* regime ($\xi < 1$) and the *disrupting stream* regime ($\xi > 1$). *Right panel:* Comparison between HD and MHD+TC simulations. The vetical black dashed lines represent the boundaries between the *condensing stream* regime ($\xi < 0.3$), the *intermediate* regime ($0.3 < \xi < 8$), and the *diffusing stream* regime ($\xi > 8$). Each point are an averaged value of the three Mach numbers $\mathcal{M} = 0.5, 1, 2$ for fixed $(n_{\rm s}, \delta, \alpha)$, with the error bars representing the range of minimum and maximum values. A small random offset in the x coordinate is included for clarity between the points.

deceleration. However, this explanation does not fully hold for increasing ξ as in this case the momentum is not only transfer to condensing CGM gas but is mostly due to stream mass loss and to the growth of turbulence.

4.2.4.2 Turbulence

As previously mentioned, the interaction between the CGM and the stream gas is crucial in shaping the distinctive emission signature of the cold stream. In this section, we employ a mean-field approach to evaluate the turbulent velocity within the mixing layer. Below, we outline the procedure for calculating the turbulent component of a specific fluid parameter. Firstly, the values averaged along the stream axis, and on both sides of the stream axis to yield to a radial-dependent average, as,

$$\overline{\rho}\,(r) = \frac{1}{L_{\rm y}} \int_0^{L_{\rm y}} 0.5\,(\rho(x,y) + \rho(-x,y))\;{\rm d}y. \tag{4.14}$$

Subsequently, we compute the density-weighted average of the given parameter, which average is suited for compressible flows (Favre, 1969),

$$\widetilde{X}\,(r) = \frac{\overline{\rho X}}{\overline{\rho}}. \tag{4.15}$$

.

The fluctuating field is obtained through the mean-field decomposition, where $X'(x,y) = X(x,y) - \widetilde{X}(|x|)$. Practically, the root-mean-square value of the fluctuating velocity field within the mixing layer is determined from the turbulent kinetic energy, as,

$$V'_{\rm ML} = \left(\frac{1}{r_{\rm ML}} \int \widetilde{u'^2} {\rm dr} \right)^{1/2}, \tag{4.16}$$

where here, $u'^2 = u_{\rm r}'^2 + u_{\rm y}'^2$, and the mixing layer is defined between the temperature thresholds $T_{\rm d}$ and $T_{\rm u}$ (refer to appendix B for an in-depth discussion on the thresholds). The mean size of the mixing layer, denoted as $r_{\rm ML}$, is defined as,

$$r_{\rm ML} = \frac{1}{L_{\rm y}} \int \left(0.5 \int_{\rm ML} {\rm dx} \right) {\rm dy}, \tag{4.17}$$

The factor 0.5 accounts for the averaging of the mixing layers on both sides of the stream. It's worth noting that the integral in Equation 4.16 is performed as a function of the radius r since the density-weighted averaged values in Equation 4.15 vary with r. Here, $r_{\rm ML}$ is the size of the mixing layer. It's important to emphasize that our definition of turbulent kinetic energy incorporates the mean radial velocity as part of the mean flow, accounting for the inflow velocity of CGM gas, denoted as $v_{\rm in}$, within the bulk motion (cf. Sec. 2.3.3), instead of being accounted in the turbulent velocity term.

The results are illustrated in Fig. 4.14 for all simulations, except the MHD+TC in the *diffusing stream* regime[6]. The trend in turbulent velocity is quite apparent, showing a consistent decrease as ξ increases. For $\xi < 1$, the overall decrease observed in HD simulations can be fitted as $V'_{\rm ML} \propto v_{\rm s,0}\xi^{-1/5}$. On the other hand, for $\xi > 1$, a relatively constant value around $0.11 v_{\rm s,0}$ emerges, exhibiting only a very weak dependence on ξ. This descending pattern aligns with the analytical model presented by Tan et al. (2021, equation 42, Figure 12), which was deduced from previous simulations focusing on cold-hot interface geometry. Their simulations also yielded the relationship $V'_{\rm ML} \propto v_{\rm s,0}\xi^{-1/5} \propto v_{\rm s,0}^{4/5} t_{\rm cool}^{-1/5}$.

In line with our earlier findings, the HD simulations consistently exhibit higher turbulent velocities in contrast to their MHD and MHD+TC counterparts. As previously observed, the presence of magnetic fields and thermal conduction inhibits the growth of the Kelvin-Helmholtz instability (KHI), particularly evident when $\alpha \neq 0°$, which directly translates to a reduction in turbulence within the mixing

[6]Concerning the MHD+TC simulations in the *diffusing stream* regime, thermal conduction effectively diffuses all instabilities, yielding a negligible turbulent velocity, specifically $V'_{\rm ML} < 10^{-2} v_{\rm s,0}$. To ensure clarity, we have opted to exclude these simulations from the plot.

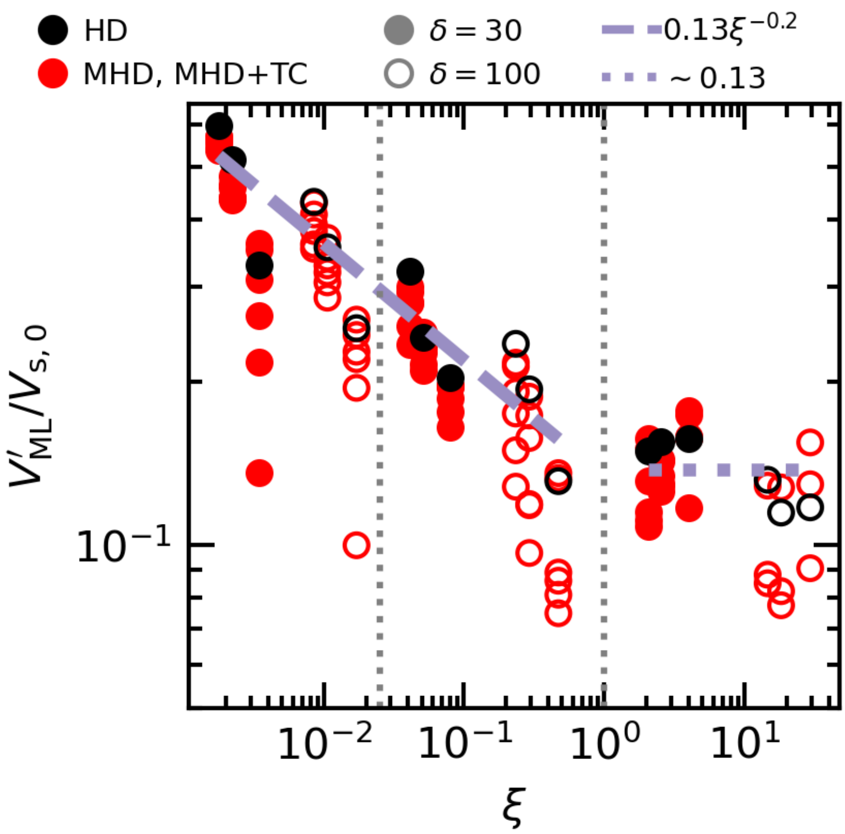

FIGURE 4.14: Turbulent velocity in the mixing layer. Black points red points refer to the HD simulations and the MHD and MHD+TC simulation, respectively. Fitted power-law relations are shown in purple for $\xi < 1$ and $\xi > 1$ by the purple dashed and dotted lines, respectively. The detailed distribution (grey dashed lines, filled and open circles) of the points is the same as in Fig. 4.4.

layer. Concerning the magnitude of turbulence, we find values quite similar to those reported in prior simulations of cold streams by Mandelker et al. (2019, without radiative cooling), where $V'_{\rm ML} \sim 0.2 v_{\rm s,0}$. However, our turbulent velocities surpass those observed in their simulations with radiative cooling (Mandelker et al., 2020a), which indicate $V'_{\rm ML} \sim 0.2 v_{\rm s,0} \delta^{-1/2} \sim 0.02 - 0.03 v_{\rm s,0}$. This discrepancy might be attributed to the distinct integration domains. In their case, they consider both the stream and the mixing layer, while we restrict our calculations exclusively to the region encompassed by the temperature thresholds of the mixing layer. When we include the stream in the integral domain defined in Equation 4.16, we find $V'_{\rm ML} \sim 0.6 v_{\rm s,0} \delta^{-1/2}$, which is smaller than our value within the mixing layer. Additionally, it's important to note that their simulations are three-dimensional, whereas ours are conducted in two dimensions. Therefore, we should anticipate some variation in the magnitude of turbulence between the two studies.

We find that the influence of MHD or MHD+TC on turbulence magnitude aligns with the evolution of stream mass. As the angle α approaches $90°$, there is a decrease on turbulence intensity. To quantify this, we applied a fitting approach akin to that used for the HD simulations in Fig. 4.14 to the MHD and MHD+TC simulations where $\alpha \neq 0°$. Simulations with $\alpha = 0°$ were excluded from the fitting process since their magnetic fields do not undergo significant amplification compared to HD simulations. The resultant fit yields:

$$V'_{\rm ML} \sim \begin{cases} 0.1\, v_{\rm s,0}\, \xi^{-1/4} & \text{if } \xi < 1, \\ 0.1\, v_{\rm s,0} & \text{if } 1 < \xi < 10. \end{cases} \tag{4.18}$$

The decrease in turbulence magnitude is evident from the fitting results. Both HD and the combined MHD and MHD+TC fits start at a similar turbulence intensity around $\xi \sim 10^{-2}$, with $V'_{\rm ML} \sim 0.6 v_{\rm s,0}$. However, the fitting curve for MHD and MHD+TC exhibits a steeper slope, resulting in a more pronounced decrease in turbulent velocity down to approximately $V'_{\rm ML} \sim 0.1 v_{\rm s,0}$. This sharper decrease in turbulent velocity highlights the direct influence of MHD and TC in suppressing the growth of the Kelvin-Helmholtz instability (KHI). In the presence of a magnetic field, the amplified field generates a tension force that opposes KHI growth, thereby stabilizing the stream. In the case of thermal conduction, the diffusion of either the mixing layer or the stream can further diminish KHI growth, leading to stream stabilization against KHI and reducing the mixing between the stream and the CGM.

Chapter 5

Discussion

5.1 Emissions in the halo

In Section 4.1, we explored the emission characteristics of a cold stream with a constant radius of $R_\mathrm{s} = 1, \mathrm{kpc}$ situated at the virial radius $R_\mathrm{v} = 100, \mathrm{kpc}$ of a massive galaxy residing within a $10^{12}, \mathrm{M}_\odot$ halo. As the stream perseveres and delves deeper into the halo, it undergoes an increase in density, resulting in a substantial boost in its emission by a factor of $10^2 - 10^3$ (Mandelker et al., 2020b).

In the *condensing stream* regime, marked by high density, and/or high metallicity, and/or an large R_s, the influence of magnetic fields and thermal conduction on the stream's emission remains minimal. However, within the *intermediate* or *diffusing stream* phases, where the stream exhibit low number density, and/or reduced metallicity, and/or a small radius, the presence of magnetic fields and thermal conduction leads to a siginificant reduction in the stream's emission, amounting to a factor of $10 - 20$.

Our analysis unveils that, on average, the hydrogen component contributes approximately 20%, with peak values reaching around 45% (as detailed in Sec. 4.2.1.2), to the emission from the stream. Considering that the cooling emission is predominantly collisional, it is reasonable to assume that the Lyα emission constitutes approximately 50% of the total hydrogen cooling rate (see figure 7 in Dijkstra, 2017). Consequently, for MHD+TC simulations (restricted to cases with $\alpha \neq 0^\circ$, which better reflect a realistic scenario than a purely parallel magnetic field configuration), the overall net emission originating from a cold stream in proximity to the galaxy (at approximately $0.1 R_\mathrm{v}$ from the halo centre) falls within the range of $L_\mathrm{net}\,(0.1 R_\mathrm{v}) = (100\text{–}1000) \times L_\mathrm{net}\,(1 R_\mathrm{v}) \sim 4 \times 10^{38}\text{–}10^{41}, \mathrm{erg}, \mathrm{s}^{-1}$ (with

$L_{\rm net}\,(1R_{\rm v}) \sim 4\times 10^{36}$–$10^{38}{\rm erg s^{-1}}$ for the *intermediate* and *diffusing stream* phases). Consequently, the ensuing Lyα emission in the vicinity of the galaxy is estimated as follows,

$$\begin{aligned} L_{\rm Ly\alpha} &= a_{\rm H} a_{\rm Ly\alpha} L_{\rm net}\,(0.1R_{\rm v}) \\ &\sim \begin{cases} 10^{38}\text{–}5\times 10^{41}\,{\rm erg\,s^{-1}} & \text{for } \xi < 0.3, \\ 4\times 10^{37}\text{–}2.5\times 10^{40}\,{\rm erg\,s^{-1}} & \text{for } \xi > 0.3, \end{cases} \end{aligned} \tag{5.1}$$

with here, $a_{\rm H} = 0.2$–0.45, representing the hydrogen contribution to the total net cooling emission, while $a_{\rm Ly\alpha} = 0.5$ accounts for the Lyα contribution to the hydrogen cooling emission. The two distinct scenarios, $\xi < 0.3$ and $\xi > 0.3$, correspond to the *condensing stream* phase and the *intermediate* and *diffusing stream* phases, respectively.

The emission emanating from the stream primarily originates from the cooling layer. As the stream's radius expands, so does the volume encompassed by the mixing layer surrounding the stream. Consequently, the net emission, denoted as $L_{\rm net}$, scales proportionally with $R_{\rm s}^2$, representing the cross-sectional area of the stream. For instance, when $R_{\rm s} = 10,{\rm kpc}$, this implies that $L_{\rm Ly\alpha}$ falls within the range of $\sim 4\times 10^{39}$–$2.5\times 10^{42}\,{\rm erg,s^{-1}}$ for a stream in the *intermediate* or *diffusing stream* phases, and of $\sim 10^{40}$–$5\times 10^{43}\,{\rm erg,s^{-1}}$ for a stream in the *condensing* regime. Here, we assume that the stream remains within the phase it occupied with $R_{\rm s} = 1,{\rm kpc}$.

Comparatively, in contrast to the analytical model developed by Mandelker et al. (2020b)[1], our MHD+TC simulations yield very similar results for dense and/or thick streams. However, they yield values that are lower by a factor of approximately 100 for diffuse and/or thin streams. This difference arises from both a reduced $L_{\rm net}$ and a decreased $a_{\rm H}$[2].

Prior investigations, such as those by Goerdt et al. (e.g., 2010), Mandelker et al. (e.g., 2020b), have frequently depicted galaxies being fed by two or three large cold streams. This conceptual framework aligns nicely with established cosmological simulations. However, recent simulations employing higher resolutions within galactic haloes (Hummels et al., 2019, Peeples et al., 2019, van de Voort et al., 2019, Bennett & Sijacki, 2020, Nelson et al., 2020) have unveiled the presence of numerous small-scale ($<1,{\rm kpc}$) cold structures within the CGM. These small-scale features

[1]This model is derived from earlier hydrodynamic simulations, such as those found in (e.g. Mandelker et al., 2020a), which bear similarities to our work.

[2]In their model, they ascribe roughly 50% of the emission to gas at a temperature of $T \sim (2\text{–}3)\,10^4{\rm K}$, which they associate with hydrogen emission. In our case, the hydrogen emission is directly calculated from the cooling model, leading to a lower percentage contribution.

become particularly conspicuous as resolution is increased near CGM shocks generated by galactic feedback processes (Bennett & Sijacki, 2020, see figure 5). Bennett & Sijacki (2020) even suggest that the CGM exhibit a "web-like" structure of cold matter, potentially boosting emissions by a factor of more than 10.

As a result, the cold flow signature woud not solely revolve around large filamentary structures; it could encompass emissions from a myriad of smaller, less dense streams. This implies that the overall cold flow emission can be increased, by over a factor of 10, owing to the potential contribution of numerous thin cold streams within the CGM. Consequently, the emission characteristics linked to cold flows are notably more diverse and intricate than previously believed, highlighting the necessity of fully accounting for the range of cold structures within the CGM.

5.2 Properties of the cold accretions

In our analysis, we concentrate on assessing the properties of a stream upon entry into a halo, specifically focusing on mass flux, metallicities, and magnetic field strength. The mean[3] cold mass inflow rate $j_{\rm s}$ is determined by the equation,

$$j_{\rm s} = \frac{1}{L_{\rm y}} \int \left(\iint \rho v_{\rm y} \, {\rm dA} \right) {\rm dy}, \tag{5.2}$$

where $L_{\rm y} = 32\,{\rm kpc}$ represents the length of the stream, dA denotes the cross-sectional area perpendicular to the stream axis, and the integration is restricted to gas categorized as cold with $T < T_{\rm d}$ (refer to Sec. 4.1). We express the mass flow rate in terms of the initial rate $j_{\rm s,0} = 0.01\text{–}1\,{\rm M}_\odot\,{\rm yr}^{-1}$, assuming a cylindrical stream.

We calculate the stream's metallicity as a function of its mass using the following formula,

$$Z_{\rm s,final} \sim \begin{cases} \frac{M_{\rm s,final} - M_{\rm s,0}}{M_{\rm s,final}} Z_{\rm cgm} + \frac{M_{\rm s,0}}{M_{\rm s,final}} Z_{\rm s} & \text{if } M_{\rm s,final} > M_{\rm s,0}, \\ Z_{\rm s} & \text{if } M_{\rm s,final} < M_{\rm s,0}. \end{cases} \tag{5.3}$$

The equation accounts for the scenario where if the stream gains mass, the additional cold mass has the metallicity of the surrounding CGM, while if the stream loses mass, the remaining cold mass retains its initial stream metallicity.

[3]Since our simulations encompass both stream and CGM properties at $R_{\rm v}$ across the entire computational domain, we perform mass flux averaging in the y-direction to eliminate dependence on the local cold mass rate.

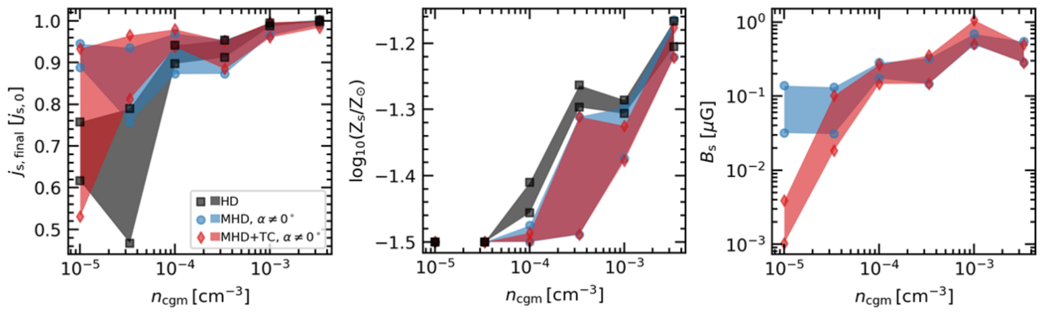

FIGURE 5.1: Properties of the stream penetrating the halo plotted as a function of the CGM number density. *Left panel*: Cold mass accretion rate at the simulation final time in units of initial cold accretion rate, $j_{\mathrm{s},0} = m_{\mathrm{p}}\mu n_{\mathrm{s}}\mathcal{M}c_{\mathrm{cgm}}\pi R_{\mathrm{s}}^2 \sim 0.01\text{–}1\,\mathrm{M}_\odot\,yr^{-1}$ for $R_{\mathrm{s}} = 1\,\mathrm{kpc}$ and $n_{\mathrm{s}} = 0.001\text{–}0.1\,\mathrm{cm}^{-3}$. *Middle panel*: Logarithm of the average metallicity in the stream at the final time in unit of Solar metallicity. The stream metallicity is initially $\log_{10}(Z_{\mathrm{s},0}/\mathrm{Z}_\odot) = -1.5$, and the initial CGM metallicity is $\log_{10}(Z_{\mathrm{cgm},0}/\mathrm{Z}_\odot) = -1$. *Right panel*: Mean magnetic field strength in the stream (B_{s}). This average value B_{s} is attained early in the simulations at a time $t \sim 0.1t_{\mathrm{end}}$ and then remain roughly constant.

Furthermore, we determine the mean magnetic field using the methodology outlined in Equation 4.10, and the outcomes are presented in physical units at the final simulation time.

Fig. 5.1 illustrates the stream properties as a function of the CGM number density, denoted as $n_{\mathrm{cgm}} = n_{\mathrm{s}}\delta^{-1}$, which scales approximately as $\xi^{-0.5}$. A higher density corresponds to more pronounced cooling emission and smaller ξ ratios, while the opposite is true for lower densities. For the MHD and MHD+TC simulations, we display results exclusively for cases with $\alpha \neq 0°$, as there are no significant deviations from the HD simulations when $\alpha = 0°$. In the left panel, we observe the tangible impact of MHD on the cold mass accretion rate, where it effectively retains approximately 80% of the initial mass flow in the low-density regime. This highlights how the presence of a magnetic field reinforces the stability of the stream, ensuring the persistence of cold mass accretion.

Thermal conduction comes into play primarily in scenarios with very low density, typically when $n_{\mathrm{cgm}} \sim 10^{-5}\,\mathrm{cm}^{-3}$, leading to stream diffusion and resulting in a decreased cold mass accretion rate of approximately $0.5j_{\mathrm{s},0}$. Nevertheless, as conduction efficiency diminishes with increasing velocity, the stream manages to maintain a cold mass accretion rate at roughly 90% of its initial value at low densities for $\mathcal{M} = 2$. Consequently, when compared to HD simulations, MHD+TC simulations exhibit no substantial differences in a high-density CGM with $n_{\mathrm{cgm}} \gtrsim 2 \times 10^{-4}\,\mathrm{cm}^{-3}$, but thermal conduction aids in sustaining the stream below this density threshold. Our results align with simulations involving cold clouds within galactic winds conducted in MHD simulations by Hidalgo-Pineda et al. (2023) and MHD+TC simulations by

Brüggen & Scannapieco (2023), as well as cosmological simulations with enhanced resolutions (Hummels et al., 2019, Nelson et al., 2020, Bennett & Sijacki, 2020).

The metallicity plot reveals that as CGM density, and subsequently cooling strength, increases, the stream's metallicity also rises, reaching up to approximately 60% of the difference between the final stream metallicity, $Z_{\mathrm{s,final}}$, and its initial value, Z_{s}, relative to the difference between CGM metallicity, Z_{cgm}, and stream metallicity, Z_{s}. Interestingly, both MHD and MHD+TC simulations exhibit a reduction in the metal enrichment of the stream by minimizing gas mixing. This phenomenon contradicts the conventional notion of cold streams as pristine, and it provides support for the observed (Bouché et al., 2013, 2016) or inferred (Giavalisco et al., 2011, Rubin et al., 2012, Martin et al., 2012, Zabl et al., 2019, Emonts et al., 2023, Zhang et al., 2023) high metallicity of cold inflows. Furthermore, from a cosmological simulation perspective, a higher metal-enriched cold inflow would lead to higher star-formation efficiency. Coupled with the prolonged stability of cold streams in the hot CGM, this suggests the potential for extended periods of star formation in massive galaxies.

In high-density CGM environments, the magnetic field within the stream can experience substantial amplification, reaching approximately 1 μG. Conversely, as the CGM density decreases, the magnetic field strength diminishes, dropping to around 2×10^{-2} μG in the case of MHD simulations.

However, for MHD+TC simulations with $n_{\mathrm{cgm}} \sim 10^{-5}\,\mathrm{cm}^{-3}$, the magnetic field within the cold stream remains relatively stable as the stream gradually diffuses.

From the perspective of cosmological simulations, one might anticipate the magnetic field to undergo further amplification upon compression once it enters the ISM. Such magnetized cold inflow could potentially takes longer time to collapse due to magnetic support.

The straightforward extrapolation of our findings raises intriguing questions about potential limitations in cosmological simulations stemming from their resolution constraints. Beyond the extended persistence of cold stream inflow, there is a significant transformation in the nature of the cold material itself. It evolves from being pristine cold streams to becoming metal-enriched, magnetized cold streams.

5.3 Caveats: 2D vs. 3D and additional physics

One primary limitation of our study lies in the two-dimensional nature of our simulations. In a three-dimensional context, the Kelvin-Helmholtz instability (KHI) is expected to evolve more rapidly due to the presence of additional instability modes. This accelerated growth results in a more effective mixing process between the stream and its surrounding medium, consequently influencing the evolution of the stream and its observable characteristics (Padnos et al., 2018, Mandelker et al., 2019). This enhanced mixing could potentially lead to increased emission and mass growth rates for streams in the "condensing stream" regime ($\xi = t_{\rm cool}/t_{\rm sh} < 1$). In previous MHD simulations featuring magnetic fields aligned with the stream, Berlok & Pfrommer (2019b) observed that three-dimensional simulations exhibited amplified mixing. This enhancement primarily arises from the growth of azimuthal KHI modes, which are not impeded by any magnetic tension force when the magnetic field is parallel to the stream. In future investigations, we intend to explore the impact of magnetic fields that are not aligned with the stream by performing three-dimensional simulations.

Furthermore, a more comprehensive model should incorporate additional physics. For instance, our current model overlooks self-gravity, which could potentially impact the stability of the stream (Aung et al., 2019). Additionally, we utilize a cooling-heating function (as illustrated in Fig. 2.2) with the presumption that the gas behaves as optically thin. Nevertheless, this function should be adaptable to the stream's density since dense cold streams are capable of self-shielding against the UV background radiation. Considering that both gas temperature and density play pivotal roles in determining the significance of self-gravity within the stream (refer to Ostriker, 1964, Aung et al., 2019), it becomes evident that a meticulous treatment of radiation heating is essential for assessing the stability of the cold stream. However, we suggest that self-shielding may not influence on the emission originating from the mixing layer, as it is predominantly governed by collisional cooling.

Chapter 6

Conclusions and future plans

Recent progress from high-resolution idealized simulations has significantly advanced our understanding of cold streams and their associated emission signatures. To further increase this understanding, we undertook an extensive suite of two-dimensional simulations that took into account critical physical mechanisms, namely radiative cooling, magnetic fields with varying orientations, and anisotropic thermal conduction. This thesis work represent the first exploration of the fate of cold streams with the combination of all these physical processes. The simulations were executed employing the Athena++ code, without considering self-gravity or self-shielding.

Our idealized simulations consider a cold stream located at the virial radius of a halo with a mass of $10^{12}\,\mathrm{M}_{\odot}$ at a redshift of $z = 2$. We defined the stream with a relatively small radius of $R_{\mathrm{s}} = 1\,\mathrm{kpc}$ with a weak magnetic field characterized by the ratio of thermal pressure to magnetic pressure denoted as $\beta = 10^5$. Our main findings are presented by the illustration in Fig. 6.1.

Cold Streams Regimes: Considering thermal conduction, the behavior of the stream can be classified into three regimes (see Sec. 2.5), determined by the $\xi = t_{\mathrm{cool}}/t_{\mathrm{sh}}$ ratio, where t_{cool} represents the cooling time defined from the mixing layer (Equation 2.6) and t_{sh} denotes the shearing time (Equation 2.29).

(1) The *diffusing Stream* regime ($\xi > 8$) corresponds to the thinnest and/or most diffuse cold streams, as depicted in Fig. 6.1. In this regime, thermal conduction dominates over other processes, inhibiting Kelvin-Helmholtz Instabilities (KHI) growth and causing the stream to diffuse within the circumgalactic medium (CGM). However, a faster stream can significantly reduce the efficiency of thermal conduction while still stabilizing it against KHI, potentially allowing it to reach the central galaxy.

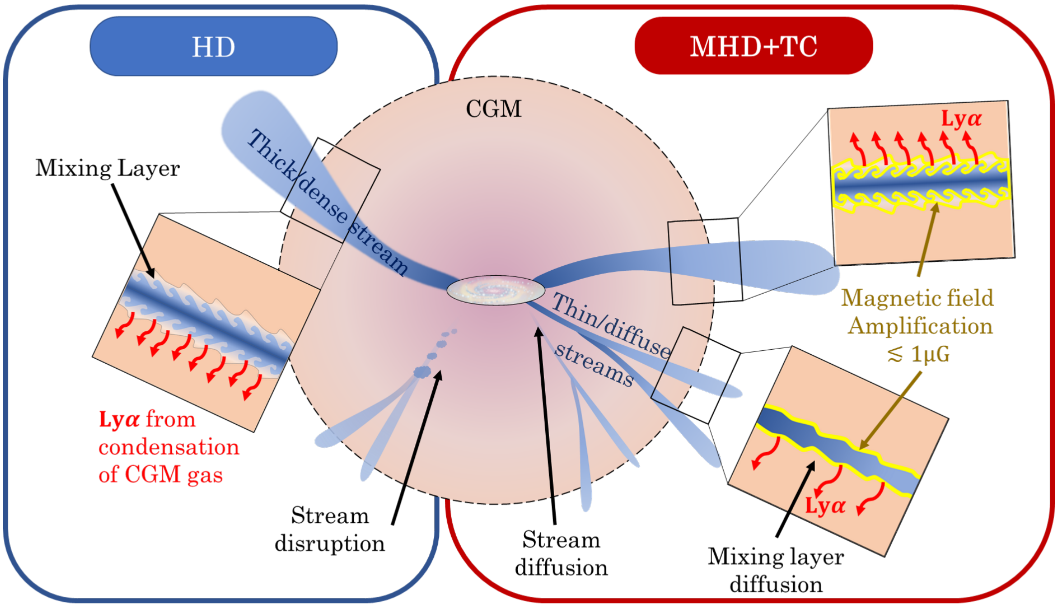

FIGURE 6.1: Summary illustration which compares the fate of cold streams for the hydrodynamic (HD) case and the magnetohydrodynamic with thermal conduction (MHD+TC) case. In the HD case, dense or thick streams survive (*condensing stream* regime) while diffuse or thin streams disrupt within the CGM due to the growth of KHI (*disrupting stream* regime). In both cases, Lyα emissions originates from the mixing layer. In the MHD+TC case, dense or thick streams survive, but providing magnetized cold material to the galaxy (*condensing stream* regime). For diffuse or diffuse streams, the amplification of magnetic field and the diffusion of the mixing layer by the thermal conduction stabilize the stream against Kelvin-Helmholtz instability (KHI), but resulting in significantly less Lyα emissions (*intermediate* regime). If the stream is too diffuse or thin, it may evaporate in the CGM, potentially stopping its fall towards the central galaxy (*diffusing stream* regime).

(2) In the *intermediate* regime ($8 > \xi > 0.3$), radiative cooling can overcome thermal conduction within the stream but not in the mixing layer. This leads to diffusion of the mixing layer and all cold substructures inside it.

(3) The *condensing Stream* regime ($\xi < 0.3$) relates to dense and/or thick cold streams, as illustrated in Fig. 6.1. In this scenario, cooling operates with high efficiency, resulting in the condensation of CGM gas onto the stream. A crucial distinction from the hydrodynamic version of the *condensing Stream* regime is that the stream becomes magnetized upon reaching the central galaxy.

Emission Signature: In the *intermediate* and *diffusing Stream* regimes, the MHD+TC case exhibits a substantial reduction in the emission signature compared to the HD case, by a factor of up to 20 (see Sec. 4.2.1). This decrease in emission can be attributed to two factors: the enhancement of the magnetic field at the stream interface and the diffusion of the mixing layer which represent the source of the cooling emissions. In the *diffusing Stream* regime, the emitting gas becomes hotter, leading to an increase in metals emissions but a decrease in hydrogen emissions. In the *condensing Stream* regime, the impact of thermal conduction and magnetic fields on the stream's emission is relatively minor. We observed that, in all regimes but the *diffusing Stream* regime, approximately 20% of the stream's cooling emission originates from hydrogen, which is lower than previous estimates found in the literature. This further diminishes the expected Lyα luminosity of cold streams.

Cold Stream Evolution: In the *intermediate* regime, magnetic fields and thermal conduction effectively hinder KHI growth (see Sec. 4.2.3 and 4.2.4). Consequently, the stream remains stable without experiencing mass loss, enabling it to survive longer compared to the hydrodynamic case (Sec. 4.1).

In the *diffusing Stream* regime, even though mass loss occurs, the efficiency of thermal conduction drop notably with increasing stream velocity. Consequently, streams with a Mach number $\mathcal{M} = 2$ experience only minimal mass loss and as the KHI are completely inhibited, the stream can actually survives longer than in the HD cases.

It's noteworthy that, similar to the emission signature, the presence of magnetic fields and thermal conduction does not significantly affects the stream's evolution in the *condensing Stream* regime and int he other regimes when the magnetic field is parallel to the stream ($\alpha = 0°$).

Cosmological Implications: Extrapolating our idealized simulation findings to a cosmological context (see Chapter 5), we have determined that Lyα luminosities of cold streams within halos range from $4 \times 10^{37}\,\mathrm{erg\,s^{-1}}$ to $5 \times 10^{41}\,\mathrm{erg\,s^{-1}}$. This range is specific to relatively small cold streams with a radius of $R_\mathrm{s} = 1\,\mathrm{kpc}$. Moreover, we observed that inflowing gas in these streams becomes enriched with metals and magnetized, with the mean magnetic field strength in the stream reaching approximately $1\,\mu\mathrm{G}$. These results provide insights into the properties and characteristics of cold streams in a cosmological context.

Appendix A

Resolution test

We perform a convergence analysis of our simulations, concentrating on a density ratio $\delta = 100$, a Mach number $\mathcal{M} = 1$, and a magnetic field angle $\alpha = 45°$. For both the pure MHD and MHD with TC (thermal conduction) cases, we vary the number density as $n_{\rm s} = \{0.001, 0.01, 0.1\}\,{\rm cm}^{-3}$, and the corresponding ξ values can be found in Table A.1.

We employ grids with minimal resolution $\Delta_{\rm min}/R_{\rm s} = \{1/32, 1/16, 1/8, 1/4\}$. Due to the use of static mesh refinement, each simulation uses one fewer refinement level, resulting in a stream region resolution that is twice as coarse. Furthermore, as detailed in Section 3.2, we apply smoothing to the interface using $h = R_{\rm s}/32$, which determines the penetration depth of the perturbations in Equation 3.8. To ensure that the penetration depth remains greater than the minimum mesh size, the parameter h is scaled by a factor of two between each grid enlargement.

Figure A.1 illustrates the temporal evolution of the stream mass. Each panel displays the fiducial (finest grid) and coarser grid cases, depicted using a dark-to-pale color scale, respectively. The convergence quality varies across different regimes.

In the *condensing stream* regime ($\xi \ll 1$), results show good agreement starting from $\Delta_{\rm min} = R_{\rm s}/8$. However, in other regimes, qualitative convergence is not yet achieved at $\Delta_{\rm min} = R_{\rm s}/32$.

It's worth noting that scaling the parameter h also enlarges the size of the smoothing region. In the case of the *diffusing stream* regime, this enlargement leads to a modification in the initial temperature gradient, resulting in a slight impact on stream diffusion. This explains the minor discontinuity in convergence. Starting from $\Delta_{\rm min} = R_{\rm s}/4$ to $\Delta_{\rm min} = R_{\rm s}/32$, results begin converging. However, between

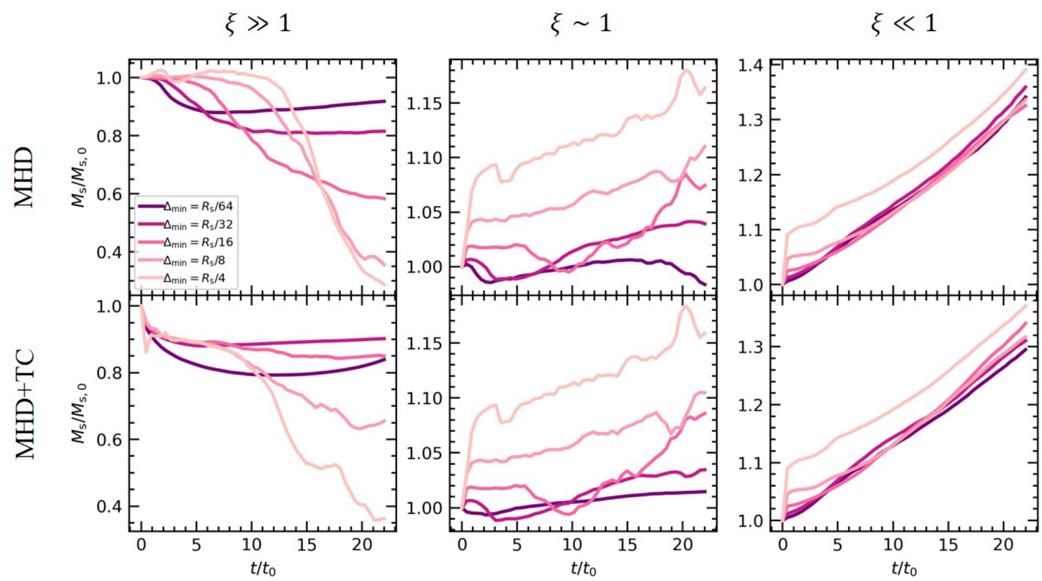

Figure A.1: Results of the convergence tests are presented. The top panels show the mass evolution of the stream in units of the initial stream mass as a function of time for different ξ values in the MHD cases, while the bottom rows depict the same for the MHD+TC cases.

$\Delta_{\mathrm{min}} = R_{\mathrm{s}}/32$ and $\Delta_{\mathrm{min}} = R_{\mathrm{s}}/64$, the difference between solutions suddenly increases. To further investigate this effect, we conducted simulations without scaling the parameter h.

To evaluate the quantitative convergence, we introduce the time-averaged relative error of a given quantity, denoted as X, defined as follows,

$$\epsilon_{\mathrm{i}} = \left\langle \frac{X_{\mathrm{i}} - X_0}{X_0} \right\rangle, \tag{A.1}$$

where the subscript i represents the coarsening factor of the simulation, defined for $i = 0, 1, 2, 3, 4$, such that $\Delta_{\mathrm{min}}\,(i)\,/R_{\mathrm{s}} = (1/64) \times 2^i$. The brackets indicate arithmetic-linear time averaging over all simulation snapshots. This relative error is computed based on the fiducial value X_0 obtained from the finest resolution simulation.

The time-averaged relative error, expressed as a percentage of the fiducial value (finest grid case), is provided in Table A.1 for the stream mass.

In all cases and considering the no-scaling case for the MHD+TC simulation in the *diffusing stream* regime ($\xi = 10^{1.3}$), the mean error decreases with rising resolution, peaking at around $\sim 7\%$ for $\Delta_{\mathrm{min}} = R_{\mathrm{s}}/32$.

TABLE A.1: Convergence test simulations and relative error of stream mass as a percentage of the fiducial value (finest grid case). The last row presents the MHD+TC simulation in the *diffusing stream* regime with the scaling of h removed, showing significantly improved convergence.

Simulation	ξ	ϵ_1 [%]	ϵ_2 [%]	ϵ_3 [%]	ϵ_4 [%]
MHD	$10^{-2.0}$	0.9	0.6	0.8	5.3
MHD+TC	$10^{-2.0}$	1.0	1.3	1.4	6.1
MHD	$10^{-0.5}$	1.8	2.9	6.6	11.7
MHD+TC	$10^{-0.5}$	1.1	2.3	5.6	10.8
MHD	$10^{1.3}$	6.7	17.5	20.6	22.5
MHD+TC	$10^{1.3}$	9.0	6.5	9.5	20.3
No scaling :					
MHD+TC	$10^{1.3}$	0.5	0.6	3.4	3.4

The purely MHD simulation in the *disrupting stream* regime ($\xi \sim 10^{1.3}$) exhibits relatively high error percentages at $\Delta_{\rm min} = R_{\rm s}/32$. For all other simulations, errors remain below a few percent, indicating good convergence.

Significant differences appear in the results obtained with and without scaling of the parameter h (corresponding to the last two rows in the table). In this specific case, eliminating the scaling of h results in the best convergence. This finding confirms that the broadening of the smooth interface between the stream and the CGM is responsible for the discrepancies observed in Fig. A.1.

In summary, our analysis suggests that all simulations, except for the MHD simulations in the *disrupting stream* regime ($\xi \gg 1$), exhibit good convergence, with relative errors below a few percent. In the case of the MHD simulations in the *disrupting stream* regime, the ongoing lack of full convergence may affect the quantitative conclusions by approximately 7% for this specific scenario.

Appendix B

Temperature thresholds

We have verified the suitability of the temperature thresholds introduced in Chapter 4 for the calculation of stream mass variables and mixing layer variables.

In Fig. B.1, we present the total gas mass within a specific temperature range T for HD, MHD, and MHD+TC simulations at $\mathcal{M} = 1$ across two density ratios, $\delta = \rho_{\rm s}/\rho_{\rm cgm} = 100$ and 30. In each panel, we display the thresholds $T_{\rm l} = (T_{\rm s}T_{\rm mix})^{1/2}$, $T_{\rm mix}$, and $T_{\rm u} = (T_{\rm cgm} + T_{\rm mix})/2$. Furthermore, we include the relative error defined as:

$$\epsilon\left(T\right) = \left\|\frac{M_{\rm s}\left(T\right) - M_{\rm s}\left(T_{\rm l}\right)}{M_{\rm s}\left(T_{\rm l}\right)}\right\|, \tag{B.1}$$

beneath each panel. In all curves, it is evident that we can distinguish the mass within the stream, the mixing layer, and the CGM. The initial rise in mass just after T_s corresponds to the stream gas, while the relatively constant phase represents the gas in the mixing layer. The final increase around $T_{\rm cgm} = \delta T_{\rm s}$ originates from the CGM gas. The threshold mass $M_{\rm s}\left(T_{\rm l}\right)$ appears to be suitable, as variations of the threshold to temperatures $2T_{\rm s}$ or $3T_{\rm s}$ result in only marginal changes in mass. The same argument applies to the threshold $T_{\rm u}$. The only drawback is that this threshold may introduce a systematic error by potentially misidentifying mixing layer gas as stream gas. Nevertheless, this error seems relatively minor and, being systematic, would not significantly alter our qualitative results.

Finally, insights can be drawn from Fig. B regarding the discussed physical differences in Chapter 4. The simulations with $\delta = 30$ reside within the "condensing stream" regime, thus exhibiting similar results across the HD, MHD, and MHD+TC cases. Conversely, for $\delta = 100$, the simulations find themselves in either the *intermediate* regime (MHD+TC) or the *condensing stream* regime (HD and MHD). The impact of thermal conduction is directly observable; in the MHD+TC simulations,

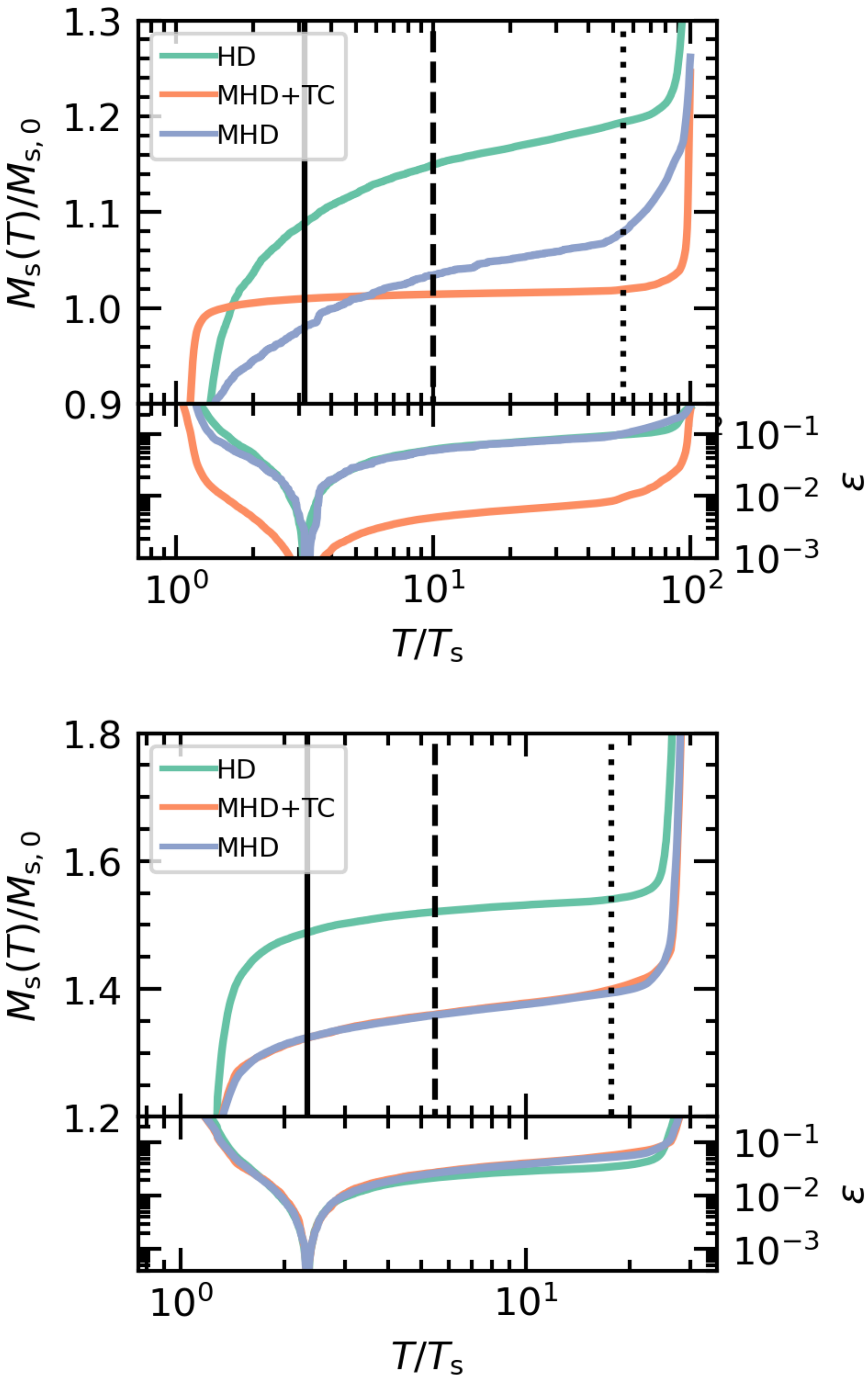

FIGURE B.1: Verification of the temperature thresholds. The mass within the entire simulation domain, enclosed within specific temperature limits, is plotted against temperature (upper subplot). The lower curves depict the relative error between our stream mass and the mass calculated using the provided temperature thresholds. (Top) HD, MHD, and MHD+TC simulations for $\delta = 100$. (Bottom) HD, MHD, and MHD+TC simulations for $\delta = 30$. In both panels, our selected stream temperature thresholds T_{l} and T_{mix}, along with our CGM temperature threshold T_{u}, are represented by solid, dashed, and dotted black lines. The relative error concerning the mass $M_{\mathrm{s}}(T)$ is displayed below each panel.

the mixing layer phase is entirely flattened, indicating the absence of gas in this phase due to its diffusion. This, in turn, leads to a reduction in cooling emission, as illustrated in Fig. 4.6.

Appendix C

Photo-chemistry Matlab code

```
clear all, close all
global A1s A2s A3s A4s G1s G2s G3s J1s J2s J3s ys nhs;
%% Constant parameters:
eV2erg = 1.602*1e-12;    % erg
h = 6.6261*1e-27;        % erg.s^-1
nu_H  = 13.62/h*eV2erg;
nu_He = 24.60/h*eV2erg;
nu_Hep= 54.40/h*eV2erg;

%Integration constant for heating rate and photoionization
    rate
Ca1=4*pi*(1e-22)/h; Ca2=4*pi*(1e-22)*nu_H; Ca3=4*pi*(1e
   -22)*nu_Hep; Bh=6.3*(1e-18);

% Primordial composition
X = 0.76; Y = 1-X;
y = Y/(4-4*Y); ys=y;
nh = 2.89*1e-6; nhs = nh; nhe = y*nh;

x = nh / (6.63*1e-3);
sh = (0.98*((1+(x.^1.64)).^-2.28) + 0.02*((1+x).^-0.84));

% Background radiation intensity
J1 = 0;% 0.267683*Ca1*Bh;         % from integral Thoul et
    al. (1998) //  9.44*1e-13*sh Haardt & Madau (2012) %
   integral = 3.2*(1e-13)  Photoionization  rate (eq.29)
```

```
J2 = 0;% J1/4;                    % from integral Thoul et al. (1998) // 5.57*(1e-13)*sh Haardt & Madau (2012)
J3 = 0;% 1.28*(1e-14);            % Haardt & Madau (2012)
J1s =J1; J2s=J2;J3s=J3;
Huvbh0  = Ca2*Bh*0.0949837;       % from integral Thoul et al. (1998) // 3.74*1e-12*eV2erg*sh  Haardt & Madau (2012) % integral = 9.44*1e-13 heating rate erg.s^-1 Photoionization heating rate (eq.40)
Huvbhe0 = Ca3*Bh*0.0949837/4;     % from integral Thoul et al. (1998) //4.44*(1e-12)*eV2erg*sh Haardt & Madau (2012)
Huvbhep = 2.44*(1e-13)*eV2erg;    % Haardt & Madau (2012)


%% Calculus
eT = 3.6:0.05:8.5; T = 10.^eT;                  % Temperature range
G1 = 5.85*(1e-11).*(T.^0.5)./(1+sqrt(T/1e5)).*exp(-157809.1./T); % H+   Collisional ionization rates cm^3.s^-1
G2 = 2.38*(1e-11).*(T.^0.5)./(1+sqrt(T/1e5)).*exp(-285335.4./T); % He+  Collisional ionization rates cm^3.s^-1
G3 = 5.68*(1e-12).*(T.^0.5)./(1+sqrt(T/1e5)).*exp(-631515./T);   % He++ Collisional ionization rates cm^3.s^-1

A1 = 8.40*(1e-11)./(T.^0.5)./((T/1e3).^0.2)./(1+(T/1e6).^0.7);  % H+   Recombination rates cm^3.s^-1
A2 = 1.5*(1e-10)./(T.^0.6353);
        % He+  Recombination rates cm^3.s^-1
A3 = 1.9*(1e-3)./(T.^1.5).*exp(-470000./T).*(1+0.3.*exp(-94000./T));   % Recombination rates cm^3.s^-1
A4 = 3.36*(1e-10)./(T.^0.5)./((T/1e3).^0.2)./(1+(T/1e6).^0.7);  % He++ Recombination rates cm^3.s^-1

nh0 = T./T;
nhe0 = nh0; nhep = nh0; nhepp = nh0; ne = nh0;
fun = @HHeSys_noUVB;
```

```
% fun = @HHeSys; if UVB
nhp = nh - nh0;
for i=1:length(T)
    %A1s=A1(i)*ne(i)*nhp(i); A2s=A2(i); A3s=A3(i); A4s=A4(
   i)*ne(i)*nhepp(i); G1s=G1(i); G2s=G2(i); G3s=G3(i);
    A1s=A1(i); A2s=A2(i); A3s=A3(i); A4s=A4(i); G1s=G1(i);
    G2s=G2(i); G3s=G3(i);
    X0=[nh,y*nh,0.1,0.1,nh];
    X0 = fsolve(fun,X0);
    nh0(i) = X0(1);
    nhe0(i) = X0(2);
    nhep(i) = X0(3);
    nhepp(i) = X0(4);
    ne(i) = X0(5);
    nhp(i) = max(nh - nh0(i),0);
end
nhp = nh - nh0;


% Collisional excitation cooling :
Lceh0 = 7.5*(1e-19).*exp(-118348./T)./(1+sqrt(T/(1e5))).*
   ne.*nh0/(nh^2);
Lcehep= 5.54*(1e-17).*(T.^(-0.397)).*exp(-473638./T)./(1+
   sqrt(T/(1e5))).*ne.*nhep/(nh^2);
% Lcehep= Lcehep + 59.1*(1e-27).*(T.^(-0.1687)).*exp
   (-13179./T)./(1+sqrt(T/(1e5))).*ne.*ne.*nhep/(nh^2);
% Collisional ionization cooling :
Lcih0 = 1.27*(1e-21).*sqrt(T).*exp(-157809./T)./(1+sqrt(T
   /(1e5))).*ne.*nh0/(nh^2);
Lcihe0 = 9.38*(1e-22).*sqrt(T).*exp(-285335.4./T)./(1+sqrt
   (T/(1e5))).*ne.*nhe0/(nh^2);
Lcihep = 4.95*(1e-22).*sqrt(T).*exp(-631515./T)./(1+sqrt(T
   /(1e5))).*ne.*nhep/(nh^2);
% Lcihep = Lcihep + 5.01*(1e-27).*(T.^(-0.1687)).*exp
   (-55338./T)./(1+sqrt(T/(1e5))).*ne.*ne.*nhep/(nh^2);
% Recombination cooling :
Lrchp = 8.7*(1e-27).*sqrt(T)./((T/1e3).^0.2)./(1+((T/(1e6)
   ).^0.7)).*ne.*nhp/(nh^2);
Lrchep = 1.55*(1e-26).*(T.^(0.3647)).*ne.*nhep/(nh^2);
```

```
Lrchepp = 3.48*(1e-26).*sqrt(T)./((T/1e3).^0.2)./(1+((T/(1
   e6)).^0.7)).*ne.*nhepp/(nh^2);
% Dielectric recombination :
Ldhep = 1.24*(1e-13)./(T.^1.5).*exp(-470000./T).*(1+0.3.*
   exp(-94000./T)).*ne.*nhep/(nh^2);
% Free-free emission cooling cooling :
Lff = 1.42*(1e-27).*sqrt(T).*(1.1+0.34*exp( -((5.5-log10(T
   )).^2)/3 )).*ne.*(nhp+nhep+4*nhepp)/(nh^2);
% Inverse Compton cooling :
Lcmp = 5.41*(1e-36)*(T/1e4)*((1+2)^4).*ne/(nh^2);
% Total cooling rate
Lcool = (Lceh0 + Lcehep + Lcih0 + Lcihe0 + Lcihep + Lrchp
   + Lrchep + Lrchepp + Lff + Ldhep + Lcmp);

% Heating rates:
Hh0 = nh0*Huvbh0/(nh^2);
Hhe0 = nhe0*Huvbhe0/(nh^2);
Hhep = nhep*Huvbhep/(nh^2);
Lnet = Hh0 + Hhe0 + Hhep - Lcool;

T = log10(T);

fg=figure(1)
    axis_handle = axes;
    set(0,'DefaultTextInterpreter','Latex');
    set(groot,'DefaultAxesTickLabelInterpreter','Latex');
    set(groot, 'defaultLegendInterpreter','latex');
    plot(T,log10(Lcool),'k','LineWidth',3.0);hold on
    plot(T,log10(Lceh0),'b-.','LineWidth',2.0);
    plot(T,log10(Lcehep),'c-.','LineWidth',2.0);
    plot(T,log10(Lcih0),'b:','LineWidth',2.0);
    plot(T,log10(Lcihe0),'c:','LineWidth',2.0);
    plot(T,log10(Lcihep),'m:','LineWidth',2.0);
    plot(T,log10(Lrchp),'b--','LineWidth',2.0);
    plot(T,log10(Lrchep),'c--','LineWidth',2.0);
    plot(T,log10(Lrchepp),'m--','LineWidth',2.0);
    plot(T,log10(Ldhep),'m--','LineWidth',2.0);
    plot(T,log10(Lff),'k--','LineWidth',2.0);
    % plot(T,log10(Lcmp),'k-.','LineWidth',2.0);
```

```
    xmin = 3.55;
    xmax = 8.2;
    ymin = -25
    ymax = -21.55;
    axis([xmin xmax ymin ymax]);
    hold off;

    set(axis_handle,'LineWidth',2,'FontName','Latex','
   FontSize',18,'FontWeight','Bold');
    xlabel('$\log_{10} \left(T\right)$ $[\rm{K}]$','
   Interpreter','latex','FontSize',22);
    ylabel('$\log_{10}\left(\Lambda / n_{\rm{H}^2}\right)$
    $[\rm{erg \, s^{-1} \, cm^{3}}]$','Interpreter','latex
   ','FontSize',22);
%     legend('total','$\vert$ Net Cooling $\vert$','
   Location','northeast','interpreter','Latex','FontSize
   ',20)
    hold off
%     title('$log \vert \mathcal{H}-\Lambda\vert / n_{\rm{
   H}^2}$ $\rm{erg \, s^{-1} \, cm^{3}}$','Interpreter','
   latex','FontSize',23);
    file_name = strcat('./fig1_Katz.png');
    set(gcf, 'Units','centimeters', 'Position',[0 0 15
   15])
        print(file_name,'-dpng','-r200');
%  delete(fg);
```

Listing C.1: Main Matlab code to solve and plot the cooling curves

```
function F = HHeSys_noUVB(X)
global nhs A1s A2s A3s A4s G1s G2s G3s ys;
nh0 = X(1);
nhe0 = X(2);
nhep =X(3);
nhepp = X(4);
ne = X(5);

eq = 1:5;
eq(1) = nh0 - nhs*A1s / (A1s + G1s);
```

```
% eq(2) = nhep - ys*nhs / (1 + (A2s+A3s)/(G2s) + (G3s)/A4s
   );
eq(2) = nhep - nhe0*G1s/(A2s+A3s);
% eq(3) = nhe0 - nhep*(A2s+A3s)/(G1s);
eq(3) = nhepp - nhep*G3s/A4s;
% eq(4) = nhepp - nhep*(G3s)/A4s;
eq(4) = nhe0 - ys*nhs + nhep + nhepp;
eq(5) = ne - (nhs - nh0) - nhep - 2*nhepp;

F = eq;
end
```

Listing C.2: Main Matlab code to solve and plot the cooling curves

Appendix D

CLOUDY input file

```
title map of heating vs cooling
#
# commands controlling continuum =========
background, redshift= 2.0
table hm12 z = 2.0
#
# commands for density & abundances =========
hden -5 log
constant temper 1e3 vary
grid 3 7 0.02
#abundances old solar 84
#element abundance helium -0.5006
#abundances all -0.5006
metals =0.0316227766
#
# commands controlling geometry  =========
set dr 0
stop zone 1
iterate to convergence
#
# other commands for details     =========
#
# commands controlling output    =========
# save map information to generate plot for hazy
save cooling each file="d-5.dta"  #range 1 3 7 no hash
#set nmaps 200
# CGM_Z015.in
# class function
# =======================================
#
```

LISTING D.1: CLOUDY input file to generate the net cooling rate table in function of temperature at a given density.

Bibliography

Abel T., Bryan G. L., Norman M. L., 2002, Science, 295, 93

Agertz O., Teyssier R., Moore B., 2009, MNRAS, 397, 64

Anderson L., et al., 2014, MNRAS, 441, 24

Armillotta L., Fraternali F., Werk J. K., Prochaska J. X., Marinacci F., 2017, MNRAS, 470, 114

Aung H., Mandelker N., Nagai D., Dekel A., Birnboim Y., 2019, MNRAS, 490, 181

Babcock H. W., 1939, Lick Obs. Bull., 498, 41

Baldry I. K., Glazebrook K., Brinkmann J., Ivezić Ž., Lupton R. H., Nichol R. C., Szalay A. S., 2004, ApJ, 600, 681

Baldry I. K., Glazebrook K., Driver S. P., 2008, MNRAS, 388, 945

Bale S. D., Pulupa M., Salem C., Chen C. H., Quataert E., 2013, Astrophys. J. Lett., 769, 2

Barkana R., Loeb A., 2001, PhyRev, 349, 125

Battaia F. A., Prochaska J. X., Hennawi J. F., Obreja A., Buck T., Cantalupo S., Dutton A. A., Macciò A. V., 2018, MNRAS, 473, 3907

Begelman M. C., 1990, MNRAS, 000, 26

Bell E. F., et al., 2004, ApJ, 608, 752

Bennett J. S., Sijacki D., 2020, MNRAS, 499, 597

Bennett C. L., et al., 1996, ApJ, 464, L1

Bennett C. L., et al., 2013, ApJS, 208, 20

Berlok T., Pfrommer C., 2019a, MNRAS, 485, 908

Berlok T., Pfrommer C., 2019b, MNRAS, 489, 3368

Bernet M. L., Miniati F., Lilly S. J., Kronberg P. P., Dessauges-Zavadsky M., 2008, Nature, 454, 302

Birkinshaw M., 1984, MNRAS, 208, 887

Birnboim Y., Dekel A., 2003, MNRAS, 345, 349

Black J. H., 1981, MNRAS, 197, 553

Blanton M. R., et al., 2003, ApJ, 594, 186

Blumenthal G. R., Faber S. M., Primack J. R., Rees M. J., 1984, Nature, 311, 517

Bodo G., Massaglia S., Ferrari A., Trussoni E., 1994, Astron. Astrophys., 283, 655

Borisova E., et al., 2016, ApJ, 831, 39

Bouché N., Murphy M. T., Kacprzak G. G., Contini T., Martin C. L., 2013, Science, 341, 50

Bouché N., et al., 2016, ApJ, 820, 121

Bouwens R. J., et al., 2012a, ApJL, 752, L5

Bouwens R. J., et al., 2012b, ApJ, 754, 83

Boylan-Kolchin M., Springel V., White S. D. M., Jenkins A., Lemson G., 2009, MNRAS, 398, 1150

Brüggen M., Scannapieco E., 2023, The Launching of Cold Clouds by Galaxy Outflows. V: The role of anisotropic thermal conduction, preprint (arXiv:2304.09881)

Cantalupo S., Arrigoni-Battaia F., Prochaska J. X., Hennawi J. F., Madau P., 2014, Nature, 506, 63

Cen R., 1992, ApJS, 78, 341

Chandrasekhar S., 1961, Hydrodynamic and hydromagnetic stability. Dover Publications

Chen Y., et al., 2020, MNRAS, 499, 1721

Christopher Martin D., et al., 2019, Nat. Astron., 3, 822

Couchman H. M. P., Rees M. J., 1986, MNRAS, 221, 53

Cowie L. L., Mckee C. F., 1977, ApJ, 211, 135

Cucciati O., et al., 2012, Astron. Astrophys., 539, A31

Daddi E., et al., 2021, A& A, 649, A78

Daddi E., et al., 2022, ApJL, 926, L21

Dahlen T., Mobasher B., Dickinson M., Ferguson H. C., Giavalisco M., Kretchmer C., Ravindranath S., 2007, ApJ, 654, 172

Davis M., Efstathiou G., Frenk C. S., White S. D. M., 1985, ApJ, 292, 371

Dayal P., Ferrara A., 2018, Phys. Rep., 780-782, 1

De Lucia G., Blaizot J., 2007, MNRAS, 375, 2

Dekel A., Birnboim Y., 2006, MNRAS, 368, 2

Dekel A., et al., 2009, Nature, 457, 451

Dekel A., Zolotov A., Tweed D., Cacciato M., Ceverino D., Primack J. R., 2013, MNRAS, 435, 999

Delubac T., et al., 2015, A&A, 574, A59

Dijkstra M., 2017, Saas-Fee Lecture Notes: Physics of Lyman Alpha Radiative Transfer, preprint (`arXiv:1704.03416`)

Dimotakis P. E., 1991, Technical report, Turbulent Free Shear Layer Mixing and Combustion, `https://www.dimotakis.caltech.edu/pub/91/dimotakis.91d.html`. AIAA, `https://www.dimotakis.caltech.edu/pub/91/dimotakis.91d.html`

Dolag K., Kachelriess M., Ostapchenko S., Tomàs R., 2011, ApJL, 727

Efstathiou G., 1992, MNRAS, 256, 43P

Einstein A., 1916, Annalen der Physik, 354, 769

Eisenstein D. J., et al., 2005, ApJ, 633, 560

Emonts B. H., et al., 2023, Science, 379, 1323

Endsley R., Stark D. P., Whitler L., Topping M. W., Chen Z., 2023, MNRAS, 2330, 2312

Fall M. S., Efstathiou G., 1980, MNRAS, 193, 189

Fardal M. A., Katz N., Gardner J. P., Hernquist L., Weinberg D. H., Dave R., 2001, ApJ, 562, 605

Faucher-Giguère C. A., Kereš D., 2011, MNRAS, 412, 118

Favre A., 1969, Philadelphia: Society for Industrial and Applied Mathematics, pp 231–266

Ferland G. J., et al., 2017, Rev. Mex. Astron. Astrof., 53, 385

Ferrari A., Trussoni E., Zaninetti L., 1978, Astron. Astrophys., 64, 43

Fielding D. B., Ostriker E. C., Bryan G. L., Jermyn A. S., 2020, ApJ, 894, L24

Finlator K., Keating L., Oppenheimer B. D., Davé R., Zackrisson E., 2018, MNRAS, 480, 2628

Fu H., Xue R., Prochaska J. X., Stockon A., Ponnada S., Lau M. W., Cooray A., Narayanan D., 2021, ApJ, 908, 188

Fumagalli M., Prochaska J. X., Kasen D., Dekel A., Ceverino D., Primack J. R., 2011, MNRAS, 418, 1796

Fumagalli M., Cantalupo S., Dekel A., Morris S. L., O'Meara J. M., Prochaska J. X., Theuns T., 2016, MNRAS, 462, 1978

Furlanetto S. R., Zaldarriaga M., Hernquist L., 2004, ApJ, 613, 1

Gardiner T. A., Stone J. M., 2005, J. Comput. Phys., 205, 509

Gardiner T. A., Stone J. M., 2008, J. Comput. Phys., 227, 4123

Geller M. J., Huchra J. P., 1989, Science (80-.)., 246, 897

Genel S., et al., 2014, MNRAS, 445, 175

Giavalisco M., et al., 2011, ApJ, 743, 95

Gnedin N. Y., 2000a, ApJ, 535, 530

Gnedin N. Y., 2000b, ApJ, 542, 535

Gnedin N. Y., 2014, ApJ, 793, 1

Goerdt T., Dekel A., Sternberg A., Ceverino D., Teyssier R., Primack J. R., 2010, MNRAS, 407, 613

Gott III J. R., Juric M., Schlegel D., Hoyle F., Vogeley M. S., Tegmark M., Bahcall N., Brinkmann J., 2005, ApJ, 624, 463

Gray D. R., Kilkenny J. D., 1980, Plasma Phys., 22, 81

Greif T. H., Johnson J. L., Klessen R. S., Bromm V., 2008, MNRAS, 387, 1021

Greif T. H., Glover S. C. O., Bromm V., Klessen R. S., 2010, ApJ, 716, 510

Gronke M., Oh S. P., 2018, MNRAS, 480, L111

Gronke M., Oh S. P., 2020, MNRAS, 492, 1970

Gruppioni C., et al., 2013, MNRAS, 432, 23

Guo Q., et al., 2011, MNRAS, 413, 101

Haardt F., Madau P., 1996, ApJ, 461, 20

Haardt F., Madau P., 2012, ApJ, 746

Hardee P. E., 1987, Astron. J., 313, 607

Hardee P. E., Norman M. L., 1988, ApJ, 334, 70

Hidalgo-Pineda F., Farber R. J., Gronke M., 2023, Better Together: The Complex Interplay Between Radiative Cooling and Magnetic Draping, preprint (`arXiv:2304.09897`)

Hillier A., Arregui I., 2019, ApJ, 885, 101

Hillier A., Van Doorsselaere T., Karampelas K., 2020, ApJ, 897, L13

Hinshaw G., et al., 2013, ApJS, 208, 19

Hopkins P. F., Chan T. K., Garrison-kimmel S., Ji S., Su K.-y., Hummels C. B., Quataert E., 2020, MNRAS, 492, 3465

Hubble E., 1929, Proc. Natl. Acad. Sci., 15, 168

Hummels C. B., et al., 2019, ApJ, 882, 156

Iliev I. T., Mellema G., Ahn K., Shapiro P. R., Mao Y., Pen U. L., 2014, MNRAS, 439, 725

Ji S., Oh S. P., Masterson P., 2019, MNRAS, 487, 737

Kannan R., Garaldi E., Smith A., Pakmor R., Springel V., Vogelsberger M., Hernquist L., 2022, MNRAS, 511, 4005

Katz N., Weinberg D. H., Hernquist L., 1996, ApJS, 105, 19

Kauffmann G., White S. D. M., Guiderdoni B., 1993, MNRAS, 264, 201

Kauffmann G., Colberg J. M., Diaferio A., White S. D. M., 1999, MNRAS, 303, 188

Kauffmann G., et al., 2003, MNRAS, 341, 33

Kereš D., Katz N., Weinberg D. H., Davé R., 2005, MNRAS, 363, 2

Komarov S., Schekochihin A. A., Churazov E., Spitkovsky A., 2018, J. of Plasma Phys., 84, 1

Komatsu E., et al., 2009, ApJS, pp 330–376

Kowalski M., et al., 2008, ApJ, 686, 749

Kwak K., Shelton R. L., 2010, ApJ, 719, 523

Lacey C., Cole S., 1993, MNRAS, 262, 627

Lan T. W., Prochaska J. X., 2020, MNRAS, 496, 3142

Larson D., et al., 2011, ApJS, 192, 16

Lemaître G., 1927, Annales de la Société Scientifique de Bruxelles, 47, 49

Lemaître G., 1931, Monthly Notices of the Royal Astronomical Society, 91, 483

Lewis J. S. W., et al., 2022, MNRAS, 3397, 3389

Madau P., Dickinson M., 2014, Annu. Rev. Astron. Astrophys., 52, 415

Magnelli B., Elbaz D., Chary R. R., Dickinson M., Le Borgne D., Frayer D. T., Willmer C. N. A., 2011, Astron. Astrophys., 528, A35

Magnelli B., et al., 2013, Astron. Astrophys., 553, A132

Mandelker N., Padnos D., Dekel A., Birnboim Y., Burkert A., Krumholz M. R., Steinberg E., 2016, MNRAS, 463, 3921

Mandelker N., Nagai D., Aung H., Dekel A., Padnos D., Birnboim Y., 2019, MNRAS, 484, 1100

Mandelker N., Nagai D., Aung H., Dekel A., Birnboim Y., Van Den Bosch F. C., 2020a, MNRAS, 494, 2641

Mandelker N., Van Den Bosch F. C., Nagai D., Dekel A., Birnboim Y., Aung H., 2020b, MNRAS, 498, 2415

Martin-Alvarez S., Devriendt J., Slyz A., Teyssier R., 2018, MNRAS, 479, 3343

Martin C. L., Shapley A. E., Coil A. L., Kornei K. A., Bundy K., Weiner B. J., Noeske K. G., Schiminovich D., 2012, ApJ, 760, 127

Matte J. P., Virmont J., 1982, Phys. Rev. Lett., 49, 1936

Meinecke J., et al., 2022, Sci. Adv., 8, 1

Meyer C. D., Balsara D. S., Aslam T. D., 2014, J. Comput. Phys., 257, 594

Miyoshi T., Kusano K., 2005, J. Comput. Phys., 208, 315

Mo H. J., Mao S., White S. D. M., 1998, MNRAS, 295, 319

Navarro J. F., Frenk C. S., White S. D. M., 1996, ApJ, 462, 563

Navarro J. F., Frenk C. S., White S. D. M., 1997, ApJ, 490, 493

Nelson D., et al., 2018, MNRAS, 475, 624

Nelson D., et al., 2020, MNRAS, 498, 2391

Neronov A., Vovk I., 2010, Science, 328, 73

Norman M. L., Hardee P. E., 1988, ApJ, 334, 80

Ocvirk P., Pichon C., Teyssier R., 2008, MNRAS, 390, 1326

Ocvirk P., et al., 2016, MNRAS, 463, 1462

Ostriker J. P., 1964, ApJ, p. 1056

Padnos D., Mandelker N., Birnboim Y., Dekel A., Krumholz M. R., Steinberg E., 2018, MNRAS, 477, 3293

Pakmor R., et al., 2017, MNRAS, 469, 3185

Pakmor R., Guillet T., Pfrommer C., Gómez F. A., Grand R. J., Marinacci F., Simpson C. M., Springel V., 2018, MNRAS, 481, 4410

Pakmor R., et al., 2020, MNRAS, 498, 3125

Pawlik A. H., Rahmati A., Schaye J., Jeon M., Vecchia C. D., 2017, MNRAS, 466, 960

Payne D. G., Cohn H., 1985, ApJ, 291, 655

Peeples M. S., et al., 2019, MNRAS, 873, 129

Peng Y.-j., et al., 2010, ApJ, 721, 193

Percival W. J., Cole S., Eisenstein D. J., Nichol R. C., Peacock J. A., Pope A. C., Szalay A. S., 2007, MNRAS, 381, 1053

Percival W. J., et al., 2010, MNRAS, 401, 2148

Perlmutter S., et al., 1999, ApJ, 517, 565

Planck Collaboration ., et al., 2014, Astron. Astrophys., 571, A16

Planck Collaboration et al., 2016, Astron. Astrophys., 594, A13

Planck Collaboration et al., 2020, Astron. Astrophys., 641, A6

Planck Collaboration et al., 2021, Astron. Astrophys., 652, C4

Press W. H., Schechter P., 1974, APJ, 187, 425

Prochaska X. J., et al., 2019, Science, 73, 1

Reddy N. A., Steidel C. C., 2009, ApJ, 692, 778

Reed D., Gardner J., Quinn T., Stadel J., Fardal M., Lake G., Governato F., 2003, MNRAS, 346, 565

Rees M. J., Ostriker J. P., 1977, MNRAS, 179, 541

Rieder M., Teyssier R., 2017, MNRAS, 471, 2674

Riess A. G., et al., 1998, AJ, 116, 1009

Riess A. G., et al., 2004, ApJ, 607, 665

Riess A. G., et al., 2007, ApJ, 659, 98

Robertson B. E., 2022, Annu. Rev. Astron. Astrophys., 60, 121

Robotham A. S. G., Driver S. P., 2011, MNRAS, 413, 2570

Roca-Fabrega S., et al., 2019, Mon, 484, 3625

Roca-Fàbrega S., et al., 2021, ApJ, 917, 64

Rosdahl J., et al., 2018, MNRAS, 479, 994

Rubin V. C., Ford W. K., 1970, ApJ, 159, 379

Rubin K. H. R., Prochaska J. X., Koo D. C., Phillips A. C., 2012, ApJL, 747, 26

Sander B., Hensler G., 2021, MNRAS, 501, 5330

Sander B., Hensler G., 2023, MNRAS, 519, 1313

Sanders D. B., Mazzarella J. M., Kim D. C., Surace J. A., Soifer B. T., 2003, AJ, 126, 1607

Saveliev A., Jedamzik K., Sigl G., 2012, Phys. Rev. D, 86, 1

Schenker M. A., et al., 2013, ApJ, 768, 196

Schiminovich D., et al., 2005, ApJL, 619, L47

Seo H.-J., Eisenstein D. J., 2003, ApJ, 598, 720

Shapiro P. R., Iliev I. T., Raga A. C., 2004, MNRAS, 348, 753

Sharma P., Hammett G. W., 2007, J. Comput. Phys., 227, 123

Shen X., et al., 2023, (preprint), 22, 1

Sheth R. K., Tormen G., 1999, MNRAS, 308, 119

Sheth R. K., Tormen G., 2002, MNRAS, 329, 61

Sheth R. K., Mo H. J., Tormen G., 2001, MNRAS, 323, 1

Silk J., 1977, ApJ, 211, 638

Slavin J. D., Shull M. J., Begelman M. C., 1993, ApJ, 407, 83

Smith B. D., et al., 2017, MNRAS, 466, 2217

Smith A., Kannan R., Garaldi E., Vogelsberger M., Pakmor R., Springel V., Hernquist L., 2022, MNRAS, 3265, 3243

Smoot G. F., et al., 1992, ApJ, 396, L1

Somerville R. S., Kolatt T. S., 1999, MNRAS, 305, 1

Spergel D. N., et al., 2003, ApJS, 148, 175

Spitzer L., 1962, Physics of Fully Ionized Gases. Interscience, New York

Springel V., et al., 2005, Nature, 435, 629

Springel V., Frenk C. S., White S. D., 2006, Nature, 440, 1137

Spruit H. C., 2013, Essential Magnetohydrodynamics for Astrophysics, preprint (arXiv:1301.5572)

Steinwandel U. P., Beck M. C., Arth A., Dolag K., Moster B. P., Nielaba P., 2019, MNRAS, 483, 1008

Stone J. M., Tomida K., White C. J., Felker K. G., 2020, ApJ, 249, 4

Strateva I., et al., 2001, AJ, 122, 1861

Strawn C., et al., 2021, MNRAS, 501, 4948

Suresh J., Nelson D., Genel S., Rubin K. H., Hernquist L., 2019, MNRAS, 483, 4040

Takeuchi T. T., Yoshikawa K., Ishii T. T., 2003, ApJL, 587, L89

Tan B., Oh S. P., Gronke M., 2021, MNRAS, 502, 3179

Tegmark M., Silk J., Rees M. J., Blanchard A., Abel T., Palla F., 1997, ApJ, 474, 1

Thoul A. A., Weinberg D. H., 1996, ApJ, 465, 608

Treu T., et al., 2023, Astrophys. J. Lett., 942, L28

Turner M. L., Schaye J., Crain R. A., Rudie G., Steidel C. C., Strom A., Theuns T., 2017, MNRAS, 471, 690

Umehata H., et al., 2019, Science (80-.)., 366, 97

Vogelsberger M., et al., 2014, MNRAS, 444, 1518

Vossberg A. C. E., Cantalupo S., Pezzulli G., 2019, MNRAS, 489, 2130

White S. D. M., Frenk C. S., 1991, ApJ, 379, 52

White S. D. M., Rees M. J., 1978, MNRAS, 183, 341

Wise J. H., Abel T., Turk M. J., Norman M. L., Smith B. D., 2012a, MNRAS, 427, 311

Wise J. H., Turk M. J., Norman M. L., Abel T., 2012b, ApJ, 745, 50

Wright E. L., et al., 1990, ApJ, 354, L37

Wyder T. K., et al., 2005, ApJL, 619, L15

Xu H., Wise J. H., Norman M. L., Ahn K., O'Shea B. W., 2016, ApJ, 833, 84

Yang Y., Ji S., 2023, MNRAS, 520, 2148

Yang X., Mo H. J., Van den Bosch F. C., 2003, MNRAS, 339, 1057

Yoshida N., Omukai K., Hernquist L., Abel T., 2006, ApJ, 652, 6

Yoshida N., Omukai K., Hernquist L., 2008, Science, 321, 669

Zabl J., et al., 2019, MNRAS, 485, 1961

Zhang S., et al., 2023, Science (80-.)., 380, 494

Zwicky F., 1937, ApJ, 86, 217

van de Voort F., Springel V., Mandelker N., van den Bosch F. C., Pakmor R., 2019, MNRAS, 482, L85